Measuring Beam Deflections Using Weak Value Amplification

Elina Köster

München, Mai 2023

Measuring Beam Deflections Using Weak Value Amplification

Elina Köster

München, Mai 2023

Measuring Beam Deflections Using Weak Value Amplification

Elina Köster

Masterarbeit
an der Fakultät für Physik
der Ludwig-Maximilians-Universität
München

vorgelegt von
Elina Köster
aus München

betreut von
Prof. Dr. H. Weinfurter

München, Mai 2023

Messung von Strahlauslenkungen mittels Weak-Value-Verstärkung

Elina Köster

Masterarbeit
an der Fakultät für Physik
der Ludwig-Maximilians-Universität
München

vorgelegt von
Elina Köster
aus München

betreut von
Prof. Dr. H. Weinfurter

München, Mai 2023

Abstract

The technique of weak value amplification makes it possible to measure small deflections of light precisely. So far, weak value amplification setups have measured deflections occurring in an interaction region inside the measurement device. Here, we present an interferometric weak measurement setup able to measure displacements and deflections of a light beam that occur *outside* of the measurement device. This is achieved by spatially separating the arms of a Sagnac-like interferometer and inserting a Dove prism into one of them.

The Dove prism mirrors the initial deflection, introducing a relative angle and offset between the two beams. The resulting interference depends on the initial deflection. Amplified by the weak value of the system, this allows a highly sensitive determination of the deflection and displacement.

We formulate a theoretical model of the experiment and compare its expected performance with respect to noise with alternative measurement methods. Furthermore, we describe an experimental realization we set up in a laboratory. We describe and discuss difficulties we encountered during the implementation and propose further improvements to the experimental setup.

We devise an algorithm to fit the model parameters to empirical data. When applied to our preliminary laboratory results, we see that the calculated deflections in the near and far field differ more than expected. We attribute this to the faulty performance of a quarter-wave plate which we observed. Based on our experience, we propose the next steps to proceed with the experimental realization.

Contents

1. Introduction

In classical mechanics, systems are usually measured indirectly by looking at the meter of a measurement device. The shift the meter displays correlates with a change of the system. For example, a voltage is measured by connecting a battery to a measurement device whose needle moves.

In quantum mechanics properties of systems are described by observables that can be measured. In the early days of quantum mechanics it already became clear that quantum systems can be measured similarly to classical systems. Von Neumann presented a measurement scheme [1] where a quantum mechanical system is coupled to a quantum mechanical measurement device. The change of the quantum system manifests as a change of the quantum mechanical pointer state.

In those measurements, like direct measurements of a quantum observable, the measurement results never exceed the minimal or maximal eigenvalue of the operator representing the observable. As a new development, Aharonov, Albert and Vaidman presented a measurement scheme [2] similar to the one of von Neumann, however, where the pointer shift can now go beyond the bound set by the minimal and maximal eigenvalue. This is achieved by carefully preparing the system to be measured in an initial state and selecting into a particular final state. The coupled preselected state of the system and the pointer are postselected with the final state of the system, which means that only certain information of the system is considered. Then, after the postselection, the pointer depends only on a quantity called the "weak value" of the system, which can be much larger than the largest eigenvalue.

By performing a postselection it is thus possible to amplify even small changes of a quantum system [2]. The finding is harnessed in a method called "weak value amplification". In 1991 the first realization of such a measurement was presented [3]. Since then, several experiments have made use of this technique, [4–9], where small misalignments were introduced into an interferometer. Weak value amplification allowed to measure the deflection in one arm of the interferometer precisely by evaluating the change of the pointer encoded in the spatial mode of the beam, i. e. the center of mass of the interfering beams.

In this work, an interferometric measurement is introduced, which allows to determine small beam deflections. In contrast to all previous experiments, the interaction region is not inside the interferometer but *outside*. This means that one can detect deflections outside of the interferometer, which was not possible before. In order to see a change of the interference pattern after the initial deflection, the

light beams in the different interferometer arms have to be displaced relative to each other. It is achieved by spatially separating the arms of a Sagnac-like interferometer and placing a Dove prism into one of the arms. The Dove prism mirrors the initial deflection along its axis, deflecting the two beams relative to each other. Hence, the initial deflection outside of the interferometer manifests in a change of the center of mass of the interference. Postselection amplifies the pointer shift, allowing a highly sensitive determination of the deflection parameters.

We formulate the theoretical model of this measurement technique and compare it with respect to noise with alternative measurement methods that do not employ the concept of weak value amplification. Furthermore, we describe an experimental realization we set up in the quantum optics laboratory at the Max-Planck-institute for Quantum Optics. We discuss difficulties that we encountered during the realization. We were able to overcome several obstacles, such as the faulty behavior of optical components. We propose solutions for the remaining issues.

We devise an algorithm to fit the model parameters to empirical data, which works for theoretical test data. When applied to our preliminary laboratory results, we see that the fitted deflections in the near and far field differ more than expected. We attribute this to the faulty performance of a quarter-wave plate, which we observed. Based on our experience, we propose the next steps for the experimental realization.

The thesis is structured as follows: In Chapter 2 fundamental aspects of optics, quantum mechanics, weak values and weak value amplification are described. In Chapter 3 our experiment is modeled theoretically and compared to two alternative measurement methods with regard to signal-to-noise ratio and technical noise. Chapter 4 describes the experimental setup, obstacles and solutions, the fitting algorithm and the preliminary data.

2. Weak values and related concepts

This chapter describes the theoretical fundamentals needed for the description and the understanding of the experiment that is presented in this thesis. First, some aspects of optics and key concepts of quantum mechanics, most importantly the standard quantum mechanical measurement process, are briefly called to mind. Next, the concept of pre- and postselected systems is discussed, in which the framework of weak values can be best understood. This concept offers a useful application, the so-called "weak value amplification", which is essential for the experiment.

2.1. Properties of light

Here, two concepts of optics that are exploited in this thesis are explained. This summary is based on [10–13].

2.1.1. Polarization of light

Light is an electromagnetic wave. The equation describing light can be derived from the Maxwell equations. For homogeneous media, without charge carriers or currents it describes a plane wave propagating in direction $\vec{k}$. It has the form

$$\vec{E}(\vec{r},t) = \vec{E}_0 \exp\Big[i(\omega t - \vec{k}\vec{r} + \varphi)\Big]\,. \tag{2.1}$$

$\vec{E}$ is the electric field vector, $\vec{E}_0$ is the amplitude of the field, ω is the angular frequency and φ is a phase angle. $\vec{k}$ is the wave vector, which is perpendicular to the wavefront. It has norm $k = |\vec{k}| = \frac{2\pi}{\lambda}$ with λ being the wavelength of the light. The intensity I of the electric field can be related to the field by

$$I(\vec{r},t) \propto |\vec{E}(\vec{r},t)|^2\,. \tag{2.2}$$

If the electric wave vector $\vec{E}$ oscillates in one plane the light is said to be polarized. There are three polarizations the light can have: linear, circular or

elliptical polarization. Assuming the wave propagates along the z-axis Eq. 2.1 can be simplified to

$$\vec{E}(z,t) = \begin{bmatrix} E_x e^{i(\omega t - kz)} \\ E_y e^{i(\omega t - kz + \varphi)} \\ 0 \end{bmatrix} . \tag{2.3}$$

We can see that this wave is a superposition of a wave oscillating in the x-z plane and one in the y-z plane that has a phase difference φ to the first wave. This phase difference influences the polarization of the light, as we will see now.

Linear polarization of light generally refers to light whose electric (and magnetic) field vector oscillates in one direction. The electric field vector of horizontally polarized light lies horizontally in a chosen reference frame, while the electric field vector of vertical light is perpendicular to this plane. Any other linear polarization state can be described as as superposition of horizontal and vertical light that are in phase, that is $\varphi = 0$.

In Fig. 2.1 linear light is depicted. The blue wave oscillates in the horizontal plane and the red wave on the vertical plane. They are in phase. The green wave is a superposition of the two waves, also having linear polarization, but oscillating in a plane tilted relative to the horizontal and vertical plane.

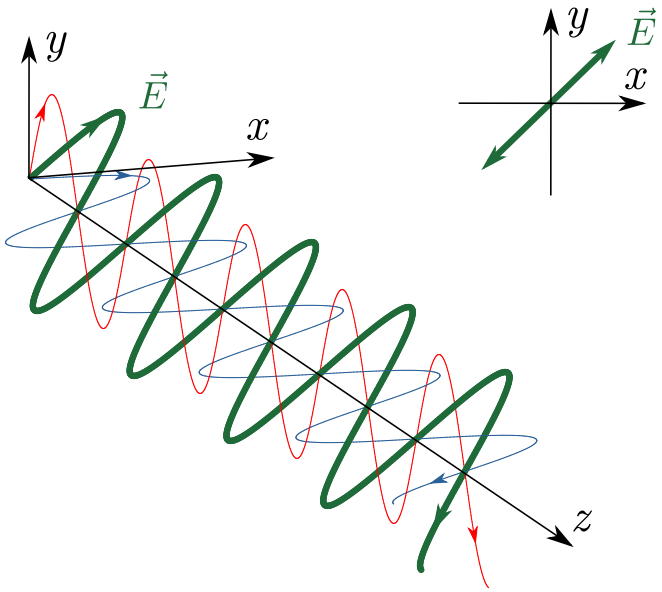

Figure 2.1.: Light with linear polarization. The blue and red wave are horizontal and vertical polarized light without phase difference. The green wave is the superposition of the horizontal and vertical light, which is also linear polarized light oscillating in a plane tilted with respect to the horizontal and vertical plane. The electric field vector $\vec{E}$ oscillates in one direction.

The electric field vector of **elliptical light** changes its direction, describing an ellipse in the plane perpendicular to the propagation direction of the light. Over

one period the vector changes its length. Depending on the circulation direction the light is called right-handed or left-handed. The light itself is a superposition of horizontal and vertical polarized light that are not in phase, that is $\varphi \neq 0$. This can be seen in Fig. 2.2. The horizontal and vertical wave are not in phase, which results in the superposition evolving in a spiral, the green wave. The projection of the spiral is an ellipse.

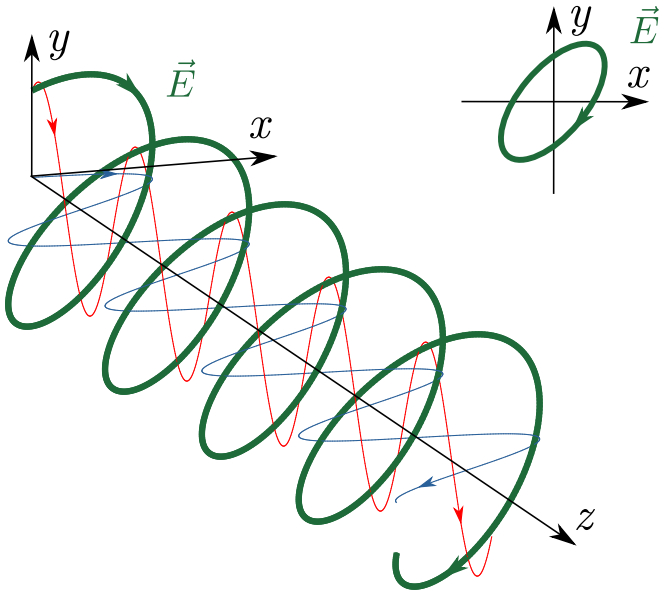

Figure 2.2.: Light with elliptical polarization. The blue and red wave are horizontal and vertical polarized light with a phase difference. The green wave is the superposition of the horizontal and vertical light, which is elliptical polarized light. The electric field vector $\vec{E}$ oscillates in a plane that is perpendicular to the propagation direction of the wave, describing an ellipse. During a period it changes its length.

For phase differences of exactly $\varphi = \frac{\pi}{2}$ the electric field vector describes a circle, hence one speaks of **circular polarized** light. During a period its length remains constant. This is shown in Fig. 2.3. The horizontal and vertical wave have a phase difference of $\frac{\pi}{2}$, which results in the superposition evolving in a spiral, the green wave. The projection of the spiral is a circle.

2.1.2. Gaussian beam

Light beams are often represented as straight lines or rays, whose intensity distribution has a finite radius. This is not the reality of light. In one possible solution to the paraxial approximation of the Helmholtz equation, light evolves as a so-called Gaussian beam. There, the intensity distribution follows a Gaussian

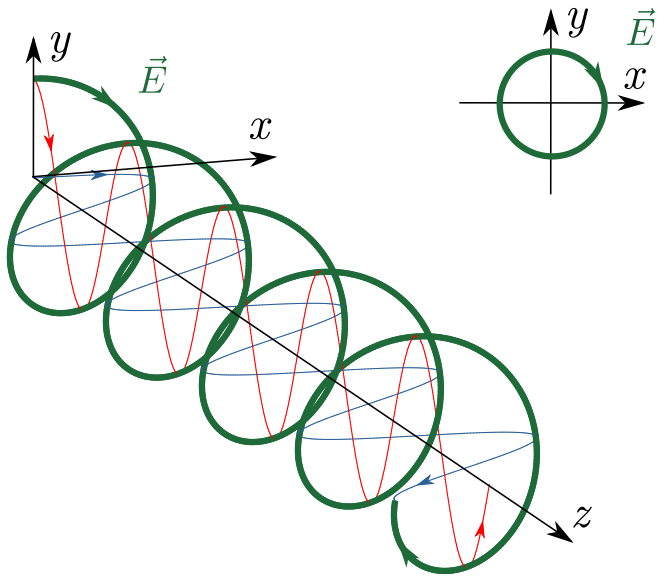

Figure 2.3.: Light with circular polarization. The blue and red wave are horizontal and vertical polarized light with a phase difference of $\frac{\pi}{2}$. The green wave is the superposition of the horizontal and vertical light, which is circular polarized light. The electric field vector oscillates in a plane that is perpendicular to the propagation direction of the wave, describing a circle. During a period its length remains constant.

distribution. The light propagates along an axis initially as a plane wave, which becomes curved with increased propagation distance.

Since laser light often has this form it is crucial to understand Gaussian beam for both the experiment and the theory of this thesis.

The electric field of a Gaussian beam propagating in z-direction is expressed as

$$E(r,z) = E_0 \frac{w_0}{w(z)} \exp\left(-\frac{r^2}{w(z)^2}\right) \exp\left(ikz + ik\frac{r^2}{2R(z)} - i\psi(z)\right), \tag{2.4}$$

where r is the radial distance from the propagation axis of the beam.

In this equation $E(r,z)$ is the electric field with the amplitude E_0. The intensity is given by

$$I(r,z) \propto |E(r,z)|^2 \propto \left(\frac{w_0}{w(z)}\right)^2 \exp\left(-\frac{2r^2}{w(z)^2}\right). \tag{2.5}$$

Such a beam is depicted in Fig. 2.4 in propagation direction z. Since the electric field, and therefore also the intensity, will never become zero, the width $w(z)$ of the beam is defined as the point where the electric field has decreased by $1/e$

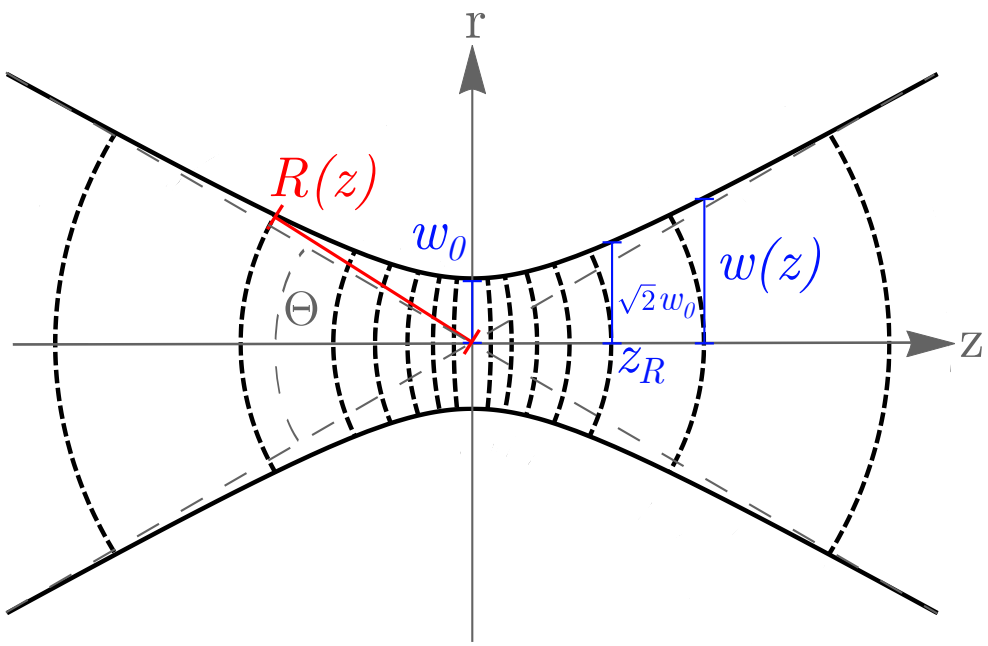

Figure 2.4.: A Gaussian beam propagating in z-direction. The thick solid line indicates the line where the field intensity has decreased $1/e^2$ with respect to the amplitude at the propagation axis. $w(z)$ is the beam radius at position z, $w_0 = w(z = 0)$ is the waist of the beam, z_R is the Rayleigh length, $R(z)$ the radius of curvature and Θ is twice the divergence angle of the beam.

with respect to the amplitude at the propagation axis, or where the intensity has decreased by $1/e^2$. The beam width is given by

$$w(z) = w_0 \sqrt{1 + \left(\frac{z}{z_R}\right)^2} . \tag{2.6}$$

Clearly, the Gaussian beam width is the smallest at $z = 0$. At this position $w(z)$ is denoted by w_0 and called the waist of the beam. z_R is the so-called Rayleigh length of the beam. At its position the beam width has increased by a factor $\sqrt{2}$, hence $w(z_R) = \sqrt{2} w_0$. The Rayleigh length is expressed as

$$z_R = \frac{\pi w_0^2}{\lambda} . \tag{2.7}$$

Here, λ is the wavelength of the beam. With very large z the beam width converges towards an asymptote. The angle between the propagation axis and the asymptote is called the divergence of the beam, defined as

$$\tan(\theta_{\text{div}}) \approx \theta_{\text{div}} = \frac{w_0}{z_R} = \frac{\lambda}{\pi w_0} . \tag{2.8}$$

Sometimes the divergence angle is defined as the angle between the two asymptotes of the upper and lower edge of the Gaussian beam, $\Theta = 2\theta_{\text{div}}$.

Eq. 2.4 is also dependent on the wave number k of the Gaussian beam and of $R(z)$. The parameter defines the radius of curvature the wavefront shows at position z. It is given by

$$\frac{1}{R(z)} = \frac{z}{z^2 + z_R^2}\,. \tag{2.9}$$

The radius of the wavefront is therefore given by

$$R(z) = z\left[1 + (\frac{z_R}{z})^2\right]. \tag{2.10}$$

At the waist of the beam $R(z = 0) = \infty$, hence there the wavefront is plane. At $z = z_R$ the wavefront curvature is the largest with $1/(2z_R)$. For $z \to \infty$ the wavefront resembles the wavefront of a spherical wave with origin $z = 0$ [14].

The last term in Eq. 2.4 is the Gouy-phase

$$\psi(z) = \arctan\left(\frac{z}{z_R}\right). \tag{2.11}$$

over the whole length of the Gaussian beam the Gouy phase changes from $-\pi/2$ to $\pi/2$, with the biggest change happening around the focal area of the beam, $z = 0$. [14]

2.2. Quantum mechanics in Hilbert spaces

Here, just a very short introduction to Quantum mechanics is given. For a much more extensive description please refer to [15, 16], on which this chapter is also based on.

States and operators A quantum state representing the physical state of a quantum system can be written as a vector in a Hilbert space

$$|v\rangle \in \mathcal{H}\,. \tag{2.12}$$

Here the Dirac notation (or bra-ket notation) is used. $|v\rangle$ is called ket. It can often be represented as a column vector. Any arbitrary state $|v\rangle$ can be decomposed into the eigenbasis of an operator $\hat{A}$,

$$|v\rangle = \sum_i c_i\,|a_i\rangle \quad \text{where} \quad c_i \in \mathbb{C}\,. \tag{2.13}$$

Here, $|a_i\rangle$ are the eigenvectors of the operator $\hat{A}$ with corresponding eigenvalues a_i. Quantum mechanical states are normalized, i.e. for the prefactors c_i, the so-called probability amplitudes, the following relation applies:

$$\sum_i |c_i|^2 = 1\,. \tag{2.14}$$

Observables For quantum states and operators one can find the hermitian transpose. In general the relation

$$(\hat{A}\,|v\rangle)^\dagger = \langle v|\,\hat{A}^\dagger \tag{2.15}$$

holds. $\langle v|$ is dual to $|v\rangle$ and is called a bra. It can often be represented as a row vector. If $\hat{A} = \hat{A}^\dagger$, the eigenvalues of the operator are real; it is then called a hermitian operator. In quantum physics those operators represent observables, that is measurable properties of physical systems like the position, the momentum or the spin of the system. The information about the possible measurement results is contained in the eigenvalues of the operator, hence it makes sense that they are real.

Position and momentum operator, wave function One of those operators is the position operator $\hat{x}$. A state $|v\rangle$ can be expanded in the basis of the position operator as

$$|v\rangle = \int dx\,|x\rangle\langle x|\,|v\rangle\ . \tag{2.16}$$

The inner product

$$\langle x|v\rangle := \psi_v(x) \tag{2.17}$$

is called the wave function of the state $|v\rangle$ in position space. The wave function for the momentum space can be found by Fourier transforming the wave function of the position space.

Density matrix, pure and mixed states Another representation for a quantum state is the density matrix $\hat{\rho}$. For a so-called pure state $|\psi\rangle$ it is just

$$\hat{\rho} = |\psi\rangle\langle\psi|\ . \tag{2.18}$$

This matrix $\hat{\rho}$ represents a quantum ensemble, where all physical systems can be described by the state $|\psi\rangle$. Because this state is known, the density matrix does not contain any new information about the ensemble. Now imagine an ensemble where a fraction p_1 is represented by a state $|\psi_1\rangle$, while another fraction p_2 is represented by $|\psi_2\rangle$. Such an ensemble is called mixed state. For a mixed state the state vector is unknown and one can only use the density matrix to describe the system. It has the form

$$\hat{\rho} = \sum_i p_i\,|\psi_i\rangle\langle\psi_i| \tag{2.19}$$

where $\sum_i p_i = 1$.

A density matrix is always positive semi-definite, hermitian and it satisfies $\mathrm{Tr}[\hat{\rho}] = 1$. For pure states $\mathrm{Tr}[\hat{\rho}^2] = 1$ while for mixed states $\mathrm{Tr}[\hat{\rho}^2] < 1$.

Product and entangled states Consider a quantum system A $|\psi\rangle_A$ in the Hilbert space $\mathcal{H}_A$ and a system B $|\psi\rangle_B$ in a Hilbert space $\mathcal{H}_B$. A composite system $|\psi\rangle_{AB}$ is a state in both Hilbert spaces. This is denoted with the tensor product:

$$|\Psi\rangle_{AB} \in \mathcal{H}_A \otimes \mathcal{H}_B \,. \tag{2.20}$$

Using the basis $\{|n\rangle_A\}_{n=1}^{d_A}$ of $\mathcal{H}_A$ and basis $\{|m\rangle_B\}_{m=1}^{d_B}$ any composite state can be written as

$$|\Psi\rangle = \sum_{n=1}^{d_A}\sum_{m=1}^{d_B} c_{n,m}\,|n\rangle_A \otimes |m\rangle_B \;. \tag{2.21}$$

It is in general not possible to represent the composite system as a state

$$|\Psi\rangle_{AB} = |\psi_A\rangle \otimes |\psi_B\rangle \;, \tag{2.22}$$

hence in general $c_{n,m} \neq c_n c_m$. If it is possible, $|\Psi\rangle$ is a product state. In this case $c_{n,m} = c_n c_m$. A state which can be represented as a sum of product states

$$\hat{\rho}_{AB} = \sum_i p_i \hat{\rho}_A^i \otimes \hat{\rho}_B^i \tag{2.23}$$

is a mixture of product states, called a separable state. Any other state

$$\hat{\rho}_{AB} \neq \sum_i p_i \hat{\rho}_A^i \otimes \hat{\rho}_B^i \tag{2.24}$$

is an entangled state. Operators can also be a composite of two operators acting on two Hilbert spaces,

$$\hat{O} = \hat{O}_A \otimes \hat{O}_B \quad \text{acting on} \quad \mathcal{H}_A \otimes \mathcal{H}_B \,. \tag{2.25}$$

Here, $\hat{O}_A$ acts on system A and $\hat{O}_B$ acts on system B. Note that the above definitions can also be extended to compositions of n systems. [17]

Qubits, Pauli matrices and Bloch sphere For a two dimensional system, a two-level system, one defines two basis states

$$\begin{bmatrix}0\\1\end{bmatrix} := |0\rangle \;, \quad \begin{bmatrix}1\\0\end{bmatrix} := |1\rangle \;. \tag{2.26}$$

The linear combination of those, often called qubit,

$$|\psi\rangle = \cos\left(\frac{\theta}{2}\right)|0\rangle + e^{i\varphi}\sin\left(\frac{\theta}{2}\right)|1\rangle \tag{2.27}$$

can describe any state in this two dimensional system. Here, θ is a parameter determining the probability amplitude of the state and φ is a phase. A basis for

operators acting on this state is $\{\mathbb{1}, \hat{\sigma}_x, \hat{\sigma}_y, \hat{\sigma}_z\}$, the identity $\mathbb{1}$ and the three Pauli matrices $\hat{\sigma}_x$, $\hat{\sigma}_y$, $\hat{\sigma}_z$. Their matrix form is

$$\mathbb{1} = \begin{bmatrix} 1 & 0 \\ 0 & 1 \end{bmatrix}, \quad \hat{\sigma}_x = \begin{bmatrix} 0 & 1 \\ 1 & 0 \end{bmatrix}, \quad \hat{\sigma}_y = \begin{bmatrix} 0 & -i \\ i & 0 \end{bmatrix} \quad \text{and} \quad \hat{\sigma}_z = \begin{bmatrix} 1 & 0 \\ 0 & -1 \end{bmatrix}. \tag{2.28}$$

The eigenvalues of the Pauli matrices are either +1 or –1. For different angles θ and phases φ the qubit $|\psi\rangle$ can become the eigenvector for one of those matrices. The eigenvectors (also called eigenstates) for the $\hat{\sigma}_z$ matrix are just the states $|0\rangle$ and $|1\rangle$, corresponding to the eigenvalues +1 and –1.

For the other matrices we find:

$$\mathrm{EV}_{\sigma_x+} := |+\rangle = \frac{1}{\sqrt{2}} \begin{bmatrix} 1 \\ 1 \end{bmatrix} = \frac{1}{\sqrt{2}}(|0\rangle + |1\rangle) \tag{2.29}$$

$$\mathrm{EV}_{\sigma_x-} := |-\rangle = \frac{1}{\sqrt{2}} \begin{bmatrix} 1 \\ -1 \end{bmatrix} = \frac{1}{\sqrt{2}}(|0\rangle - |1\rangle) \tag{2.30}$$

$$\mathrm{EV}_{\sigma_y+} := |+_y\rangle = \frac{1}{\sqrt{2}} \begin{bmatrix} 1 \\ i \end{bmatrix} = \frac{1}{\sqrt{2}}(|0\rangle + i\,|1\rangle) \tag{2.31}$$

$$\mathrm{EV}_{\sigma_y-} := |-_y\rangle = \frac{1}{\sqrt{2}} \begin{bmatrix} 1 \\ -i \end{bmatrix} = \frac{1}{\sqrt{2}}(|0\rangle - i\,|1\rangle) \tag{2.32}$$

A possible realization of such a two-level system is polarized light, which was explained in Section 2.1. There, one defines linear light with horizontal polarization as the first eigenstate of the Pauli-z-matrix, $|0\rangle := |H\rangle$ and the second eigenstate as linear light with vertical polarization, $|1\rangle := |V\rangle$.

The eigenstates of the Pauli-x-matrix are often called $|P\rangle$ ("Plus") and $|M\rangle$ ("Minus") in quantum optics. Decomposed into the basis vectors $|H\rangle$ and $|V\rangle$ they are written as

$$|P\rangle = \frac{1}{\sqrt{2}}(|H\rangle + |V\rangle) \quad \text{and} \quad |M\rangle = \frac{1}{\sqrt{2}}(|H\rangle - |V\rangle). \tag{2.33}$$

This state describes linear polarized light which has an angle $+45°$ or $-45°$ to horizontally polarized light.

Circular polarized light corresponds to the eigenvectors of the Pauli-y-matrix. It is referred to as $|R\rangle$ for right-handed polarization and $|L\rangle$ for left-handed polarization. It can be written as

$$|R\rangle = \frac{1}{\sqrt{2}}(|H\rangle + i\,|V\rangle) \quad \text{and} \quad |L\rangle = \frac{1}{\sqrt{2}}(|H\rangle - i\,|V\rangle). \tag{2.34}$$

To understand better how those states look and how they behave one often uses the Bloch sphere, see Fig. 2.5. In this sphere any qubit is represented as a vector from the origin to the surface of the sphere. Any linear polarized light is

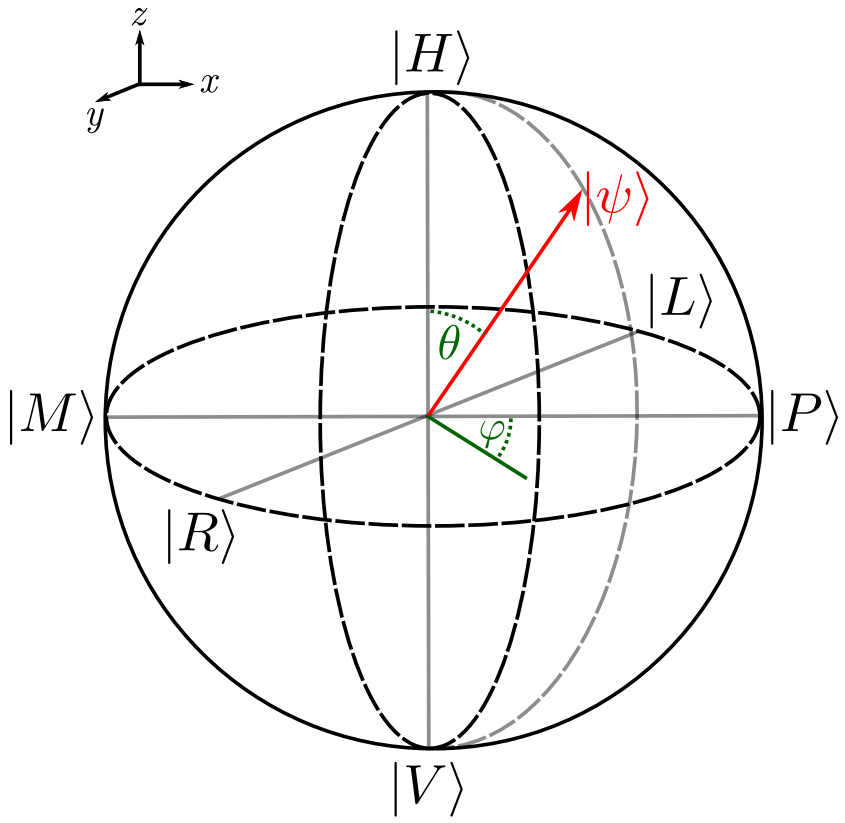

Figure 2.5.: A Bloch sphere. The red vector represents an arbitrary state $|\psi\rangle = \cos\left(\frac{\theta}{2}\right)|H\rangle + e^{i\varphi}\sin\left(\frac{\theta}{2}\right)|V\rangle$, where $|H\rangle$ denotes horizontal polarization of light and $|V\rangle$ vertical polarization. θ is a parameter determining the probability amplitude of the state and φ is a phase. The states $|P\rangle$ and $|M\rangle$ represent light with plus and minus polarization. $|R\rangle$ and $|L\rangle$ represent circular light. Any other vector on the surface of the sphere represents elliptical light.

represented as a vector in the z-x plane of the coordinate system, while circular light are the two vector along the y-axis of the sphere. Elliptical light is represented by any other vector on the surface of the sphere.

For pure states the point that defines the end of the state vector always lies on the surface of the sphere, whereas for mixed states this point lies inside the sphere.

2.3. Von Neumann quantum mechanical measurements

Just like classical systems, quantum systems can also be measured. A model for such measurements was first introduced by John von Neumann [1]. However,

the quantum mechanical measurement process has been subject to debates and discussions since the first days of quantum mechanics [18, 19]. [16] and [20] provide a good overview about quantum mechanical measurements and have been used to for the following summary.

2.3.1. Projective measurements

Assume that we want to measure an observable $\hat{A}$ of a state $|\psi\rangle$. The outcomes of the measurement are the eigenvalues of the observable a_i, and the state after the measurement is the corresponding eigenvector $|a_i\rangle$. It is clear that the minimal measurement result is the minimal eigenvalue of $\hat{A}$, and the maximal measurement result is the maximal eigenvalue.

In general a quantum mechanical operator $\hat{A}$ can be represented as

$$\hat{A} = \sum_i a_i \hat{P}_i \tag{2.35}$$

with $\hat{P}_i$ being the projection operator on the subspace of eigenstates with eigenvalue a_i [20]. The probability to find measurement result a_i when performing a measurement is given by

$$p_i = \mathrm{Tr}\left[\hat{P}_i \hat{\rho}\right], \tag{2.36}$$

which leaves the system in the state

$$\hat{\rho}_i = \frac{\hat{P}_i\, \hat{\rho}\, \hat{P}_i}{\mathrm{Tr}\left[\hat{P}_i\, \hat{\rho}\right]} \tag{2.37}$$

after the measurement.

The expectation value of operator $\hat{A}$ is given by

$$\langle \hat{A} \rangle = \mathrm{Tr}\left[\hat{\rho}\hat{A}\right] \tag{2.38}$$

which is bounded by the minimal and maximal eigenvalue of $\hat{A}$.

It is important to note that the measurement does not leave the system in the initial state but fundamentally alters the system. This reduction of the state to one eigenstate of the system is under discussion since the very early times of quantum mechanics. For standard quantum mechanics the change is purely probabilistic and called the "collapse of the wave function", as introduced by von Neumann [1]. There exist several alternative theories. For example, the pilot wave theory by de-Broglie and Bohm [21] describes actual particles governed by a pilot wave. The position of the particle is a "hidden variable" that determines the movement of the particles on trajectories [22, 23]. This way, the theory and also the results of a measurement is deterministic.

Another interpretation is the many-worlds interpretation of quantum mechanics [24]. In this description a measurement branches the words: In one world one measurement result is recorded, in another world the measurement has a different outcome [19].

2.3.2. Indirect measurement

In classical experiments the system is often not measured directly but instead a measurement device is used. The shift the meter displays correlates with a change of the system. For example, a voltage is measured by connecting a battery to a measurement device, whose needle moves. In quantum measurements one can do the same: A quantum system is coupled to a measurement device which is read out. This measurement scheme was originally presented by John von Neumann [1].

In this scheme, it is assumed that at a time $t = 0$ the system and the measurement device (which is called pointer) are in two uncorrelated pure states $|\psi\rangle \in \mathcal{H}_{\text{system}}$ and $|\Phi_0\rangle \in \mathcal{H}_{\text{pointer}}$ living in different Hilbert spaces. After some time the system and the pointer become correlated via a unitary transformation

$$\hat{U} = \exp\left[-i \underbrace{\int_{t_1}^{t_2} dt\, g(t)}_{:=\varepsilon} \hat{A} \otimes \hat{B}\right] \quad \text{acting on} \quad \mathcal{H}_{\text{system}} \otimes \mathcal{H}_{\text{pointer}}\,. \tag{2.39}$$

In this equation $g(t)\hat{A} \otimes \hat{B} = \hat{H}$ is the Hamiltonian of the interaction. $\hat{A}$ acts on the states in $\mathcal{H}_{\text{system}}$ and $\hat{B}$ acts on the states in $\mathcal{H}_{\text{pointer}}$. The factor ε specifies the interaction strength, i.e. how much the system is coupled to the pointer, with $g(t) \in \mathbb{R}$ being the coupling rate [20]. For convenience reasons we set here, and in the rest of the thesis that $\hbar = 1$. The coupling leads to the final state

$$|\Psi_f\rangle = \hat{U}\Big[\,|\psi\rangle \otimes |\Phi_0\rangle\,\Big] \in \mathcal{H}_{\text{system}} \otimes \mathcal{H}_{\text{pointer}}\,. \tag{2.40}$$

Afterwards the pointer observable is measured and provides the information of the system.

$|\Psi_f\rangle$ will get a simpler form if observable $\hat{B}$ and its conjugate $\hat{C}$ is considered. Then, using the spectral form of $\hat{A}$ and the composition of $|\psi\rangle$ into eigenstates of $\hat{A}$ one finds

$$\begin{aligned} |\Psi_f\rangle &= \exp\Big[-i\varepsilon \hat{A} \otimes \hat{B}\Big] \sum_i c_i\, |a_i\rangle \otimes |\Phi_0\rangle \\ &= \sum_i c_i\, |a_i\rangle \otimes \exp\Big[-i\varepsilon a_i \hat{B}\Big]\, |\Phi_0\rangle\ . \end{aligned} \tag{2.41}$$

This result reveals that the interaction changes the system and performs a shift $e^{-i\varepsilon a_i \hat{B}}$ on the pointer state. It also shows that the pointer state is a superposition of different pointer states all corresponding to a different measurement outcome a_i.

Now we can measure observable $\hat{C}$. To facilitate the calculation the identity is expanded in the eigenbasis of the the operators $\hat{B}$, $\hat{C}$,

$$\mathbb{1} = \int_b \mathrm{d}b \, |b\rangle\langle b| \ , \quad \mathbb{1} = \int_{c'} \mathrm{d}c' \, |c'\rangle\langle c'| \tag{2.42}$$

assuming a continuous eigenspace, therefore using integrals rather than sums. Moreover, we use that for conjugate operators $\langle b|c\rangle = \frac{1}{\sqrt{2\pi}} e^{ibc}$:

$$\begin{aligned}
|\Psi_f(c)\rangle &= \langle c|\Psi_f\rangle = \langle c|\Big[\exp\Big[-i\varepsilon \hat{A}\otimes\hat{B}\Big]\sum_i c_i\,|a_i\rangle\otimes|\Phi_0\rangle\Big] \\
&= \sum_i c_i\,|a_i\rangle \exp[-i\varepsilon a_i b]\int_{c'}\mathrm{d}c'\int_b \mathrm{d}b\,\langle c|b\rangle\,\langle b|c'\rangle\,\langle c'|\Phi_0\rangle \\
&= \sum_i c_i\,|a_i\rangle \int_{c'}\mathrm{d}c'\int_b \mathrm{d}b\,\frac{1}{2\pi}\exp[-i(c'-(c-\varepsilon a_i))b]\,\langle c'|\Phi_0\rangle \\
&= \sum_i c_i\,|a_i\rangle \int_{c'}\mathrm{d}c'\,\delta\Big(c'-(c-\varepsilon a_i)\Big)\Phi_0(c') \\
&= \sum_i c_i\,|a_i\rangle\,\Phi_0(c-\varepsilon a_i)\,.
\end{aligned} \tag{2.43}$$

Crucially, we see that in the final state the pointer wave function has shifted by εa_i. This shift represents the change, the system wave function has experienced. Each possible pointer wave function is centered around the eigenvalue of the operator $\hat{A}$ that a direct measurement on $\hat{A}$ would yield. We can also see that the the pointer can not be shifted further than $\varepsilon a_{\min}$ or $\varepsilon a_{\max}$, where $a_{\min}, a_{\max}$ are the minimal and maximal eigenvalue of operator $\hat{A}$. This agrees with the theory of protective measurements.

Any quantum operator $\hat{C}$ carries an uncertainty $\Delta\hat{C} = \sqrt{\left\langle \hat{C}^2\right\rangle - \left\langle \hat{C}\right\rangle^2}$. If the distance between the different eigenvalues a_i is smaller than the uncertainty $\Delta\hat{C}$, the wave packets $\Phi_0(c-\varepsilon a_i)$ and hence the measurement results a_i cannot be distinguished any more. To be able to perform meaningful measurements we therefore need to make sure that the wave packets do not overlap, which is the case when

$$|\varepsilon|\delta a \gg \Delta\hat{C} \tag{2.44}$$

with δa being the minimal distance between two eigenvalues a_i. If this condition is fulfilled, that is if the coupling strength ε is large, such a measurement is called a "strong measurement". A projective measurement on $\hat{C}$ will yield the the outcome

a_i with a probability of $|c_i|^2$ [23]. The pointer will be one single state centered around εa_i [23]. This illustrates the change of the system after the measurement, that is the collapse in the framework of standard quantum mechanics, or the branching of the worlds when following the many-worlds theory.

When ε is small, which is the case when

$$|\varepsilon|\delta a < \Delta\hat{C} \tag{2.45}$$

the measurement is called "weak measurement". Since the uncertainty of $\hat{C}$ is larger than the shift of the pointer one single measurement will give almost no information, however disturbing the system very little [25]. One has to perform measurements on a larger ensemble instead, and calculate the average of the results [20].

2.4. Pre- and postselected systems

This section describes an alternative, time-symmetric description of quantum mechanics, first introduced by Aharonov, Bergman and Lebowitz [26]. In this description not only the inital state of a system is know, but also the final state of the system. This has several important consequences for the outcomes of measurements.

2.4.1. The two-state vector formalism

In standard quantum mechanics, just the initial state of some system is known which then evolves in time according to the Schrödinger equation. The final state of the system is not known before the end of the evolution. Measurements in standard quantum mechanics are not deterministic, resulting in a final state which cannot be calculated before the measurement is performed [15]. The theory is therefore time asymmetric.

Aharonov, Bergman and Lebowitz introduced a new description of quantum mechanics, which is time symmetric [26]. In their description a system is described by both the inital state of a system and the final state, the two-state vector

$$\langle\phi|\ |\psi\rangle\ . \tag{2.46}$$

$|\psi\rangle$ is the initial state of the system and evolves forward in time, just as in the standard formalism of quantum mechanics. $\langle\phi|$ however is the final state and consequently evolves *backward* in time. In the example of an interferometer $|\psi\rangle$ evolves from the laser to the detector, while $\langle\phi|$ evolves from the detector towards the laser. The description is therefore called "two-state vector formalism" (TSVF).

In this formalism, the system is "preselected" to be in an initial state $|\psi\rangle$ and is "postselected" to a final state $\langle\phi|$. This corresponds to a projection onto the postselected state $|\phi\rangle$, such that other states the initial state could have evolve to are

not considered to be part of this pre- and postselected system. In a measurement process, the information encoded in them is hence thrown away.

Measurements of pre- and postselected systems can be strong or weak [20]. In this thesis, we shall only be concerned with weak pre- and postselected measurements, henceforth referred to as "weak measurements".

2.4.2. Weak values as outcomes of weak measurements

An extension of the TSVF is the so called "weak value" formalism, first introduced by Yakir Aharonov, David Z. Albert and Lev Vaidman in 1988 [2]. They showed that for weak measurements on a pre- and postselected system the measured results can be far beyond the range of measurement results that a standard measurement would yield.

The weak value formalism is at first analogue to the indirect standard measurements with the system being coupled to a measurement device, the pointer, see Section 2.3. On the system of the entangled state, however, a postselection is performed, after which only the final pointer state is considered. The whole measurement scheme is depicted in Fig. 2.6.

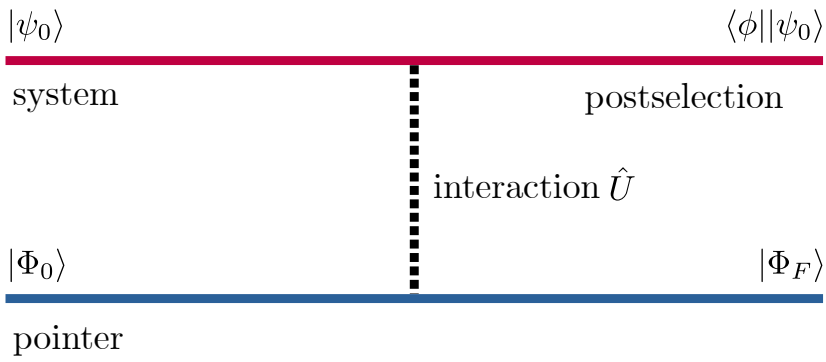

Figure 2.6.: Scheme of interaction of a pre- and postselected weak measurement. A quantum mechanical system is prepared in an inital state $|\psi_0\rangle$, the preselection. A pointer is prepared in an initial state $|\Phi_0\rangle$. A unitary interaction $\hat{U}$ couples the system with the pointer. A postselection with state $|\phi\rangle$ is then performed on the entangled state, after which only the final pointer state $|\Phi_F\rangle$ is considered.

In the description both the system to be measured and the pointer state are prepared in an initial state $|\psi_0\rangle \in \mathcal{H}_{\text{system}}$ respectively $|\Phi_0\rangle \in \mathcal{H}_{\text{pointer}}$. A unitary operation

$$\hat{U} = \exp\left[-i\varepsilon \hat{A} \otimes \hat{B}\right] \quad \text{acting on} \quad \mathcal{H}_{\text{system}} \otimes \mathcal{H}_{\text{pointer}} \tag{2.47}$$

couples the system to the measurement device, as in Section 2.3. Again, $\hat{A}$ is a self-adjoint observable of the system, while $\hat{B}$ is an operator acting on the pointer

system. $\varepsilon \in \mathbb{R}$ indicates the strength of the coupling. After the coupling we are left with an entangled state

$$|\Psi_f\rangle = \hat{U}\Big[\,|\psi_0\rangle \otimes |\Phi_0\rangle\,\Big] \tag{2.48}$$

which is the final state Eq. 2.41 of the indirect von Neumann measurement.

In the TSVF framework the entangled state is now projected on a the postselected state of the system $|\phi\rangle \in \mathcal{H}_{\text{system}}$. After this projection only the final state of the pointer is regarded. The final state of the pointer can be written as [27]:

$$\begin{aligned}
|\Phi_F\rangle &= \mathcal{N}\,\langle\phi|\Big[\,\hat{U}\,|\psi_0\rangle \otimes |\Phi_0\rangle\,\Big] \\
&= \mathcal{N}\,\langle\phi|\Big[\,\exp\Big(-i\varepsilon\hat{A}\otimes\hat{B}\Big)\,|\psi_0\rangle \otimes |\Phi_0\rangle\,\Big] \\
&\overset{\varepsilon\ll 1}{\approx} \mathcal{N}\,\langle\phi|\Big[\Big(\mathbb{1} - i\varepsilon\hat{A}\otimes\hat{B}\Big)|\psi_0\rangle \otimes |\Phi_0\rangle\,\Big] \\
&= \mathcal{N}\,\langle\phi|\psi_0\rangle\Big(\mathbb{1} - i\varepsilon\frac{\langle\phi|\,\hat{A}\,|\psi_0\rangle}{\langle\phi|\psi_0\rangle}\hat{B}\Big)|\Phi_0\rangle \\
&\approx \exp\left(-i\varepsilon\frac{\langle\phi|\,\hat{A}\,|\psi_0\rangle}{\langle\phi|\psi_0\rangle}\hat{B}\right)|\Phi_0\rangle\ ,
\end{aligned} \tag{2.49}$$

$\mathcal{N}$ is a suitable normalization factor. The approximation holds only for weak coupling regimes, where $\varepsilon \ll 1$, hence for weak measurements.

This formula contains the so called "weak value"

$$A_w := \frac{\langle\phi|\,\hat{A}\,|\psi_0\rangle}{\langle\phi|\psi_0\rangle} \tag{2.50}$$

of the pre- and postselected system. If $|\phi\rangle = |\psi_0\rangle$ the weak value becomes the expectation value of operator $\hat{A}$, $A_w = \langle\hat{A}\rangle$, which is bounded by the minimal and maximal eigenvalue of $\hat{A}$. However, when $|\phi\rangle$ is almost orthogonal to $|\psi_0\rangle$, the denominator of the weak value becomes almost zero, hence A_w becomes very large. This is a crucial point of the weak value formalism, because then measurement results can become very large, as we see now.

To see how much the pointer has shifted after the interaction we can perform a measurement on the pointer variable $\hat{O}$ acting on $\mathcal{H}_{\text{pointer}}$. For this, we just calculate the expectation value of the observable with the final state of the pointer:

$$\begin{aligned}
\langle \hat{O} \rangle &= \langle \Phi_F | \, \hat{O} \, | \Phi_F \rangle \\
&= \langle \Phi_0 | \, e^{i\varepsilon A_w^* \hat{B}} \, \hat{O} \, e^{-i\varepsilon A_w \hat{B}} \, | \Phi_0 \rangle \\
&\overset{\varepsilon \ll 1}{\approx} \langle \Phi_0 | \, (\mathbb{1} + i\varepsilon A_w^* \hat{B}) \, \hat{O} \, (\mathbb{1} - i\varepsilon A_w \hat{B}) \, | \Phi_0 \rangle \\
&= \langle \Phi_0 | \hat{O} | \Phi_0 \rangle + i\varepsilon A_w^* \, \langle \Phi_0 | \hat{B}\hat{O} | \Phi_0 \rangle - i\varepsilon A_w \, \langle \Phi_0 | \hat{O}\hat{B} | \Phi_0 \rangle + \mathcal{O}(\varepsilon^2) \\
&= \langle \Phi_0 | \hat{O} | \Phi_0 \rangle + \frac{1}{2} i\varepsilon A_w^* \big[\langle \Phi_0 | \, [\hat{B}, \hat{O}] \, | \Phi_0 \rangle + \langle \Phi_0 | \, \{\hat{B}, \hat{O}\} \, | \Phi_0 \rangle \big] \\
&\quad + \frac{1}{2} i\varepsilon A_w \big[\langle \Phi_0 | \, [\hat{B}, \hat{O}] \, | \Phi_0 \rangle - \langle \Phi_0 | \, \{\hat{B}, \hat{O}\} \, | \Phi_0 \rangle \big] \\
&= \langle \Phi_0 | \hat{O} | \Phi_0 \rangle \\
&\quad + i\varepsilon \, \mathrm{Re}[A_w] \, \langle \Phi_0 | \, [\hat{B}, \hat{O}] \, | \Phi_0 \rangle + \varepsilon \, \mathrm{Im}[A_w] \, \langle \Phi_0 | \, \{\hat{B}, \hat{O}\} \, | \Phi_0 \rangle \; . \qquad (2.51)
\end{aligned}$$

Note here that we assume that $\hat{B}^\dagger = \hat{B}$, that is $\hat{B}$ is hermitian. The shift the pointer experiences due to the interaction can then be expressed as the difference between the initial pointer position and its final position:

$$\begin{aligned}
\delta O &= \langle \Phi_F | \, \hat{O} \, | \Phi_F \rangle - \langle \Phi_0 | \, \hat{O} \, | \Phi_0 \rangle \\
&= i\varepsilon \, \mathrm{Re}[A_w] \, \langle \Phi_0 | \, [\hat{B}, \hat{O}] \, | \Phi_0 \rangle + \varepsilon \, \mathrm{Im}[A_w] \, \langle \Phi_0 | \, \{\hat{B}, \hat{O}\} \, | \Phi_0 \rangle \; . \qquad (2.52)
\end{aligned}$$

Unlike in a standard measurement, Eq. 2.52 is not dependent on an eigenvalue of operator $\hat{A}$ but only on its weak value A_w. This means that the measurement result is not necessarily bounded by the minimal and maximal eigenvalue, but could lie beyond - when the denominator in Eq. 2.50 becomes large, i.e. when the states are are almost orthogonal. This can be assured by pre- and postselecting the system in an appropriate manner.

The uncertainty of each measurement device is much larger than the measured value A_w [2]. However, performing measurements on a large ensemble decreases the uncertainty, allowing to determine the value of A_w accurately [28].

We see that we can strongly shift the pointer of the measurement device δO by postselecting on a final state that is almost orthogonal to the initial state of the system. We can amplify the pointer shift this way, in contrast to the standard measurement scheme where the pointer shift is bounded by the minimal and maximal eigenvalue of operator $\hat{A}$. This way even very small interactions ε can be detected.

2.4.3. Weak value amplification

Eq. 2.52 shows that the pointer shift of the measurement device can be amplified by pre- and postselecting the system in a smart way. This characteristics is harnessed by a method called "weak value amplification" (WVA) [29]:

In weak value amplification experiments pre- and postselection weak measurements are performed in such a way that the pointer shift of the measurement device is big. An experiment employing this fact was proposed in the original weak value article [2], by presenting a measurement on a spin-$\frac{1}{2}$-particle which would yield 100 as a result. The first experimental realization was [3], which demonstrated an amplification of a small beam separation.

To understand this phenomenon better, it is worth to consider classical waves or probability distributions. In Fig. 2.7 two intensities with Gaussian distribution in position space, $\Psi_1(x-d)$ and $\Psi_2(x+d)$ are shown. Their center of mass, i.e. their expectation values are indicated by dashed lines. They have been slightly shifted by $\pm d$ from position $x = 0$. When the Gaussians have a phase difference of π they interfere destructively, resulting in a Gaussian of low intensity, as depicted by the solid red line in Fig. 2.7. When the intensity is rescaled, it becomes visible that its center of mass lies far beyond the centers of mass of the individual Gaussians. Hence, the deflection that the two Gaussians experienced is amplified. This scenario can occur, for example in a interferometer, where both arms are slightly misaligned.

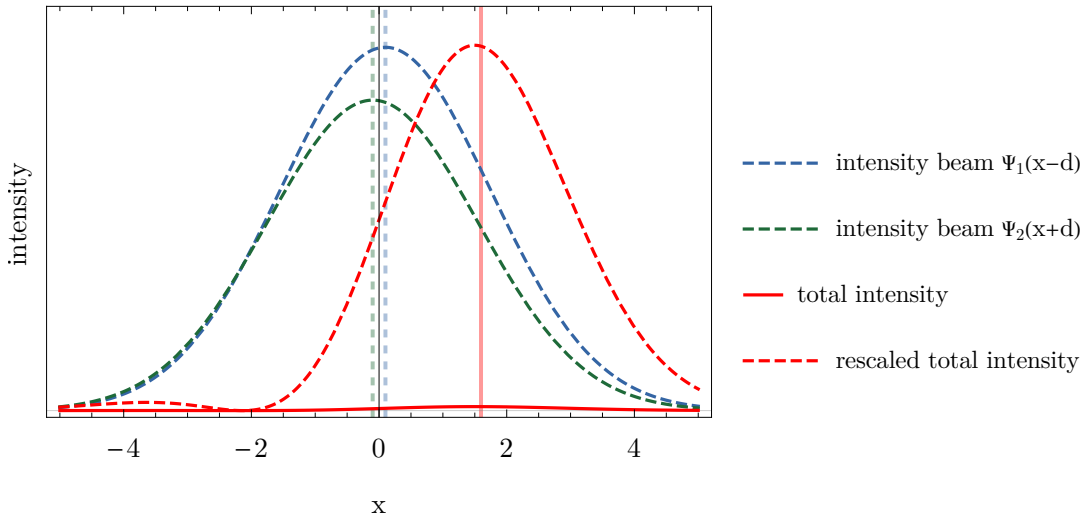

Figure 2.7.: Weak value amplification demonstrated with two Gaussian wave packages. The blue and green wave packages have been slightly shifted by $\pm d$ from position $x = 0$. The solid red line is their destructive interference. When rescaled it becomes visible that the expectation value for the combined intensity lies far beyond the expectation values of the two individual wave packages.

This classical description is similar to the quantum mechanical weak value amplification of Eq. 2.52. Assume that the blue and green curve is the pointer of the standard measurement scheme of Eq. 2.43, which is a sum of Gaussians slightly shifted by some small interaction. Since the shift is much smaller than the width

of the pointer, it can hardly be detected. In a weak measurement the destructive interference is introduced by postselecting the system on a state almost orthogonal to the preselected state. This results, due to the entanglement of the system and pointer states, in a shift of the pointer according to the weak measurement scheme in Eq. 2.52.

Weak value amplification allows to enhance small interactions and measure them precisely. However, one has a price to pay, namely, throwing away much of the ensemble in the postselection process. This has led to a controversial debate about the merits of weak value amplification. In Section 3.3 the ongoing debate about the merits of weak value amplification is presented.

In this thesis a weak value amplification experiment is discussed in detail. The goal is to precisely measure beam deflections using weak value amplification. In Section 3.3 the experiment is compared to other measurement methods, e.g. using a lens to detect the deflection.

3. Interferometric measurement device for small beam deflections

Interferometers are optical devices that make beams or particles interfere. This chapter describes a widely used interferometer, the Mach-Zehnder interferometer, quantum mechanically and summarizes a gedankenexperiment utilizing quantum mechanical interferometers. It nicely shows where the idea for our experiment comes from. The model for the experiment is derived afterward using the description of the Mach-Zehnder interferometer. At the end of the chapter, the expected performance of the experiment is compared to alternative measurement methods that do not make use of weak value amplification with regard to noise.

3.1. How interferometers relate to the past of a particle

This section shortly introduces the quantum mechanical description of a Mach-zehnder interferometer. Then, the debate on a gedankenexperiment utilizing nested Mach-Zehnder interferometers is presented.

3.1.1. Quantum mechanical description of a Mach-Zehnder interferometer

An interferometer is an optical device which divides a light beam in two or more beams and overlaps them again, resulting in an interference of the two beam [10, 11]. Often, one of the beams obtains a phase difference that can be manipulated, resulting in a changing of the interference pattern.

In a Mach-Zehnder interferometer (MZI), as pictured in Fig. 3.1, the beams are divided by a beam splitter. The two beams are then each reflected at a mirror, before they are overlapped at a second beam splitter. At both output ports of the interferometer behind the beam splitter an interference emerges. It can be detected on a screen.

In general, the amplitude both beams in the interferometer have can be controlled, for example by adjusting the reflectance and transmittance of the beam splitter. Furthermore, the two beams have a relative phase if the two arms exhibit a path difference. This phase can be changed by, for example, inserting a glass

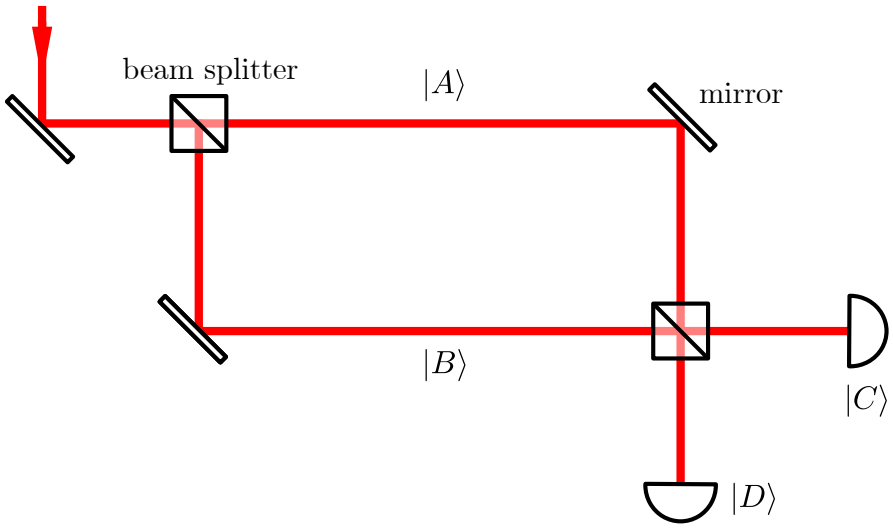

Figure 3.1.: A Mach-Zehnder interferometer. A beam is divided at a beam splitter. The two resulting beams are each reflected at a mirror before they are overlayed at a second beam splitter. This results in an interference at both output ports of the interferometer.

plate into one of the arms of the interferometer or by slightly moving one of the mirrors.

Using the formalism of quantum mechanics one can write the state of any interferometer as a sum of orthogonal states describing the arms of the interferometer [30]. In particular, the state of a quantum system inside a Mach-Zehnder interferometer is written as

$$|\psi\rangle = \cos\alpha\,|A\rangle + \sin\alpha e^{i\varphi}\,|B\rangle \tag{3.1}$$

where the particle being in the arms of the interferometer is described by two orthogonal states $|A\rangle$, $|B\rangle$. The parameter α adjusts the amplitude of the two beams and φ is the relative phase between the two beams. Note that this representation equals the representation of a qubit in Eq. 2.27.

The state of the particle in the output ports of the interferometer can be described by two orthogonal states

$$|C\rangle = \frac{1}{\sqrt{2}}(|A\rangle + |B\rangle) \tag{3.2}$$

$$|D\rangle = \frac{1}{\sqrt{2}}(|A\rangle - |B\rangle)\,. \tag{3.3}$$

With those states the intensity $I_{C/D}$ of the interfering beams at the output ports can be determined to be:

$$\begin{aligned} I_{C/D} &= \mathrm{Tr}[|\psi\rangle\langle\psi| \cdot |C/D\rangle\langle C/D|] \\ &= \frac{1}{2}[1 \pm 2\cos\alpha \sin\alpha \cos\varphi] \,. \end{aligned} \tag{3.4}$$

$I_C + I_D = 1$ because energy is conserved. For $\varphi = 0$ and $\alpha = \frac{\pi}{4}$ $|C\rangle$ is often called the "bright port" and $|D\rangle$ the "dark port".

In this equation we can see that the interference changes with the amplitudes and, more importantly, with the phase between the two beams. For certain φ the intensity is bright, while for others it is dark. The contrast of I is the greatest when both beams have the same amplitude, that is when $\alpha = \frac{\pi}{4}$. A measure of this contrast is the visibility of the interferometer

$$\mathcal{V} = \frac{I_{\max} - I_{\min}}{I_{\max} + I_{\min}} \,. \tag{3.5}$$

Here, $I_{\max}$ and $I_{\min}$ are defined as the maximal and minimal intensity over a period of φ. Using Eq. 3.4 this can be simplified to

$$\mathcal{V} = 2\cos\alpha \sin\alpha \,. \tag{3.6}$$

For interferometric experiments a visibility close to $\mathcal{V} = 1$ is desirable, as then the interferometer is perfectly aligned and tuned.

Particles in an interferometer might have more degrees of freedom than only the path-degree of freedom, that is being in the arms $|A\rangle$, $|B\rangle$. Other degrees of freedom might be longitudial or transversal spatial modes, polarization or certain spectra. If these degrees of freedom are the same for both arms at the output they can be ignored, if they differ they have to be taken into consideration. The state of the system inside the MZI can then be written as

$$|\psi\rangle = \cos\alpha\,|A\rangle \otimes |\chi_A\rangle + \sin\alpha e^{i\varphi}\,|B\rangle \otimes |\chi_B\rangle \,. \tag{3.7}$$

In this equation $|\chi_A\rangle$ and $|\chi_B\rangle$ conflate all possible additional degrees of freedom. The intensity at the output ports is then calculated [30]:

$$\begin{aligned} I_{C/D} &= \mathrm{Tr}\Big[|\psi\rangle\langle\psi| \cdot \Big(\,|C/D\rangle\langle C/D| \otimes \mathbb{1}\Big)\Big] \\ &= \frac{1}{2}[\cos^2\alpha + \sin^2\alpha \pm \cos\alpha \sin\alpha e^{i\varphi}\,\langle\chi_A|\chi_B\rangle \\ &\quad \pm \cos\alpha \sin\alpha e^{-i\varphi}\,\langle\chi_B|\chi_A\rangle] \\ &= \frac{1}{2}\Big[1 \pm 2\cos\alpha \sin\alpha \cos\varphi\,\mathrm{Re}[\langle\chi_A|\chi_B\rangle]\Big] \\ &= \frac{1}{2}\Big[1 \pm 2\cos\alpha \sin\alpha \cos\varphi\,\langle\chi_A|\chi_B\rangle\,\Big] \end{aligned} \tag{3.8}$$

if one includes the additional phase obtained from $\langle\chi_A|\chi_B\rangle$ into the relative phase φ. Then, the factor $\langle\chi_A|\chi_B\rangle := \gamma \in [0,1]$ defines the overlap or coherence of the two beams. It modulates the visibility to become

$$\mathcal{V} = 2\gamma \cos\alpha \sin\alpha \,. \tag{3.9}$$

Here, we can see that the visibility or the contrast is affected by the overlap of the degrees of freedom of the beams. This is important to note, as changes of the degrees of freedom can also decrease the visibility of the system.

3.1.2. The debate on the past of a particle

With the quantum mechanical description of the Mach-Zehnder interferometer it is possible to describe the debate surrounding another, more fundamental use of the weak value formalism.

Lev Vaidman argues that particles leave a "weak trace" where they have been due to the interaction with their environment [31]. Take for instance test particles placed near all possible paths of a photon. When the photon passes, Vaidman argues, a test particle gets a kick due to a local interaction with the photon, while it remains in its position when the photon does not pass it [31, 32]. The interaction is weak, so that the state of the test particles is only slightly disturbed. In this setting, the test particles act as the pointer of a measurement device [31] of a weak measurement. Hence, reading out all test particles provides information about the path of the photon because the trace the photon left is encoded in the test particles. Therefore, it is possible to determine the past of a particle [32].

Vaidman argues that the path of a pre- and postselected quantum particle can be described in the two-state vector formalism, namely that this quantum particle has been in all regions where the forward and backward-evolving wavefunctions overlap [32]. This weak trace is proportional to the weak value of the projection operator of the particle on a certain location since the interaction is local [31]. Therefore, by calculating the weak value, it is possible to determine the path a photon took: If it vanishes, the photons did not leave a trace there, that is it has not been there in the past, while it has been there when the weak value does not vanish.

This has counterintuitive consequences, explained in [31] with a gedankenexperiment. There, a nested interferometer is built: In one arm of a MZI another MZI is inserted. The inner interferometer is tuned such that its lower output port experiences total destructive interference, i.e. that in the arm of the outer interferometer behind it there is no light, see Fig. 3.2. At the three possible outputs of the interferometer, detectors are installed that click whenever they detect a photon.

Now, if only detector D_3 clicks, it is intuitive to assume that the photon passed through the beam splitter and then through the inner interferometer. Equivalently, for the click of the detector D_1, D_2 we intuitively assume that the photon

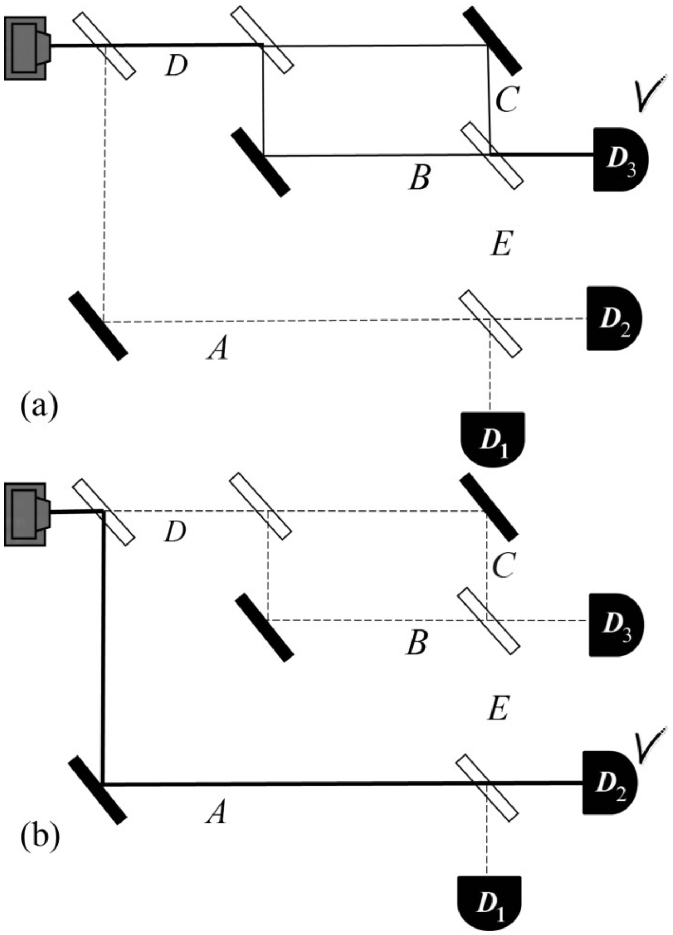

Figure 3.2.: A nested MZI. The lower output of the inner interferometer is tuned to destructive interference. The picture is taken from the paper which was the first formulation of the gedankenexperiment [31].

has only been in path A because the inner interferometer is tuned such that in path E is no light, i.e. a photon cannot be there. Hence, the only way it could possibly reach the detector would be through path A of the outer interferometer.

The weak values, however, tell a different story. In the two-state vector formalism the state inside the nested interferometer is

$$\langle\phi|\ |\psi\rangle = \frac{1}{\sqrt{3}}(\langle A| + \langle B| - \langle C|)\,\frac{1}{\sqrt{3}}(|A\rangle + |B\rangle + |C\rangle) \tag{3.10}$$

where the signs have been acquired due to phase shifts when reflecting from a mirror. Therefore, the weak value for a projector on arm A, $P_A = |A\rangle\langle A|$, is $(P_A)_w = \frac{\langle\phi|\hat{P}_A|\psi\rangle}{\langle\phi|\psi\rangle} = 1$, for a projection on arm B it is $(P_B)_w = 1$, for a projection on C it is $(P_C)_w = -1$ and for projections on D and E it vanishes.

We expected that the weak value of arm A would be non-vanishing. Surprisingly the weak values for arms B and C, that is the arms of the inner interferometer, also do not vanish, while the weak values for the arms D and E are zero as expected. This means that, according to Vaidman, the particle has been inside the inner interferometer but not in the paths connecting the inner interferometer with the outer one, as it has left no weak trace there!

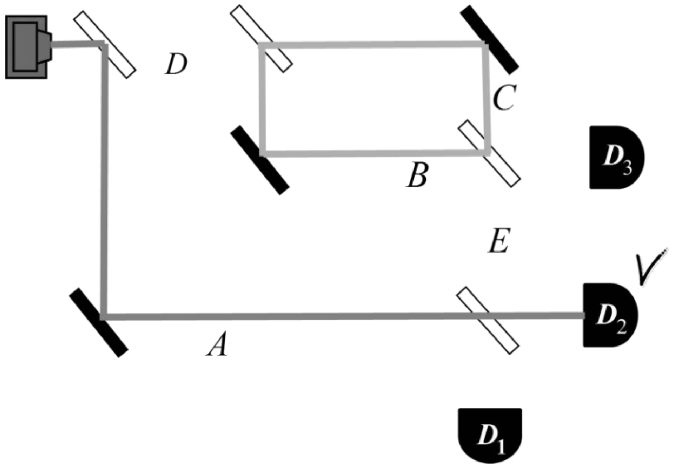

Figure 3.3.: The weak trace of the nested interferometer when detector D_1 or D_2 clicks. A trace can be observed in arm A as expected, but surprisingly also in the inner interferometer. The picture is taken from [31].

In Fig. 3.3 the overlap between the forward-evolving wave function and the backward-evolving wave function is shown. They overlap in the arms of the inner interferometer but not in the arms connecting the inner interferometer to the outer one. Hence, as calculated, the weak value of the projection onto the arms does not vanish. This effect can be explained well in the standard formalism of quantum mechanics. The weak coupling slightly changes the destructive interference so that a tiny part of the wave can leak into the arm E [33].

The gedankenexperiment was implemented in the laboratory by building a nested interferometer [34], as seen in Fig. 3.4. The mirrors of the interferometer are slightly vibrated with different frequencies, changing the path of the beams. Hence, the photons get a momentum kick from the local interaction with the mirror. On the detector the momentum kick is visible as an intensity change, which corresponds to the frequency of the vibration. Thus the photons reveal their interaction with the mirror. Consequently, the photons act as the pointer of the measurement device in this setting [32, 34].

In the experiment the frequency of the mirror wiggling was detected in the detector intensity. If the photons carried the frequency of one of the mirrors they were said to have been near the mirror. For the nested Mach-Zehnder with destructive interference at the output of the inner interferometer the result from

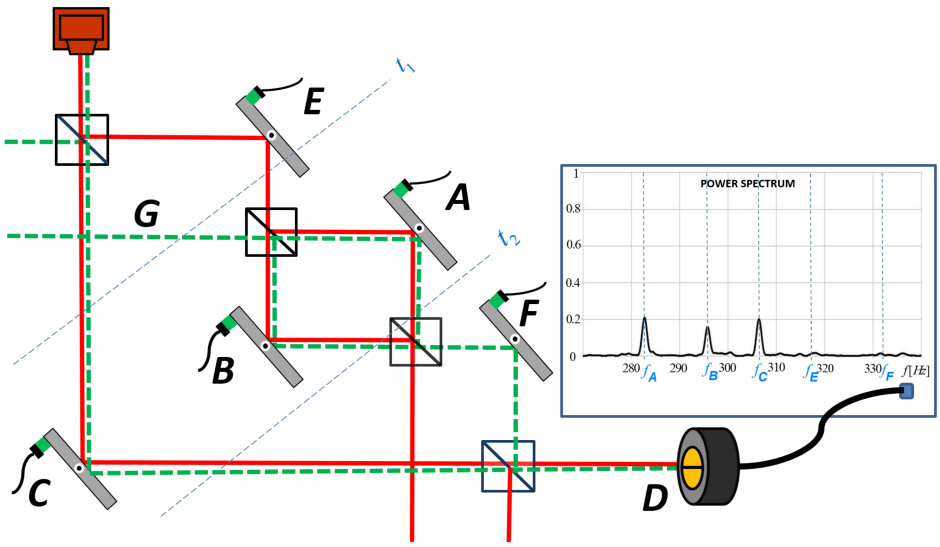

Figure 3.4.: The experimental realization of Vaidmans Gedankenexperiment. Mirrors are slightly vibrated and the resulting position change of the photons is read out as a frequency. The red line indicates the forwards evolving wave function and the green line the backward-evolving wave function. The result reveals no signal at the frequency of mirrors E and F. The picture is taken from [33].

the gedankenexperiment and the experiment in the laboratory agreed: In the detected signal the frequency of the mirrors of the inner interferometer was found, but not the frequency of the mirrors E and F connecting the inner interferometer to the outer one, as seen in Fig. 3.4 [34]. It was concluded that the photons have indeed been inside the inner interferometer but not in the arms connecting it with the outer one.

Both the gedankenexperiment and the experiment have sparked a longer debate [35–41]. One very prominent critique comes from Alonso and Jordan [42]. There, they argue that putting a Dove prism into one arm of the inner interferometer does not change the weak values of the projectors in an aligned interferometer. But now, when vibrating the mirrors, a frequency from mirror E can be seen in the signal [42], as shown in Fig. 3.5.

A Dove prism acts as a parity operator, reflecting a beam deflection around its axis [42]. Hence, the misalignment in mirror E is reflected due to the Dove prism. Thus, the interferometric stability of the interferometer is broken [42], resulting in the signal of mirror E appearing at the detector. However, following the weak trace argument, it is also thinkable that the past of the particle has been changed by the Dove prism [42]. If the Dove prism is inside the interferometer, the particles have not been at mirror E, but when it is inserted they have been at mirror E. Can a Dove prism really have this significant effect?

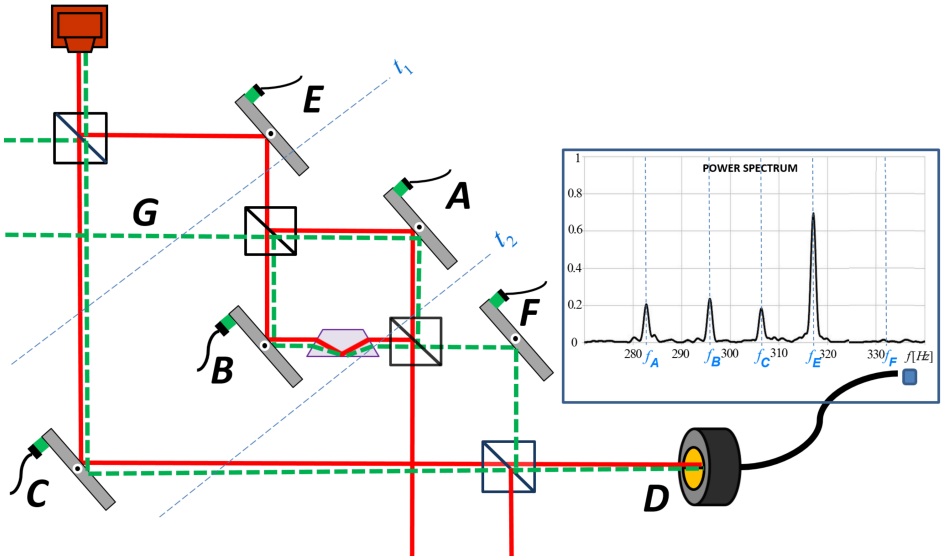

Figure 3.5.: The modified setup including a Dove prism of the experiment as proposed by [33]. A Dove prism is placed in the inner interferometer, resulting in the vibration of mirror E being detected. The picture is taken from [42].

In a response Vaidman et al. [33] argue that Alonso and Jordan have interpreted the result wrongly. The slight misalignment at mirror E introduces a small orthogonal component to the spatial mode of the photons, changing it from $|\chi_0\rangle$ to $\frac{1}{\sqrt{1+\varepsilon^2}}(|\chi_0\rangle + \varepsilon |\chi^\perp\rangle)$ with $\langle\chi_0|\chi^\perp\rangle = 0$. Inserting the Dove prism into this slightly misaligned interferometer indeed reveals a small presence of order ε^2 of the photons at mirror E [33], as claimed by [42], when calculating the weak value of the projector at mirror E with the resulting forward- and backward-evolving wave function. However, the weak trace results from all local interactions. In the case of the Dove prism the photons do not only interact with the mirror but also with the Dove prism, which mirrors the orthogonal mode, resulting in a change. Since the spatial mode of the photons acts as the pointer of the measuring device, the pointer is changed during this interaction. As a result, the faithful readout of the pointer, which should measure the weak interaction, is spoiled [33]. Hence, it is not enough to only consider the weak value of the projection on mirror E, but another operator $\hat{O}$ connecting the modes $|\chi_0\rangle$ and $|\chi^\perp\rangle$ has to be taken into account [33]. Calculating the weak value of the combined operator $\hat{O}\hat{P}_E$ reveals a presence of order ε at mirror E [33].

This explains why a signal of mirror E can be found when inserting a Dove prism. However, all other detected signals have been of order 1, while a wiggling of mirror F would also yield a signal of order ε [33]. How come only the signal at mirror E is detected? Arguably, the sensitivity towards mirror E has been enhanced, which results in a detected signal of order 1, while the true presence at

mirror E was of order ε^2. Considering also the interaction with the Dove prism, the presence is of order ε [33]. Vaidman et al. conclude that the particles have not been at mirror E but left a tiny trace there. However, changing the pointer by inserting the Dove prism enhanced the sensitivity of the detector for mirror E, which resulted in a stronger signal [33]. If the pointer was a test particle located at mirror E, the measurement would yield a presence of ε^2, which would not be detected.

They also state that the interferometer has become very sensitive towards misalignment of the incoming beam [33]. From this characteristic the idea for the experiment presented in this thesis arose: What if only the inner interferometer and mirror E are considered? Wiggling mirror E, that is changing the incident beam of the interferometer, should not yield a detectable signal. However, placing a Dove prism inside the interferometer should make the change of the incident beam observable at the detector due to the reflection of the orthogonal mode $\left|\chi^{\perp}\right\rangle$. The signal should be enhanced, as it was the case in the nested interferometer.

This results in several possible applications: First, in such an experiment, the enhancement of the signal at mirror E could be demonstrated. Second, the amplified signal could be evaluated to measure the deflection of the incident beam precisely. And third, since the deflection of the beam occurs before the interferometer, the setup could work as a "spying device", amplifying a signal created outside of the measurement device.

The following section models this proposed experiment theoretically. Furthermore, Chapter 4 explains the experimental implementation.

3.2. Model for interferometric measurement device

This section describes the model for the experimental setup. The main idea, with the experimental details being explained in Chapter 4, is the following: An mirror is slightly shifted, deflecting an laser beam by distance d and angle θ, as demonstrated in Fig. 3.6. This deflection can be determined using the method of weak value amplification. Therefore an interferometric setup is built as a measurement device. Instead of building the interferometer around the interaction, i.e. the displaced mirror so that the interaction happens inside the measurement device (as it was often deployed, see e.g. [5]) the interaction shall now take place *outside* of the interferometric measurement device. The setup is essentially the inner interferometer with mirror E of the (gendanken-)experiment introduced in Section 3.1.2.

The model for the setup has already been described in my bachelor thesis [43], using a Mach-Zehnder interferometer. Here, we will quickly summarize the model and write it down for the specific case of an interferometer with polarized arms, as we have chosen in our experiment. In this case we have to calculate with a

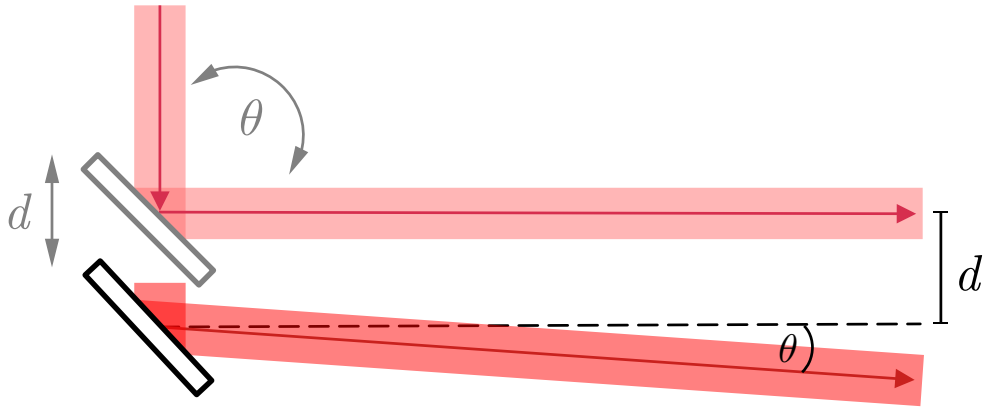

Figure 3.6.: A laser beam is sligthly defected by an angle θ and a distance d due to a mirror being shifted.

four-dimensional state, rather than a two-dimensional state, but the results for the weak value and the pointer deflection formula will be the very same.

If a beam enters a perfectly aligned interferometer the two resulting beams in the two arms have the same path length and interfere at the same spot again behind the interferometer. Therefore, even if the incident beam is displaced both resulting beams will have the same optical path because they experience the same initial deflection, as seen in Fig. 3.8a. This does not result in a change of the interference at the output, hence the weak value amplification method cannot be used. To use weak value amplification one has to deflect one beam relative to each other.

This can done by inserting a Dove prism into one of the arms of the interferometer. A Dove prism mirrors a beam along its axis, which means that a beam with spatial displacement d and angular displacement θ will get an displacement $-d$ and $-\theta$, as shown in Fig. 3.7. Deflection $d = 0$ and $\theta = 0$ are hereby defined as the beam propagating perfectly on the axis of the Dove prism. At the output port one beam will have a deflection d and θ due to the initial deflection, while the other beam will experience a displacement $-d$ and rotation $-\theta$ due to the action of the Dove prism as seen in 3.8b. Two spatially separated beams are hence overlapped behind the interferometer, resulting in an change of the initial interference.

In Fig. 3.7 a deflection in x-direction is shown. It is important to note that deflections in y-direction are not mirrored by the Dove prism. The Dove prism introduces a spatial offset to the beam, without changing the propagation direction. Hence, to mirror y deflections the Dove prism has to be rotated by 90°.

In the experiment presented in this thesis the spatial mode of the laser beam is modeled as the pointer of the weak value formalism. This means that the deflection of the spatial mode of the laser beam outside of the interferometer is

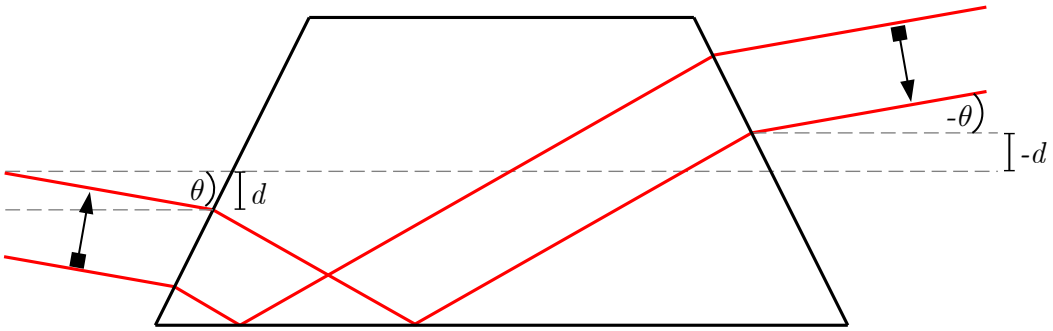

Figure 3.7.: A dove prism mirrors a beam along its axis. A beam with initial deflection d and θ will have a deflection $-d$ and $-\theta$ after the Dove prism.

modeled as a deflection of the pointer. This pointer deflection is described as a change of the initial pointer state $|\Phi_0\rangle$, as in [8, 33]:

$$|\Phi_0\rangle \to |\Phi'\rangle = \eta(|\Phi_0\rangle + \varepsilon \left|\Phi^\perp\right\rangle) \tag{3.11}$$

where $\left\langle\Phi_0\middle|\Phi^\perp\right\rangle = 0$, $\varepsilon \geq 0$ for simplicity and $\eta = \langle\Phi'|\Phi_0\rangle = \frac{1}{\sqrt{1+\varepsilon^2}}$ is the overlap between the initial and deflected mode. We assume that the outside interaction can be written as an operator

$$e^{-i\hat{B}} = \exp\left[-i(\varepsilon_x \hat{k} - \varepsilon_k \hat{x})\right] . \tag{3.12}$$

where ε_x is the spatial deflection of the beam and ε_k is the angular deflection of the beam. Here, as in Chapter 2 we set that $\hbar = 1$.

The initial state of the system, i.e. the interferometer is given by

$$|\psi\rangle = \cos\alpha\,|H\rangle \otimes |A\rangle + \sin\alpha\,|V\rangle \otimes |B\rangle \ . \tag{3.13}$$

Here, to create this state, incoming light with polarization $|V\rangle$ was rotated to $\cos\alpha\,|H\rangle + \sin\alpha\,|V\rangle$ with a half-wave plate. The polarizing beam splitter behind it then splits the beam into two beams, resulting in the given entangled state, where the horizontal component travels in an arm labeled "A" and the vertical component in an arm labeled "B".

The deflected pointer state enters the interferometer and therefore the total state of system and pointer can be written as a state

$$\cos\alpha\,|HA\rangle \otimes |\Phi'\rangle + \sin\alpha\,|VB\rangle \otimes |\Phi'\rangle \ . \tag{3.14}$$

Therefore, after the beam has entered the interferometer both arms of the interferometer experience the same deflection and overlap at the same spot on the output port. In this case the weak value amplification cannot be used.

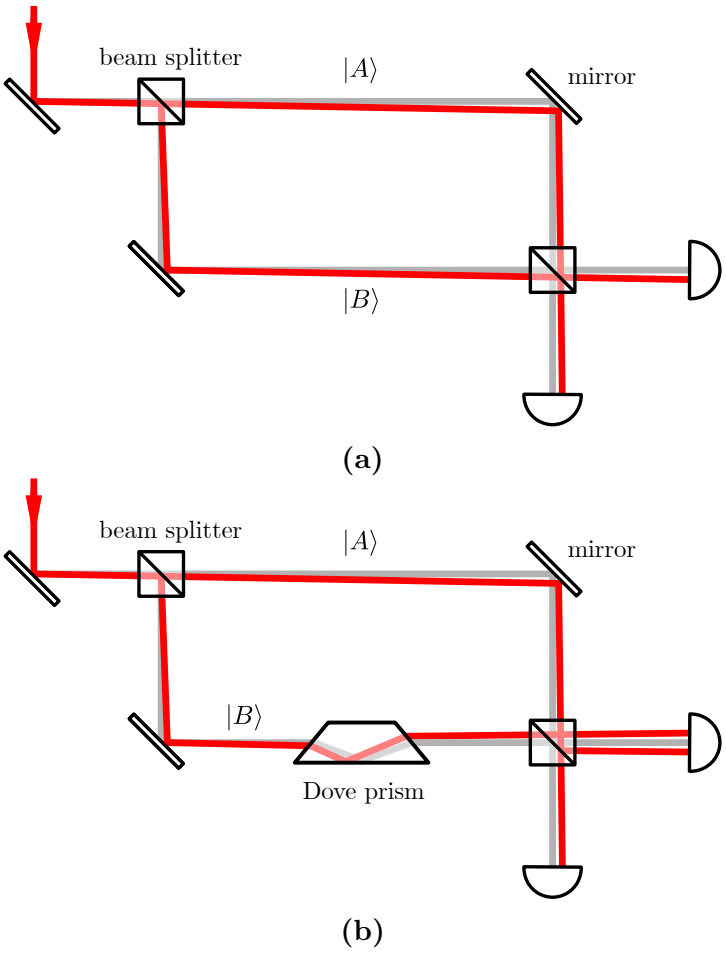

Figure 3.8.: (a) In an aligned interferometer both arms will have the same optical path, even if the incoming beam is initially displaced. (b) Inserting a Dove prism into one of the arms will introduce a relative deflection between the two resulting beams.

The interaction with the Dove prism inserted into arm $j \in \{A, B\}$ of the interferometer can be modeled as a unitary

$$\begin{aligned} \hat{U} &= \mathbb{1} \otimes \hat{P}_i \otimes \mathbb{1} + \mathbb{1} \otimes \hat{P}_j \otimes \hat{D} \quad \text{acting on} \\ &\mathcal{H}_{\text{polarization}} \otimes \mathcal{H}_{\text{arm}} \otimes \mathcal{H}_{\text{pointer}} = \mathcal{H}_{\text{system}} \otimes \mathcal{H}_{\text{pointer}} \,. \end{aligned} \tag{3.15}$$

In this equation $i, j \in \{A, B\}$, $i \neq j$. $(\mathbb{1} \otimes \hat{P}_i) := \hat{P}_i$ is the projector acting on arm i, where it leaves the polarization unaffected. Because it is a projector $\hat{P}_i + \hat{P}_j = \mathbb{1}$ holds. $\hat{D}$ is an hermitian operator describing the action of the Dove prism in arm j: The Dove prism leaves a beam which propagates on its axis unaffected, and will mirror any propagation off the axis. In terms of the initial and deflected pointer we can model the operator as

$$\hat{D} \left|\Phi_0\right\rangle = \left|\Phi_0\right\rangle \tag{3.16}$$

$$\hat{D} \left|\Phi^{\perp}\right\rangle = -\left|\Phi^{\perp}\right\rangle \tag{3.17}$$

which also implies that

$$\hat{D}\left|\Phi'\right\rangle = \hat{D}e^{-i\hat{B}}\left|\Phi_0\right\rangle = \eta\hat{D}(\left|\Phi_0\right\rangle + \varepsilon\left|\Phi^{\perp}\right\rangle) \tag{3.18}$$

$$= \eta(\left|\Phi_0\right\rangle - \varepsilon\left|\Phi^{\perp}\right\rangle) = e^{i\hat{B}}\left|\Phi_0\right\rangle \tag{3.19}$$

as calculated in [43].

After the beam has left the Dove prism the total state of system and pointer is expressed as a state

$$\hat{U}[\left|\psi\right\rangle \otimes \left|\Phi'\right\rangle] = \cos\alpha\left|HA\right\rangle \otimes \left|\Phi'\right\rangle + \sin\alpha\left|VB\right\rangle \otimes \hat{D}\left|\Phi'\right\rangle \tag{3.20}$$

given that the Dove prism is inserted into arm B. If it was in arm A the Dove operator $\hat{D}$ would be found in the first term, which would lead to the same density matrix.

Eq. 3.20 is an entangled state between the Hilbert space of the system and the Hilbert space of the pointer. The reduced state of the system is therefore a mixed state. The equation for the weak value Eq. 2.50 can however only be used for pure states. The weak value of an arbitrary operator $\hat{A}$ for the case of mixed states is given in [8] as

$$(\hat{A})_w = \frac{\mathrm{Tr}\left[\left|\phi\right\rangle\!\left\langle\phi\right|\hat{A}\hat{\rho}\right]}{\mathrm{Tr}[\left|\phi\right\rangle\!\left\langle\phi\right|\hat{\rho}]}\,. \tag{3.21}$$

We therefore need to find the density matrix of the system to calculate the weak value. The density matrix $\hat{\rho}_{\mathrm{system}} := \hat{\rho}$ of the system can be found by calculating the partial trace for the pointer over the total system Eq. 3.20:

$$\begin{aligned}\hat{\rho} &= \mathrm{Tr}_{\mathrm{pointer}}[\hat{\rho}_{\mathrm{total}}] \\ &= \cos^2\alpha\left|HA\right\rangle\!\left\langle HA\right| + \cos\alpha\sin\alpha\gamma\left|HA\right\rangle\left\langle VB\right| \\ &\quad + \cos\alpha\sin\alpha\gamma\left|VB\right\rangle\left\langle HA\right| + \sin^2\alpha\left|VB\right\rangle\!\left\langle VB\right|\,.\end{aligned} \tag{3.22}$$

In this expression γ is the overlap between the two shifted beams, which is

$$\gamma = \left\langle\Phi'\right|\hat{D}\left|\Phi'\right\rangle = e^{-\frac{2\varepsilon_x^2}{w_0^2}}e^{-\frac{1}{2}w_0\varepsilon_k^2}\,. \tag{3.23}$$

It can be calculated using the initial Gaussian pointer state in position space $\Phi_0(x) = \mathcal{N}\exp\left(-\frac{x^2}{w_0^2}\right)$ and in momentum space $\Phi_0(k) = \mathcal{M}\sqrt{\frac{w_0^2}{2}}\exp\left(-\frac{1}{4}w_0^2k^2\right)$.

Behind the interferometer a postselection on state

$$\left|\phi\right\rangle = \frac{1}{2}(\left|H\right\rangle + e^{i\varphi}\left|V\right\rangle) \otimes (\left|A\right\rangle + \left|B\right\rangle) \tag{3.24}$$

is performed. In our interferometric setup the relative phase between the two beams is introduced just after the interferometer with a quarter-wave plate and a

linear polarizer. This is effectively a postselection onto the given state, which is why we introduce the phase in the postselection state $|\phi\rangle$. Using Eq. 3.21 we can calculate the weak values for the operators $\hat{P}_A$ and $\hat{P}_B$:

$$(P_A)_w = \frac{1+\tan\alpha\gamma e^{i\varphi}}{1+\tan^2\alpha+2\tan\alpha\gamma\cos\varphi} \tag{3.25}$$

$$(P_B)_w = \frac{1+\cot\alpha\gamma e^{-i\varphi}}{1+\cot^2\alpha+2\cot\alpha\gamma\cos\varphi}\,. \tag{3.26}$$

Performing a postselection on the state $|\phi\rangle$ will yield the final state of the pointer:

$$\begin{aligned}
|\Phi_F\rangle &= \mathcal{N}\langle\phi|\,(\hat{U}\big[|\psi\rangle\,|\Phi'\rangle\big]) \\
&= \mathcal{N}\langle\phi|\Big(\big[\mathbb{1}\otimes(\mathbb{1}-\hat{P}_j)\otimes\mathbb{1}+\mathbb{1}\otimes\hat{P}_j\otimes\hat{D}\big]\,|\psi\rangle\otimes|\Phi'\rangle\Big) \\
&= \mathcal{N}\langle\phi|\psi\rangle\,\big[\mathbb{1}-\frac{\langle\phi|\,\mathbb{1}\otimes\hat{P}_j\,|\psi\rangle}{\langle\phi|\psi\rangle}+\frac{\langle\phi|\,\mathbb{1}\otimes\hat{P}_j\,|\psi\rangle}{\langle\phi|\psi\rangle}\hat{D}\big]\,|\Phi'\rangle \\
&= \mathcal{N}\langle\phi|\psi\rangle\,\big[\mathbb{1}-(P_j)_w\mathbb{1}+(P_j)_w\hat{D}\big]\,|\Phi'\rangle \\
&= |\Phi_0\rangle+\varepsilon\left|\Phi^\perp\right\rangle-2\varepsilon(P_j)_w\left|\Phi^\perp\right\rangle\,.
\end{aligned} \tag{3.27}$$

The shift of the expectation of an arbitrary pointer observable $\hat{O}$ can be calculated to be

$$\begin{aligned}
\delta O &= \langle\Phi_F|\,\hat{O}\,|\Phi_F\rangle-\langle\Phi_0|\,\hat{O}\,|\Phi_0\rangle \\
&= 2\varepsilon\,\mathrm{Re}[\langle\Phi_0|\,\hat{O}\left|\Phi^\perp\right\rangle]-4\varepsilon\,\mathrm{Re}[(P_j)_w\,\langle\Phi_0|\,\hat{O}\left|\Phi^\perp\right\rangle]\,.
\end{aligned} \tag{3.28}$$

Normalizing $\left|\Phi^\perp\right\rangle$ with respect to $|\Phi'\rangle$ and $|\Phi_0\rangle$ yields

$$\left|\Phi^\perp\right\rangle=\frac{i\langle\hat{B}\rangle_0\mathbb{1}-i\hat{B}}{\Delta B}\,|\Phi_0\rangle\;, \tag{3.29}$$

where $\langle\hat{B}\rangle_0=\langle\Phi_0|\,\hat{B}\,|\Phi_0\rangle$ and $\Delta B^2=\langle\hat{B}^2\rangle_0-\langle\hat{B}\rangle_0^2$. Using this it is possible to find that $\left\langle\Phi^\perp\middle|\Phi'\right\rangle=\eta\varepsilon=\Delta B$. Neglecting higher orders of ε_x and ε_k the relationship between ε and ΔB is $\frac{\varepsilon}{\Delta B}\approx 1$.

Making use of these relationships the pointer shift for the spatial displacement $\hat{x}$ and the angular displacement $\hat{k}$ can be calculated by plugging these operators into Eq. 3.28. We arrive at

$$\delta x = \varepsilon_x-2\varepsilon_x\,\mathrm{Re}[(P_j)_w]+4\varepsilon_k\,\mathrm{Im}[(P_j)_w]\Delta x^2 \tag{3.30}$$

$$\delta k = \varepsilon_k-2\varepsilon_k\,\mathrm{Re}[(P_j)_w]-4\varepsilon_x\,\mathrm{Im}[(P_j)_w]\Delta k^2\,. \tag{3.31}$$

Since in the actual experiment we will introduce a beam deflection both in x-direction and in y-direction, we have to extend the model to three dimensions. We

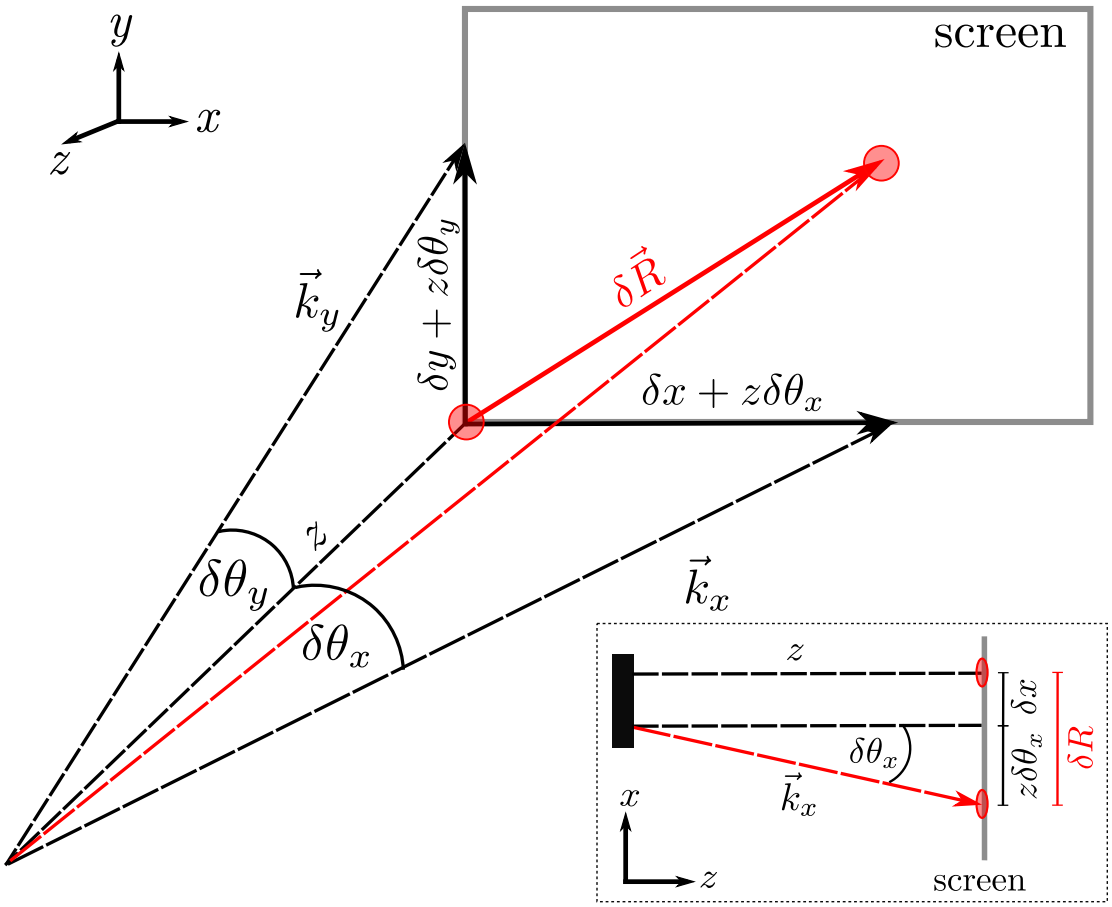

Figure 3.9.: On the screen the pointer shift is expressed as $\delta\vec{R}$, which is a combination of a shift in x- and a shift in y-direction. Each shift is furthermore a combination of spatial displacement $\delta_x = \frac{\delta k_x}{|\vec{k}_x|}$, $\delta_y = \frac{\delta k_y}{|\vec{k}_y|}$ and angular displacement $\delta\theta_x$, $\delta\theta_y$. z is the distance from the waist of the beam to the detectors. The small picture in the right corner depicts the deflection in only one dimension.

can model the interaction in x-direction as an operator $\hat{B}_x = \varepsilon_x \hat{k}_x - \varepsilon_{k_x}\hat{x}$ and the y-direction interaction as $\hat{B}_y = \varepsilon_y \hat{k}_y - \varepsilon_{k_y}\hat{y}$. Both are independent of each other. We further assume that a Dove prism is placed in each arm of the inferferometer to measure the x and y deflection respectively. As the interaction operators are independent of each other one can just act the two operators on the preselection state Eq. 3.13 with the according unitary $\hat{U}$ and calculate the shift of the pointer state for x and y independently of each other. Assuming that the operator $\hat{P}_A$

determines the deflection in x direction and P_B in y direction the results are given as

$$\begin{aligned}
\delta x &= \varepsilon_x - 2\varepsilon_x \operatorname{Re}[(P_A)_w] + 4\varepsilon_{k_x} \operatorname{Im}[(P_A)_w]\Delta x^2 && (3.32)\\
\delta k_x &= \varepsilon_{k_x} - 2\varepsilon_{k_x} \operatorname{Re}[(P_A)_w] - 4\varepsilon_x \operatorname{Im}[(P_A)_w]\Delta k_x^2 && (3.33)\\
\delta y &= \varepsilon_x - 2\varepsilon_y \operatorname{Re}[(P_B)_w] + 4\varepsilon_{k_y} \operatorname{Im}[(P_B)_w]\Delta y^2 && (3.34)\\
\delta k_y &= \varepsilon_{k_y} - 2\varepsilon_{k_y} \operatorname{Re}[(P_B)_w] - 4\varepsilon_y \operatorname{Im}[(P_B)_w]\Delta k_y^2 \,. && (3.35)
\end{aligned}$$

We can express the two dimensional pointer shift $\delta\vec{R}$ detected at the screen as a combination of a shift in x-direction and a shift in y-direction. Each shift is furthermore a combination of a spatial displacement δ_x, δ_y and an angular displacement

$$\delta\theta_x = \frac{\delta k_x}{|\vec{k_x}|}\,, \quad \delta\theta_y = \frac{\delta k_y}{|\vec{k_y}|}\,, \tag{3.36}$$

as seen in Fig. 3.9. Considering the distance z from the waist of the beam to the detector, we can therefore write the pointer shift as

$$\delta\vec{R} = \begin{bmatrix} \delta x + z\delta\theta_x \\ \delta y + z\delta\theta_y \end{bmatrix}\,. \tag{3.37}$$

Using that the properties of the (Gaussian) beam

$$\Delta k_x^2 = \Delta k_y^2 = \frac{1}{w_0}\,, \quad \Delta x^2 = \Delta y^2 = \frac{w_0^2}{4}\,, \quad z_R = \frac{\pi w_0^2}{\lambda} \tag{3.38}$$

and the terms for the deflection

$$\varepsilon_x = d_x\,, \quad \varepsilon_y = d_y\,, \quad \varepsilon_{k_x} = \frac{2\pi}{\lambda}\theta_x \quad \text{and} \quad \varepsilon_{k_y} = \frac{2\pi}{\lambda}\theta_y \tag{3.39}$$

we arrive at the formula for the deflection:

$$\delta\vec{R} = \begin{bmatrix} d_x + z\theta_x \\ d_y + z\theta_y \end{bmatrix} - \begin{bmatrix} (2d_x + 2z\theta_x)\operatorname{Re}[(P_A)_w] \\ (2d_y + 2z\theta_y)\operatorname{Re}[(P_B)_w] \end{bmatrix} + \begin{bmatrix} (2z_R\theta_x - 2\frac{z}{z_R}d_x)\operatorname{Im}[(P_A)_w] \\ (2z_R\theta_y - 2\frac{z}{z_R}d_y)\operatorname{Im}[(P_B)_w] \end{bmatrix}\,. \tag{3.40}$$

Alternatively, we can also model the deflection as the two arms of the interferometer being displaced, one in positive and one in negative direction. In this case the interaction would be modeled by the interferometer, using the Pauli-z operator $\hat{\sigma}_z$ which displaces both arms inside the interferometer. The interaction unitary is then given by

$$\hat{U}_{\sigma_z} = \exp\left[-i\hat{\sigma}_z \otimes \hat{B}\right] \quad \text{acting on} \mathcal{H}_{\text{system}} \otimes \mathcal{H}_{\text{pointer}} \tag{3.41}$$

where $\hat{B} = \varepsilon_x\hat{k} - \varepsilon_k\hat{x}$ as in the model presented.

This model is equivalent to the model presented above. This can be seen by transforming the total interaction of the model presented previously, $\hat{U}e^{-i\hat{B}}$ into the interaction that uses the Pauli-z operator:

$$\begin{aligned}
\hat{U}e^{-i\hat{B}} &= \left[\hat{P}_A \otimes \mathbb{1} + \hat{P}_B \otimes \hat{D}\right] e^{-i\hat{B}} \\
&= \hat{P}_A \otimes e^{-i\hat{B}} + \hat{P}_B \otimes \hat{D}e^{-i\hat{B}} \\
&= \hat{P}_A \otimes e^{-i\hat{B}} + \hat{P}_B \otimes e^{i\hat{B}} \\
&= \sum_{i\in\{A,B\}} \hat{P}_i \otimes e^{-ia_i\hat{B}} \\
&= \exp\left[-i\hat{\sigma}_z \otimes \hat{B}\right] \\
&= \hat{U}_{\sigma_z} \,. \qquad (3.42)
\end{aligned}$$

Here, we have used the spectral decomposition of σ_z,

$$\hat{\sigma}_z = \hat{P}_A - \hat{P}_B \qquad (3.43)$$

with its eigenvalues $a_A = +1$ and $a_B = -1$, corresponding to the projectors on arm A and and B.

The deflection can also be modeled with an interaction

$$\hat{U}_{-\sigma_z} = \exp\left[-i(-\sigma_z) \otimes \hat{B}\right] \qquad (3.44)$$

with eigenvalues $a_A = -1$ and $a_B = +1$. It corresponds to the beams being deflected opposite to the deflection introduced by $\hat{\sigma}_z$. It is manifested in different weak values:

$$(\sigma_z)_w = \frac{1 - \tan^2\alpha + \tan\alpha\gamma\,(e^{-i\varphi} - e^{i\varphi})}{1 + \tan^2\alpha + 2\gamma\tan\alpha\cos\varphi} \qquad (3.45)$$

$$(-\sigma_z)_w = \frac{1 - \cot^2\alpha + \cot\alpha\gamma\,(e^{i\varphi} - e^{-i\varphi})}{1 + \cot^2\alpha + 2\gamma\cot\alpha\cos\varphi} \,. \qquad (3.46)$$

The pointer shift for both interactions is given by

$$\delta R = d\,\mathrm{Re}[A_w] - z_R\theta\,\mathrm{Im}[A_w] + z\theta\,\mathrm{Re}[A_w] + \frac{z}{z_R}d\,\mathrm{Im}[A_w] \qquad (3.47)$$

where A_w either $(\sigma_z)_w$ or $(-\sigma_z)_w$.

Note that $-(\sigma_z)_w = (-\sigma_z)_w$, hence the pointer shift with weak value $(\sigma_z)_w$ has opposite sign of the shift for weak value $(-\sigma_z)_w$.

3.3. Comparison with alternative measurement methods

Beam displacements do not necessary have to be measured using weak value amplification. In fact, building such an interferometric measurement device seems

rather tedious compared to, for example, amplifying the displacement using a lens. This section summarizes the controversial debate on the merits of weak value amplification. Subsequently, three different measuring methods are described and their advantages scrutinized.

3.3.1. The debate on the merits of weak value amplification

Weak value amplification allows to enhance small interactions and measure them precisely. Many experiments have successfully made use of this principle, for example [4–9].

However, one has a price to pay, namely, throwing away much of the ensemble in the postselection process. This has led to a controversial debate about the merits of weak value amplification.

All studies about weak value amplification and postselected weak measurements agree that weak value amplification does not increase the signal-to-noise ratio compared to strong measurements [44, 45]. Some studies question the usefulness of weak value amplification as a whole, arguing that postselection does not enhance the precision of a measurement and weak measurements are not more precise than strong measurements [46]. According to [47] weak-value amplification is suboptimal for detecting or estimating interaction parameters.

Others point out the technical advantages weak value amplification might have: Certain technical noises could be suppressed using weak value amplification [44, 45, 48], a result which has also been challenged [49]. Weak value amplification experiments use low intensities to gain high amplification and could therefore use highly sensitive detectors, as they would not be saturated [44, 45, 49, 50]. Weak value amplification could also increase the sensitivity of the detector [50]. [45] also argues that weak value amplification allows using beams with a larger radius. [51] present a simple example where weak value amplification makes measurement of an otherwise inaccessible physical parameter possible.

The following subsections compare the weak value amplification experiment of this thesis with two alternative measurement methods in regard of noise.

3.3.2. Signal-to-noise ratio for three methods

Signal-to-noise ratio The signal-to-noise ratio (SNR) is a quantity which specifies the quality of a signal compared to the present background noise. The higher the SNR the clearer the signal is.

In general the signal-to-noise ratio is defined as the ratio of the signal power to the noise power [12],

$$\mathcal{SNR} = \frac{I_{\text{signal}}}{I_{\text{noise}}} \,. \tag{3.48}$$

A $\mathcal{SNR} > 1$ means that a signal rises above the noise, which is desirable.

The signal-to-noise ratio for the displacement measurement of a Gaussian intensity distribution $I(x) = \frac{1}{\sqrt{2\pi}\sigma} \exp(-x^2/2\sigma^2)$ is given by [45, 52]:

$$\mathcal{SNR} = \frac{\frac{\sqrt{2}Nd}{\sqrt{\pi}\sigma}}{\sqrt{N}} = \sqrt{\frac{2}{\pi}}\frac{\sqrt{N}d}{\sigma} \tag{3.49}$$

where N is the number of photon counts at the detector, d is the projection of the displacement on the detector and σ is the beam radius of the intensity distribution at the detector. Note that the beam radius is defined as the standard deviation of the intensity distribution. In Eq. 3.49 we see that the noise scales with $\sqrt{N}$. This can be attributed to the fact that photon number counting constitutes as a Poisson process [12]. Eq. 3.49 can also be understood as the beam radius σ introducing the noise: An intensity distribution with large extent cannot be measured as precise as an intensity distribution with small extent.

It is important to note that the intensity distribution for a Gaussian beam as defined in Eq. 2.4 is $I = \frac{\sqrt{2}}{\sqrt{\pi}w(z)} \exp(-2x^2/w(z))$. The beam radius at the detector is defined as twice the standard deviation, $w(z) = 2\sigma$. With this definition the SNR can be expressed as

$$\mathcal{SNR} = \sqrt{\frac{8}{\pi}}\frac{\sqrt{N}d}{w(z)}\,. \tag{3.50}$$

In this equation z is the distance from the waist of the beam to the detector.

The goal of the experiment modeled in Section 3 is to measure small beam displacements d and θ. The signal-to-noise ratio is now compared for the weak value amplification method presented in this thesis and two alternative methods.

Far field measurement: Measurement of beam in far field If one slightly deflects the beam by an angle θ and puts up a detector in the far field at distance L the deflection of the beam constitutes a position change on the detector, as seen in Fig. 3.10. For small angular displacements the distance to the initial position is $L\theta$. Assuming that the beam is deflected at the waist, the waist at the detector $w(L)$ is $w(L) = \sqrt{w_0^2 + L^2\theta_{\text{div}}^2}$, having used that $\theta_{\text{div}} = w_0/z_R$. For large L we can approximate that $w(L) = L\theta_{\text{div}}$. With this the signal-to-noise ratio becomes

$$\mathcal{SNR}_{\text{farfield}} = \sqrt{\frac{8}{\pi}}\frac{\sqrt{N}L\theta}{L\theta_{\text{div}}} = \frac{\sqrt{N}\theta}{\theta_{\text{div}}}\,. \tag{3.51}$$

Note here that $\mathcal{SNR}_{\text{farfield}} > 1$ if $\sqrt{N}\theta > \theta_{\text{div}}$. This is the case for large deflections θ and a collimated beam with a small divergence angle, or a large number of detected photons. For large divergence angles the deflection gets lost in the uncertainty of the beam.

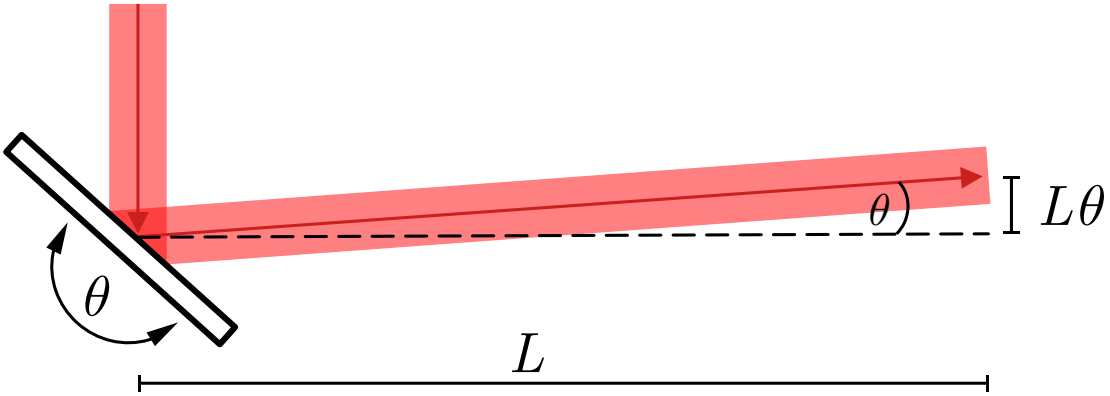

Figure 3.10.: Without any additional components the beam deflection θ is detected as a position change $L\theta$ on a screen at distance L in the far field.

Lens measurement: Amplification of deflection with lens Another method uses a lens with focal length f to amplify the beam deflection, as depicted in Fig. 3.11. The detector can then be put closer to the mirror that introduces the beam displacement. At the waist of the beam the angular deflection is the initial deflection θ. The lens is placed so close to the detector that the spatial displacement at the waist can be neglected. The detector is placed at the focus of the lens, because there the angular displacements of a beam become visible. The angular displacement is detected as a shift $f\theta$ on the sensor because the lens images the deflection and amplifies it therefore. Any spatial beam displacements are not visible in the focus. The waist of a Gaussian beam after a lens is fw_0/z_R. Putting this into Eq. 3.50, we get

$$\mathcal{SNR}_{\text{lens}} = \sqrt{\frac{8}{\pi}}\frac{\sqrt{N}f\theta}{\frac{fw_0}{z_R}} = \sqrt{\frac{8}{\pi}}\frac{\sqrt{N}\theta}{\theta_{\text{div}}} \tag{3.52}$$

which is the same SNR as for the first method. This result is interesting, as it shows the effect of a lens: Angular displacements of a naked beam can hardly be seen in the near field, whereas spatial deflections are seen in the near field and get lost in the far field due to the divergence of the beam. A lens images the angular deflection to the near field. In contrast, spatial deflections imaged with the lens cannot be detected in the focus of the lens, but rather behind the focus - the spatial deflection is imaged into the far field.

Weak value amplification: Amplification of deflection with weak value amplification The third method to measure the beam displacement is the interferometric weak value amplification method presented in Section 3. The displacement detected at the screen is a function of the weak value A_w. In weak value amplification only a fraction of photons contribute to the signal, because the postselection

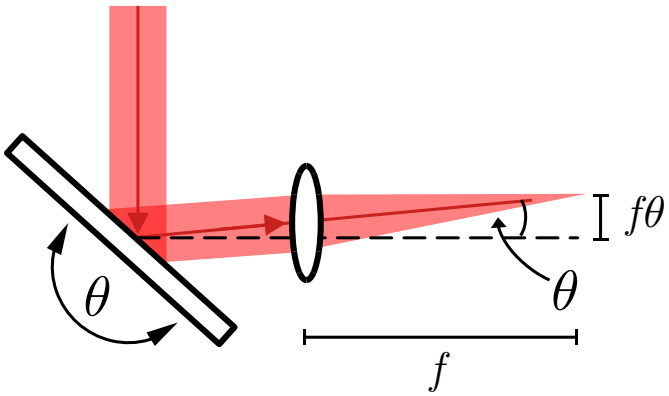

Figure 3.11.: When using a lens with focal length f the beam deflection θ is detected as a position change $f\theta$ on a screen close to the lens.

ignores most of the detectable photons. This is in contrast to the two other measurement methods, where all photos reaching the detector contribute to the signal. Hence, using weak value amplification the photon number at the detector N has to be rescaled by the postselection probability, which is given by

$$P_{\mathrm{ps}} = |\langle\phi|\psi\rangle|^2 \tag{3.53}$$

with the initial state of the system $|\psi\rangle$ and the final state $|\phi\rangle$ onto which the system is projected.

The signal-to-noise ratio of any weak value amplification method is at best as high as the signal-to-noise ration of the two other methods, often worse. Intuitively this is understood by considering a weak value amplified pointer shift of dA_w, where d is the deflection of the far field measurement and A_w is the weak value. This is the case if the weak value is real, as then the pointer shift Eq. 2.52 simplifies to that form. The signal-to-noise ratio is calculated by substituting d by dA_w and N by $P_{\mathrm{ps}}N$ into Eq. 3.50:

$$\mathcal{SNR}_{\mathrm{wva}} = \sqrt{\frac{8}{\pi}}\frac{\sqrt{NP_{\mathrm{ps}}}\,dA_w}{w(z)} = \sqrt{\frac{8}{\pi}}\frac{\sqrt{NP_{\mathrm{ps}}}\,d\frac{\langle\phi|\hat{A}|\psi\rangle}{\sqrt{P_{\mathrm{ps}}}}}{w(z)} = \sqrt{\frac{8}{\pi}}\frac{\sqrt{N}\,d\,\langle\phi|\,\hat{A}\,|\psi\rangle}{w(z)} \tag{3.54}$$

The parameter $\langle\phi|\,\hat{A}\,|\psi\rangle$ can be made 1 for two level systems [9, 44]. In this case the SNR for weak value amplification is as good as the SNR when measuring the beam in the far field or when amplifying the deflection with a lens. If $\langle\phi|\,\hat{A}\,|\psi\rangle < 1$ it is worse.

This can be demonstrated with the experiment introduced in Section 3. The shift detected at the detector is given by Eq. 3.47,

$$\delta R = (x + z\vartheta)\,\mathrm{Re}[(\sigma_z)_w] + (\frac{z}{z_R}x - z_R\vartheta)\,\mathrm{Im}[(\sigma_z)_w]\,. \tag{3.55}$$

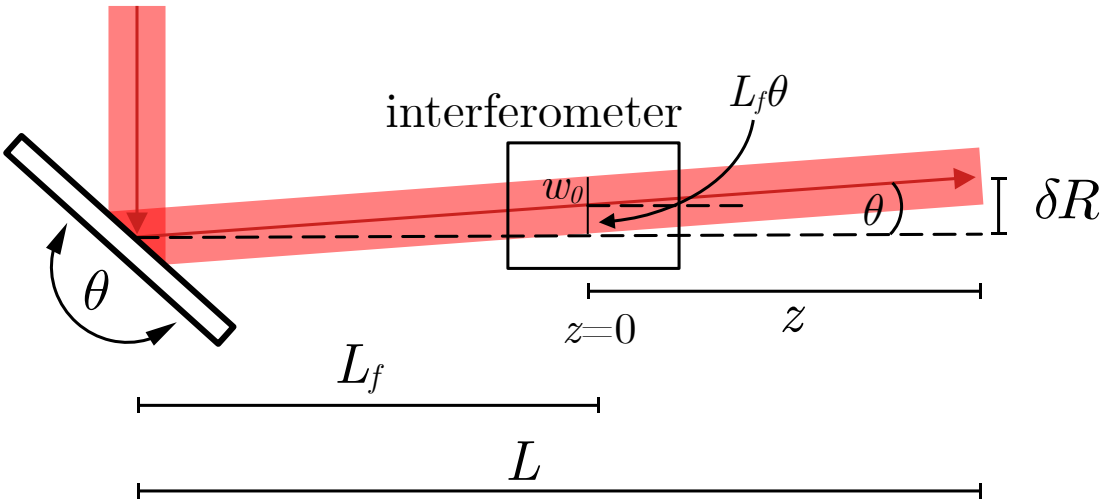

Figure 3.12.: Using interferometric weak value amplification the beam deflection θ is detected as a position change δR on a screen. L is the distance between the mirror and the screen, L_f the distance between the mirror and the waist of the beam and z is the distance between the waist and the screen. At the waist the beam is also spatially deflected by $L_f\theta$.

It is crucial to understand that x and ϑ do not describe the deflection introduced at the mirror, but the deflection of the waist of the beam to the initial position of the waist. Therefore, z describes the distance from the waist to the detector, not from the deflected mirror to the detector.

However, one can adjust the formula to a scenario where the beam is not deflected at the waist. Assuming that the beam is deflected by θ at the mirror. Then, at the waist, the beam still has deflection θ. However, the waist is also spatially deflected by $L_f\theta$, where L_f is the distance from the mirror to the waist as seen in Fig. 3.12. Assuming that the distance from the mirror to the detector is L we can substitute Eq. 3.47,

$$\begin{aligned}
\delta R &= (x + z\theta)\,\mathrm{Re}[(\sigma_z)_w] + (\frac{z}{z_R}x - z_R\theta)\,\mathrm{Im}[(\sigma_z)_w] \\
&= (L_f\theta + (L - L_f)\theta)\,\mathrm{Re}[(\sigma_z)_w] + (\frac{L - L_f}{z_R}L_f\theta - z_R\theta)\,\mathrm{Im}[(\sigma_z)_w] \\
&= \Big[L\,\mathrm{Re}[(\sigma_z)_w] + (\frac{(L - L_f)L_f}{z_R} - z_R)\,\mathrm{Im}[(\sigma_z)_w]\Big]\theta\,, \qquad (3.56)
\end{aligned}$$

which is the pointer shift at the detector.

The postselection probability for the entangled system of Section 3.2 is calculated to be

$$P_{\mathrm{ps}} = \frac{1}{2}[1 + 2\sin\alpha\cos\alpha\gamma\cos\varphi]\,. \qquad (3.57)$$

Putting these two parameters into Eq. 3.50 we arrive at

$$\begin{aligned}\mathcal{SNR}_{\text{wva}} &= \sqrt{\frac{8}{\pi}}\frac{\sqrt{NP_{\text{ps}}}\delta R}{w(z)} \\ &= \sqrt{\frac{8}{\pi}}\frac{\sqrt{NP_{\text{ps}}}\Big[L\,\text{Re}[(\sigma_z)_w] + (\frac{(L-L_f)L_f}{z_R} - z_R)\,\text{Im}[(\sigma_z)_w]\Big]\theta}{w(L-L_f)}\,.\end{aligned} \tag{3.58}$$

It can be shown numerically that $\mathcal{SNR}_{\text{wva}} \leq \mathcal{SNR}_{\text{lens}}$ for some fixed parameters. For this, realistic values to the beam parameters w_0 and λ and to the deflection θ are assigned:

$$\begin{aligned} N = 1000\,,\ w_0 = 800\,\mu\text{m}\,,\ \lambda = 810\,\text{nm}\,, \\ z_R = \frac{\pi w_0^2}{\lambda} = 2.4823\,\text{m} \ \text{ and } \ L_f = 0.45\,\text{m}\,. \end{aligned} \tag{3.59}$$

The deflection corresponds to a beam overlap of $\gamma = 99.9\%$ and a divergence angle of $\theta_{\text{div}} = 322\,\mu\text{rad}$.

Using Mathematica it is straight forward to maximize the function $\mathcal{SNR}_{\text{wva}}(\alpha, \varphi, \theta, L_f)$ of Eq. 3.58 numerically for a certain domain: $0 < \alpha < \frac{\pi}{2}$, $0 < \varphi < 2\pi$, $0 < \theta < 10\,\mu\text{rad}$ and $L_f < L < 5\,\text{m}$. The maximal value of the function in this range is

$$\max\Big(\mathcal{SNR}_{\text{wva}}(\alpha, \varphi, L, \theta)\Big) = 1.54384\,. \tag{3.60}$$

for the values

$$\alpha = 0.620209\,, \quad \varphi = 3.02789\,, \quad L = 5\,\text{m} \quad \text{and} \quad \theta = 10\,\mu\text{rad}\,. \tag{3.61}$$

Here, it is important to note that L_f should not be chosen to be great, because otherwise this method also incorporates the far-field method. In this scenario the two methods would therefore not be comparable. It can be seen that the function is maximized for the bound of L. This is surprising at first glance, since the beam intensity is distributed over a larger beam diameter with increased distance and therefore the signal should be lost in the noise at a certain distance. However, from a theoretical point of view both the deflection d and the waist of the beam w_0 in Eq. 3.49 grow linearly with increasing distance of the detector, which results in the signal-to-noise ratio approaching a constant. Therefore, the theoretical optimal value for L might be found beyond 5 m, even though in experimental realization it might approach zero with increasing distance.

It is also not surprising that the signal-to-noise ratio gets better for larger θ. However, only in regions of weak interactions, that is where θ is small the effect of weak value amplification occurs.

Calculating the signal-to-noise-ratio for the lens with the obtained parameter for θ yields

$$\mathcal{SNR}_{\text{lens}} = 1.56576\,. \tag{3.62}$$

Clearly, this is higher than the maximal value the signal-to-noise ratio of the weak value amplification method. Consequently, the signal-to-noise ratio of the far field measurement and the lens measurement is better than the weak value amplification.

In Fig. 3.13 the signal-to-noise ratio for the weak value amplification method and the lens method are shown, dependent on the deflection θ. For the weak value amplification the optimal parameters for α, L and the phase φ obtained by the maximization are used. Clearly, for small deflections θ the signal-to-noise ratio of the weak value method is comparable to the signal-to-noise ratio of the lens method. Yet, for larger θ the SNR of the weak value amplification method becomes smaller. Here, the weak value amplification effect vanishes, as the deflection is not a weak interaction anymore.

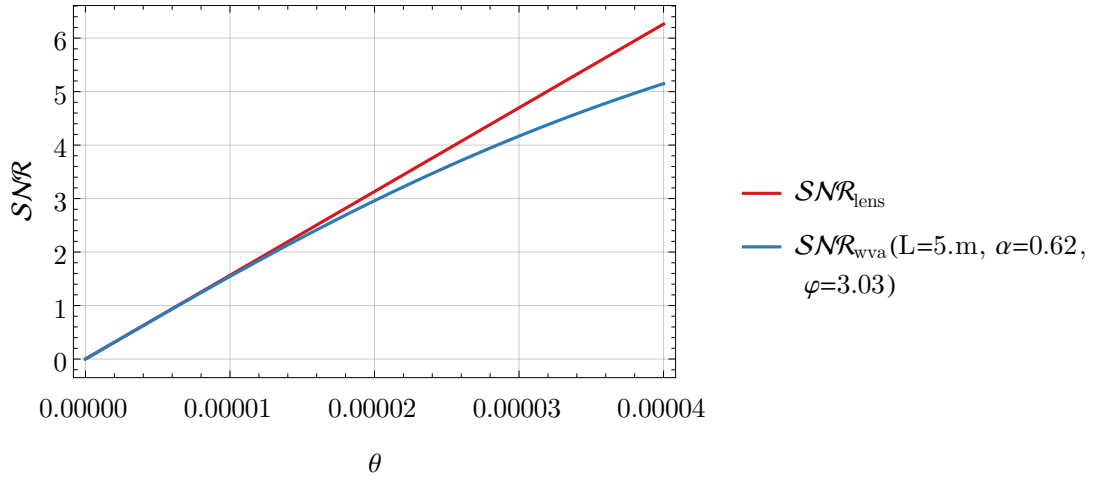

Figure 3.13.: SNR dependent on the deflection θ for the lens method and the weak value amplification method. As parameters $L_f = 0.45\,\text{m}$, $w_0 = 800\,\mu\text{m}$, $\lambda = 810\,\text{nm}$ and $\theta = 5\,\mu\text{rad}$ are chosen as realistic laboratory values. The best α, L and phase φ are chosen for the weak value amplification plot. $\mathcal{SNR}_{\text{wva}}$ remains comparable to $\mathcal{SNR}_{\text{lens}}$ for small deflections, but becomes smaller for larger deflections. Here, the weak value amplification effect vanishes.

In Fig. 3.14 the signal-to-noise ratio of a lens and of the weak value method is shown. In principle the pointer shift can have negative sign, but because the SNR is greater than zero the absolute value of the pointer shift is used for the calculation. As parameters $L_f = 0.45\,\text{m}$, $w_0 = 800\,\mu\text{m}$, $\lambda = 810\,\text{nm}$ and $\theta = 5\,\mu\text{rad}$ are chosen. For the different detector positions L the optimal α is calculated and

used. One can see that the weak value amplification method performs differently for several positions L, the SNR however never exceeds the SNR of the lens.

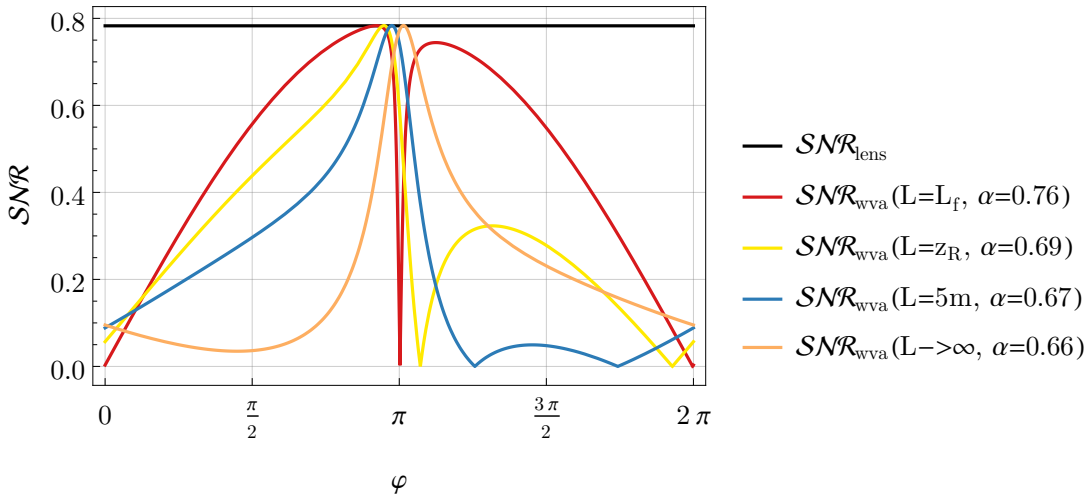

Figure 3.14.: SNR dependent on the phase φ. The curves show the SNR for different detector positions L. As parameters $L_f = 0.45\,\mathrm{m}$, $w_0 = 800\,\mu\mathrm{m}$, $\lambda = 810\,\mathrm{nm}$ and $\theta = 5\,\mu\mathrm{rad}$ are chosen as realistic laboratory values. The best α for each detector positions is L calculated. $\mathcal{SNR}_{\mathrm{wva}}$ remains smaller than $\mathcal{SNR}_{\mathrm{lens}}$ for the L that are considered.

Apparently, the SNR differs for different positions L of the detector. In Fig. 3.15 the SNR is shown for a lens and for the weak value method with several phases φ. For each φ the best α is calculated. For the blue line both α and φ are optimized, which yields a phase of close to π. The other parameters are the same as for Fig. 3.14. The SNR of the weak value amplification method never exceeds the SNR of the lens.

3.3.3. Technical noises

We have seen that the signal-to-noise ratio of the weak value amplified beam deflection measurement is never better than amplifying the deflection with a lens or measuring it in the far field. Yet, weak value amplification has an advantage compared to the other two methods: technical noise of the optical components can be suppressed.

Technical noise is introduced by the technical components of a measurement device. It is for example a limited detector resolution or noise caused by random jiggling of the components from temperature changes or air fluctuations.

The weak value method is now compared with regard to technical noise with the two alternative methods discussed in the above section. The analysis follows the one of [48]. In this section the technical noise is modeled as additional shifts on

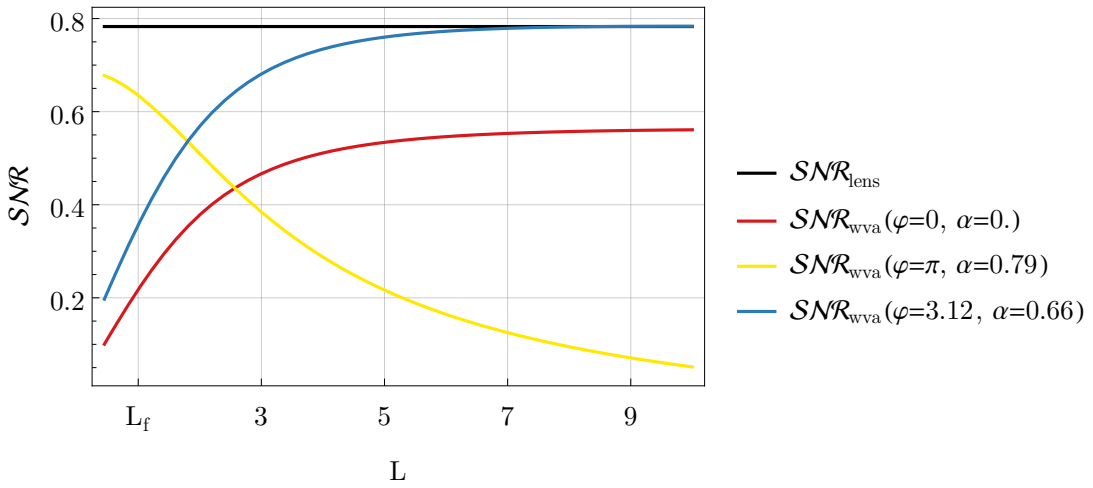

Figure 3.15.: SNR dependent on L. The curve show the SNR for several phases φ. As parameters $L_f = 0.45\,\mathrm{m}$, $w_0 = 800\,\mu\mathrm{m}$, $\lambda = 810\,\mathrm{nm}$ and $\theta = 5\,\mu\mathrm{rad}$ are chosen as realistic laboratory values. α is optimized for each phase. $\mathcal{SNR}_{\mathrm{wva}}$ remains smaller than $\mathcal{SNR}_{\mathrm{lens}}$ for the L that are considered, even when both α and φ are optimized (blue line).

the detector introduced by the components of the measurement system. However in a realistic laboratory environment a modulation introduced by the detector would rather correspond to, for example, a limited detector resolution due to a certain pixel size. This shift shall be denoted with δx_i, where i is a placeholder for the different shifts observed.

The goal is to measure the shift introduced by a beam displacement θ, δx_θ. Any other δx_i is technical noise introduced by the components of the measurement setup.

Far field measurement For the far-field measurement only the detector can introduce an additional shift. Any translation $d' = \delta x_d$ of the detector, as shown in Fig. 3.16, influences the detected shift. The ratio of the shifts δx_θ and δd_d is

$$\mathcal{R}_{\mathrm{farfield}} = \frac{\delta x_\theta}{\delta x_d} = \frac{L\theta}{d'}\,. \tag{3.63}$$

We see that the deflection θ can only be detected when either δx_d is small or the deflection is big. Using a laser beam with a small waist and introducing only a small deflection, the detector modulation might already make it impossible to detect the signal. The modulations are less significant if a beam with a larger waist is used.

Lens measurement In the measurement setup with the lens several modulations can affect the signal $\delta x_\theta = f\theta$. Detector modulations impact the signal the same

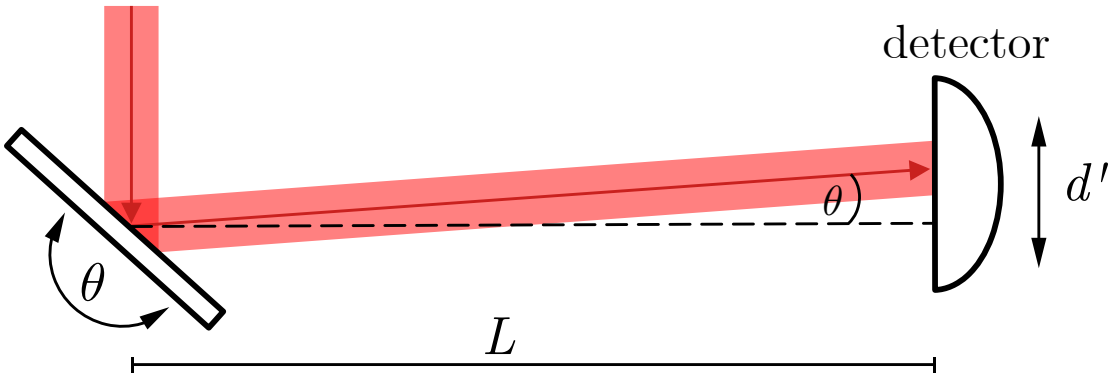

Figure 3.16.: A beam is deflected by an angle θ, which is detected at the far field at distance L. The detector introduces a noise $\delta x_d = d'$.

way as in the far field measurement, $\delta x_d = d'$. In addition the lens can be tilted, introducing a shift $\delta x_q = f\theta_q$, as shown in Fig. 3.17. The ratio between the shift we want to detect and the shift due to the noise is given by

$$\mathcal{R}^d_{\text{lens}} = \frac{\delta x_\theta}{\delta x_d} = \frac{f\theta}{d'} \tag{3.64}$$

$$\mathcal{R}^q_{\text{lens}} = \frac{\delta x_\theta}{\delta x_q} = \frac{f\theta}{f\theta_q} = \frac{\theta}{\theta_q}\,. \tag{3.65}$$

In this measurement the beam waist at the detector is small, as the detector is placed at the focus of the lens. Hence, detector modulations might be of the same order as as the signal we want to measure. The method does not suppress technical noise.

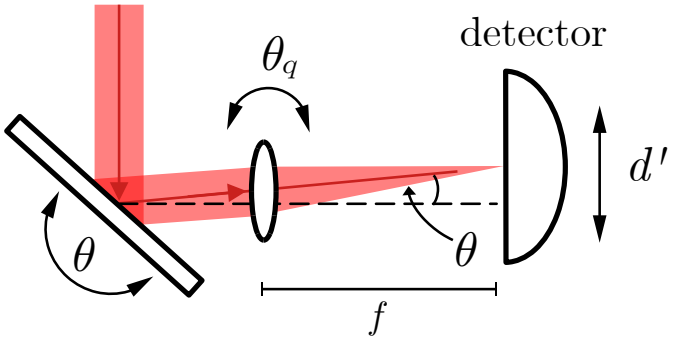

Figure 3.17.: A beam is deflect by an angle θ, which is amplified using a lens with focal length f. The detector introduces a noise $\delta x_d = d'$ and the lens a noise $\delta x_q = f\theta_q$.

Weak value amplification This result is different for the weak value amplification method. For a more general scenario assume the signal to be measured

is given by $\delta x_\theta = dA_w$ whereas the detector signal is given by $\delta x_d = d'$. The technical noise ratio is therefore

$$\mathcal{R}^d_{\text{wva}} = \frac{\delta x_\theta}{\delta x_d} = \frac{dA_w}{d'} \,. \tag{3.66}$$

In this equation the deflection at the detector scales with the weak value A_w. Therefore, for a large weak value, the signal scales better than the detector modulation, outperforming the lens or far field measurement, where the detector jiggling and the signal are of the same order of magnitude.

For the experiment of this thesis the signal we want to measure is given by $\delta x_\theta = \Big[L\,\mathrm{Re}[(\sigma_z)_w] + (\frac{(L-L_f)L_f}{z_R} - z_R)\,\mathrm{Im}[(\sigma_z)_w]\Big]\theta$. Calculating the ratio we arrive at

$$\mathcal{R}^d_{\text{wva}} = \frac{\delta x_\theta}{\delta x_d} = \frac{\Big[L\,\mathrm{Re}[(\sigma_z)_w] + (\frac{(L-L_f)L_f}{z_R} - z_R)\,\mathrm{Im}[(\sigma_z)_w]\Big]\theta}{d'} \,. \tag{3.67}$$

In Fig. 3.18 the ratios $\mathcal{R}^d_{\text{lens}}$ and $\mathcal{R}^d_{\text{wva}}$ are depicted in dependence of the phase φ. For the lens a focal length of $f = 0.5\,\text{m}$ is chosen. A big detector modulation of $100\,\mu\text{m}$ is assumed. The deflection of the beam is assumed to be $\theta = 50\,\mu\text{rad}$, which corresponds to a beam overlap of $\gamma = 95\%$. The waist of the beam is placed at $L_f = 0.5\,\text{m}$. For the beam the parameters $w_0 = 800\,\mu\text{m}$ and $\lambda = 810\,\text{nm}$ are chosen again, and for the parameter adjusting the beam amplitudes $\alpha = 44°$.

For those values $\mathcal{R}^d_{\text{lens}} = 0.25$, which is shown as a black line in Fig. 3.18. The beam overlap of $\gamma = 95\%$ is far from ideal, decreasing the visibility and hence also decreasing the weak value. Still, for almost all φ the ratio $\mathcal{R}^d_{\text{wva}} > \mathcal{R}^d_{\text{lens}}$, sometimes even almost 16 times larger. This means that the weak value amplification method suppresses technical noise of the detector very well.

In fact, the method is able to suppress all technical noise that appears *behind* the interferometer. This is easy to see when assuming that d' is not only the detector modulation but some shift introduced by other components. These might for example be a beam splitter which separates the beam behind the interferometer output so that two detectors, one in the near field and one in the far field, can be used. In this case Eq. 3.67 still holds. The modulations are small compared to a displacement amplified by a large weak value.

The calculation for technical noise introduced by components *inside* the interferometer is not as straight forward. These modulations could for example stem from a shaky mirror or from the Dove prism being misaligned, introducing a momentum kick into a beam that enters the Dove prism on the heights of its axis.

All those modulations are weak value amplified. This is because the two beams in the interferometer are spatially separated from each other. A small modulation in one arm will not influence the other arm, hence the weak value amplification works. A possible modulations is displayed in Fig. 3.19. Here, the Dove prism is misplaced and introduces a additional angle θ_q.

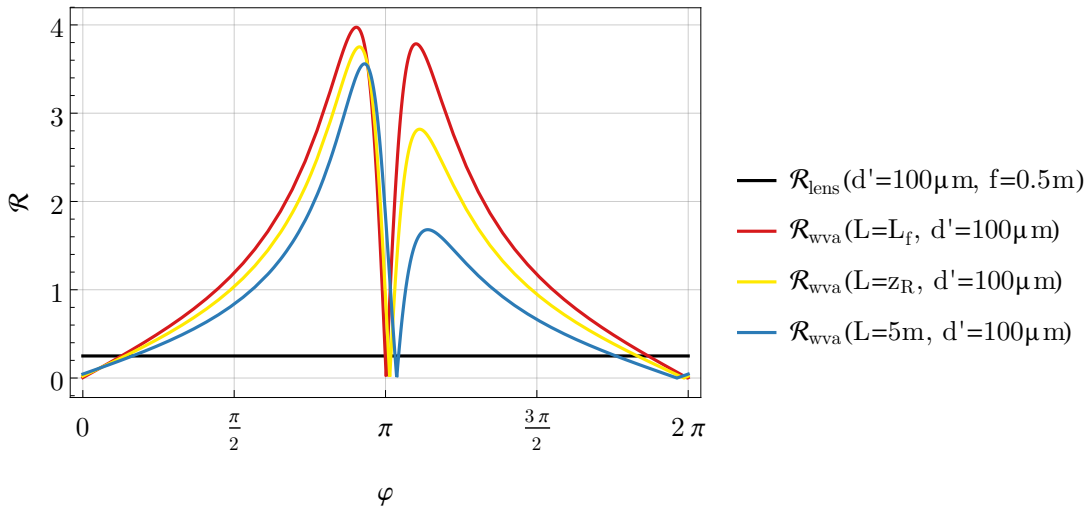

Figure 3.18.: The ratio of signal to noise introduced by detector modulations dependent on the phase φ for different L. As parameters $\theta = 50\,\mu\text{rad}$, $L_f = 0.5\,\text{m}$, $f = 0.5\,\text{m}$, $\alpha = 44°$, $w_0 = 800\,\mu\text{m}$, $\lambda = 810\,\text{nm}$ and a detection modulation of $d' = 100\,\mu\text{m}$ are chosen. For almost all φ the the weak value amplification method performs much better than the lens method, leading to stark suppression of technical noise.

The modulation which stems from a misplaced Dove prism can be calculated with an interaction

$$\hat{U} = \hat{P}_A \otimes e^{-i\varepsilon_x \hat{q}} + \hat{P}_B \otimes \mathbb{1} \tag{3.68}$$

acting on a initial state $|\psi\rangle \otimes |\Phi_0\rangle$. Here, the Dove prism introduces a momentum kick q into one arm and leaves the other arm unaffected (because it is only placed in one arm). As before is useful to express the distance with respect to L: The dove prism is placed at a position $0 < L_D < L_f < L$, and the distance from the Dove prism to the waist is expressed as $L_f - L_D$. Then the pointer shift can be calculated to be

$$\delta x_q = \Big((L - L_D)\,\text{Re}[(\hat{P}_A)_w] + (\frac{(L - L_f)(L_f - L_D)}{z_R} - z_R)\,\text{Im}[(\hat{P}_A)_w]\Big)\theta_q\,. \tag{3.69}$$

We see that the modulation θ_q is indeed weak value amplified. The ratio between the modulation δx_θ and δx_q is

$$\mathcal{R}^q_{\text{wva}} = \frac{\delta x_\theta}{\delta x_q} = \frac{\Big(L\,\text{Re}[(\sigma_z)_w] + (\frac{(L-L_f)L_f}{z_R} - z_R)\,\text{Im}[(\sigma_z)_w]\Big)\theta}{\Big((L - L_D)\,\text{Re}[(\hat{P}_A)_w] + (\frac{(L-L_f)(L_f-L_D)}{z_R} - z_R)\,\text{Im}[(\hat{P}_A)_w]\Big)\theta_q}\,. \tag{3.70}$$

The nominator and the denominator are of the same order. However, this ratio is higher than $\mathcal{R}^q_{\text{lens}}$ for certain ranges, so that the weak value amplification still

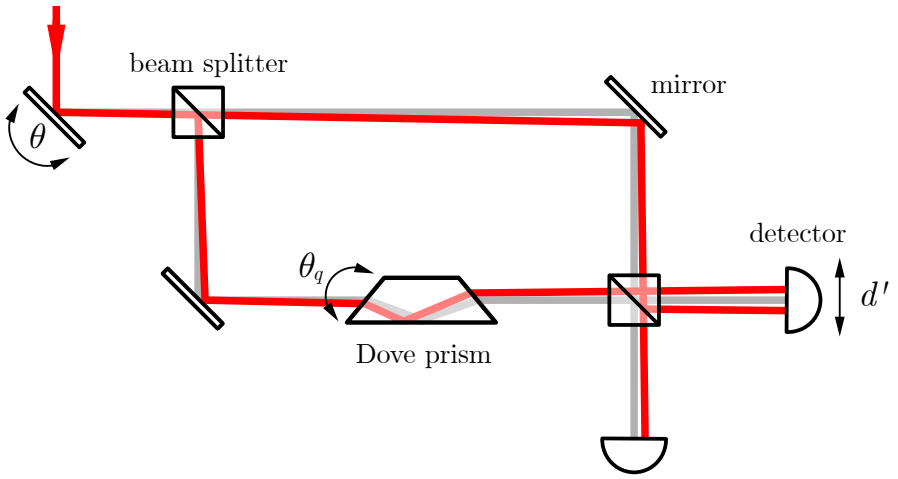

Figure 3.19.: A beam is deflect by an angle θ, which is amplified using a interferometric weak value amplification setup. The detector introduces a noise $\delta x_d = d'$ and the Dove prism a noise $\delta x_q \propto \theta_q$.

performs better than a measurement with a lens. In Fig. 3.20 the noise ratios for a lens respectively Dove prism modulation of $\theta_q = 100\,\mu\text{m}$ is shown. $\theta = 50\,\mu\text{m}$ is chosen as the deflection to be measured, together with $\alpha = 44°$, $w_0 = 800\,\mu\text{m}$, $\lambda = 810\,\text{nm}$. The Dove prism is placed $L_D = 0.4\,\text{m}$ and the waist $L_f = 0.5\,\text{m}$ behind the mirror. Evidently, for some φ the weak value method performs better than the measurement with the lens. Sometimes the ratio is even larger than 1. However, in contrast to the modulations behind the interferometer, the weak value amplification method does not perform much better.

For other modulations inside of the interferometer one arrives at the same conclusion, as modulation Eq. 3.68 can model any other modulation inside the interferometer.

3.3.4. Further comments on the methods

As we have seen, the signal-to-noise ratio of the weak value amplification method is at best as good as the one of a magnifying lens or of a far field measurement. On the other hand, it is possible to strongly suppress technical noise of components behind the interferometer, which is not possible with the other methods. Thus, since technical noise is part of any experimental setup, weak value amplification has the potential to outperform the other methods.

Some more aspects of the weak value method are worth mentioning: It would allow to employ detectors with larger pixel size. This follows from Eq. 3.65 and Eq. 3.67 for the detector modulations: d' could also be the pixel size. If it is larger than the shift introduced by the lens, the shift remains unobservable, as it would not go beyond the pixel width. The amplified shift of the weak value amplification

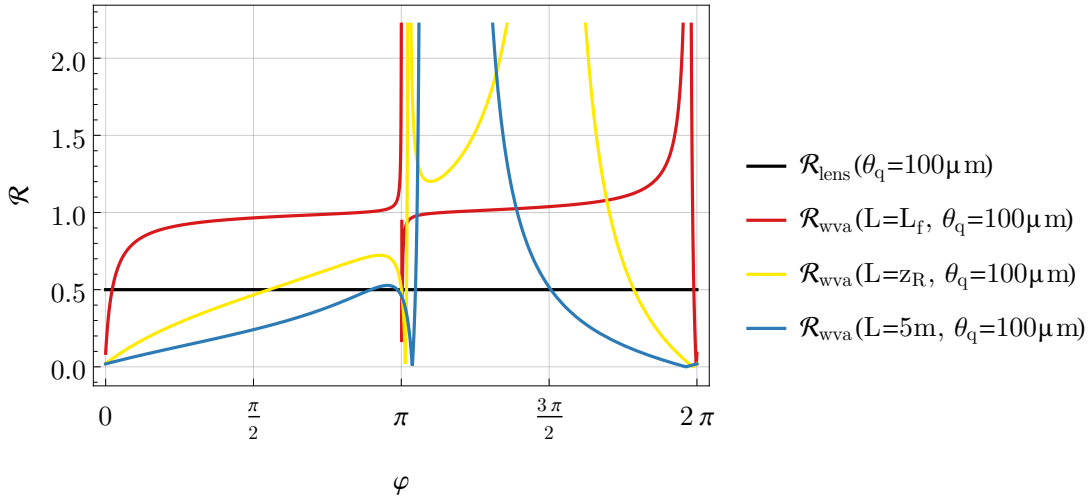

Figure 3.20.: The ratio of signal to noise introduced by the lens and the Dove prism modulations dependent on the phase φ for different L. As parameters $\theta = 50\,\mu\text{rad}$, $\alpha = 44°$, $w_0 = 800\,\mu\text{m}$, $\lambda = 810\,\text{nm}$ and a lens respectively Dove prism modulation of $\theta_q = 100\,\mu\text{rad}$ are chosen. The Dove prism is placed $L_D = 0.4\,\text{m}$ and the waist $L_f = 0.5\,\text{m}$ behind the mirror. For some φ the weak value method performs better than the measurement with the lens, however not much better.

method could, in contrast, go beyond the pixel width and would be detected on the neighboring pixel. Having a detector with a bad resolution would affect the precision of both methods, but the weak value amplification method would suffer less.

Weak value amplification is also more suitable to handle a highly sensitive detector, which saturates at low intensities. The lens is used with an intensity just before the detector saturates. Decreasing the intensity would then decrease the precision of the measurement with the lens. Here lies another merit of weak value amplification: As the amplification effect occurs in low intensities due to the postselection, the detector does not saturate, and the precision is not affected by reducing the intensity. If the detector saturates at intensity N of Eq. 3.49, the weak value method allows to increase the intensity by a factor $1/P_{\text{ps}}$ until the detector saturates, with P_{ps} being the postselection probability. This increases the signal-to-noise ratio by a factor $1/\sqrt{P_{\text{ps}}}$

Another aspect is that the weak value amplification method allows the detection of both position shifts and angular deflections in one measurement. This is because the shift at the detector, wherever it is placed, contains amplification of both deflections. With the two alternative methods this is more challenging because the detector has to be placed at different positions for the position shift detection and the momentum shift detection. In general, it could be implemented by splitting the beam behind the displacement or the lens, and putting up two

screens. However, this would very likely introduce new technical noise, decreasing the precision.

Using two detectors is likewise possible in the weak value amplification method, with the difference that additional noise introduced by, for example, a beam splitter behind the interferometer is suppressed. If one detector is placed in the near field and the other in the far field, two sets of data can be obtained simultaneously for one deflection measurement. With the distance between both detectors, the position of the beam waist can be extracted from the data with a fit. This is another merit of the weak value amplification method.

In addition, a related experiment should be mentioned. In [53] angular beam displacements were measured precisely by evaluating the fringe pattern at the output of an interferometer. Interestingly, the interferometer was very small, consisting of only a polarizing cube beam splitter, a right-angle prism and a cube corner reflector. With this sensor, angular deflections of up to 1 µrad were observed. This experiment demonstrates that, in principle, our weak value amplification measurement device could be compressed to a much smaller setup, combining the advantages of the compact lens method with the merits of weak value amplification. It would also be interesting to demonstrate if postselecting would enhance the precision of the sensor used in [53].

In conclusion, none of the presented methods always outperforms the other methods. Using a lens to magnify the deflection is a compact setup with a signal-to-noise ratio as good as detecting the beam in the far field. However, detector jitter cannot be suppressed. The weak value amplification method has a signal-to-noise ratio performing often worse than the one of the measurement with the lens. Conversely, however, this means that the method can become just as good as the lens while technical noise behind the interferometer is strongly suppressed. Additionally, the position of the beam waist can be determined using two detectors. The setup presented here is a rather large prototype with many optical components, but it could possibly be compressed when using an interferometer as [53]. Then, the susceptibility to noise could be reduced even further, resulting in a precise measurement device.

4. Experiment

This chapter explains the experimental realization in detail. Instead of a Mach-Zehner interferometer, we have chosen an Sagnac-like interferometer since a Sagnac-like interferometer is constructed such that the two arms of the interferometer use the same optical components, which increases its stability.

As explained in Chapter 3, the interferometer is also implemented in polarization space. Hence, the interferometer and the postselection were set up in polarization space, which made the alignment more difficult. In this chapter we will discuss difficulties we encountered and how we were able to overcome several of them. For the remaining ones we propose solutions.

Finally, we devise an algorithm to fit the theoretical model derived in Chapter 3 to empirical data. We present preliminary laboratory data of a deflection measurement relative to the Dove prisms and discuss the results.

4.1. Optical components

The behavior of the optical components in the experimental setup are essential for the experiment. As mentioned in Chapter 2 light has several polarization states, visualized as qubit states on the Bloch sphere. In the so-called "Jones calculus" [54] optical components are represented using matrices. Acting of those matrices on the qubit states will result in a new qubit state, representing the change light undergoes when passing optical components [11].

4.1.1. Linear polarizer

A linear polarizer is an optical component that blocks light of a certain linear polarization, while it lets light of other polarizations pass through. This way, unpolarized light is transformed into light with a well-defined polarization, or light of a certain polarization can be transformed to another polarization [11, 13].

The matrix for a general polarizer with the transmission axis tilted by an angle of θ to the horizontal axis of light is written as [13]:

$$P(\theta) = \begin{bmatrix} \cos^2\theta & \cos\theta\sin\theta \\ \cos\theta\sin\theta & \sin^2\theta \end{bmatrix} . \tag{4.1}$$

Here we see that if $\theta = 0°$ then $P = |H\rangle\langle H|$, thus the polarizer only selects horizontally polarized light. It acts as a projector on one specific vector, the $|H\rangle$-

state. Vice versa, for $\theta = 90°$ the polarizer only transmits vertical light, becoming an projector on the $|V\rangle$-state. For $\theta = \pm 45°$ the polarizer selects light with $|P\rangle$, respectively $|M\rangle$-polarization.

The linear polarizer does not change the polarization of circular polarized light. This becomes evident when the matrix acts on one of the two circular polarization states, e.g. $|R\rangle$. The resulting state is a state

$$P(\theta)\,|R\rangle = \frac{1}{\sqrt{2}} \begin{bmatrix} \cos^2\theta + i\cos\theta\sin\theta \\ \cos\theta\sin\theta + i\sin^2\theta \end{bmatrix} . \tag{4.2}$$

Taking a look at the intensity of this state, $I \propto |P(\theta)\,|R\rangle\,|^2 = \frac{1}{2} = 1|\,|R\rangle\,|^2$ we see that it remains constant: It is half of the initial amplitude.

Malus's law for linear polarizers [10, 11] explains this result. It states that a polarizer placed into polarized light with angle θ to the initial polarization direction of the light transmits $I_0 \cos^2\theta$ of the initial intensity of the light. Since circular polarized light changes the polarization direction over one period, describing a circle, the angle θ changes. The intensity is then just calculated with the average value of $\cos^2\theta$, which is $\frac{1}{2}$.

For elliptical light however, the intensity fluctuates. Over one period the electrical field vector changes its length, describing an ellipse. Hence, for different angles different fractions of horizontal and vertical light is transmitted, resulting in an intensity modulation.

4.1.2. Half-wave plate

A wave plate alters the polarization of light that travels through it [11]. Wave plates have two axes, with different refractive indices. Light on one axis therefore travels faster than the light on the other axis, resulting in a phase shift between the two components of light. The axis with lower refractive index, that is, where the light travels faster, is called the "fast axis" [13].

A half-wave plate (HWP) rotates the linear polarization of light along some angle. The matrix for a general half-wave plate with the fast axis tilted by an angle θ to the horizontal axis of light is [13]:

$$H(\theta) = \begin{bmatrix} \cos(2\theta) & \sin(2\theta) \\ \sin(2\theta) & -\cos(2\theta) \end{bmatrix} . \tag{4.3}$$

We see that for $\theta = 0°$ it leaves horizontal light unaffected and it introduces a global phase of π to vertical light. It changes plus polarization to minus polarization and vice versa. For $\theta = 45°$ horizontal light is rotated to vertical light and vertical to horizontal. Plus stays plus and minus gets a global phase of π. For both angles right handed light changes to left handed light and vice versa, with the light obtaining additional phases for $\theta = 0°$.

4.1.3. Quarter-wave plate

A quarter-wave plate (QWP) changes linear polarized light to elliptical polarization and elliptical polarized light to linear polarization [11]. Its matrix is [13]:

$$Q(\theta) = \begin{bmatrix} \cos^2\theta - i\sin^2\theta & (1+i)\sin\theta\cos\theta \\ (1+i)\sin\theta\cos\theta & \sin^2\theta - i\cos^2\theta \end{bmatrix} \tag{4.4}$$

where θ again denotes the angle of the fast axis to the horizontal axis of light.

For $\theta = 45°$ the quarter-wave plate changes horizontal light to right handed light and vertical light to left handed light. Plus polarization remains unchanged, minus acquires an additional global phase of $-\pi/2$. Right handed light is changed to vertical light and left handed light to horizontal light.

For an arbitrary linear polarization the action of the quarter-wave plate is as follows

$$\begin{aligned} Q(45°)[\cos\alpha\,|H\rangle + \sin\alpha\,|V\rangle] &= \frac{1}{\sqrt{2}}\Big[\cos\alpha\exp\Big(-i\frac{\pi}{4}\Big)\,|R\rangle + \sin\alpha\exp\Big(i\frac{\pi}{4}\Big)\,|L\rangle\Big] \\ &\simeq \frac{1}{\sqrt{2}}\Big[e^{i\alpha}\,|H\rangle + ie^{-i\alpha}\,|V\rangle\Big], \end{aligned} \tag{4.5}$$

omitting the global phase, which is elliptically polarized light.

4.2. Interferometric setup

This section describes the the fundamental idea of the experimental setup. We motivate our choice of a Sagnac-like configuration over a Mach-Zehnder interferometer and give the technical specifications of the setup.

4.2.1. Sagnac-like configuration

For the experiment we have chosen a Sagnac-like interferometer. In a Sagnac interferometer [55] a beam splitter splits a single beam into two beams. They then travel in opposite directions through the interferometer, hitting the same three mirrors until they reach the beam splitter again. Usually, in a Sagnac interferometer both beams travel along exactly the same path and thus hit every component at the same place [11].

This has two advantages over a Mach-Zehnder interferometer, which was used for the theoretical calculations. Firstly, a Sagnac-like configuration is easier to align. In usual Sagnac setups the two beams overlap and therefore have the exact same path length. The different phase between the two beams can, for example, be introduced by rotating the whole interferometer [55, 56]. For our experiment we need to spatially separate the arms of the interferometer to be able to insert Dove prisms in both of the arms. Separation of the beams can be achieved by moving the

first or third mirror so that the position on the beam splitter for the incoming and outgoing beam is no longer identical. The beams still hit the same components on spots close to each other. Fluctuations and irregularities on the components, like expansions of components, will therefore affect both beams, making a Sagnac-like interferometer easier to align than a Mach-Zehnder interferometer.

Furthermore, this configuration is rather stable against phase fluctuations because fluctuations change the path length of both arms, and therefore they do not introduce phase changes. In a similar setup to the one presented in this thesis, Dziewior et al. [8] used a Mach-Zehnder interferometer to measure small beam displacements. In it, even small fluctuations of the mirror changed the path length in only one arm and thus changed the phase, which was not wanted. To overcome this obstacle, Dziewior et al. had to obtain data over a full period of the phase. They were able to eliminate the phase fluctuations by post-processing the data. Another method, even more cumbersome, would be to stabilize the phase fluctuations.

In order to deliberately change the phase in the interferometer, as we want to do it, one could, for example, place and rotate a thin glass plate in one of the arms. In our experiment we introduce a phase behind the interferometer by projecting on certain polarizations, which is described in the following section.

4.2.2. Plan for experimental setup

These considerations motivate the fundamental idea for the experimental setup. The first steps of implementing the setup are described in detail in Zerweck's Bachelor thesis [57]. Fig 4.1 shows the plan with all the components to be explained in this section (with the labels used in the figure in brackets). The setup was implemented this way initially. However, several components had to be altered when they showed erroneous behavior. All alterations are explained in the following sections.

In the experiment a laser with wavelength 810 nm is used. A photodiode is placed on a laser stage in front of the experiment to serve as a reference to subtract laser fluctuations. It is therefore called reference diode. The light for the experiment itself is coupled into a fiber. The collimator, where the beam enters the experiment, is set so that the emergent Gaussian beam is collimated, i.e. that it has the minimal beam divergence.

A half-wave plate (HWP 1) is placed after the collimator to rotate the polarization to maximize the output intensity. Moreover, two mirrors are placed behind the collimator. They change the propagation direction of the beam so that the available space on the optical table can be used optimally. Both will introduce the weak spatial and angular deflection we want to measure when the whole experiment is set up. While setting up the interferometer, they are placed so that the beam travel parallel to a row of holes on the optical table.

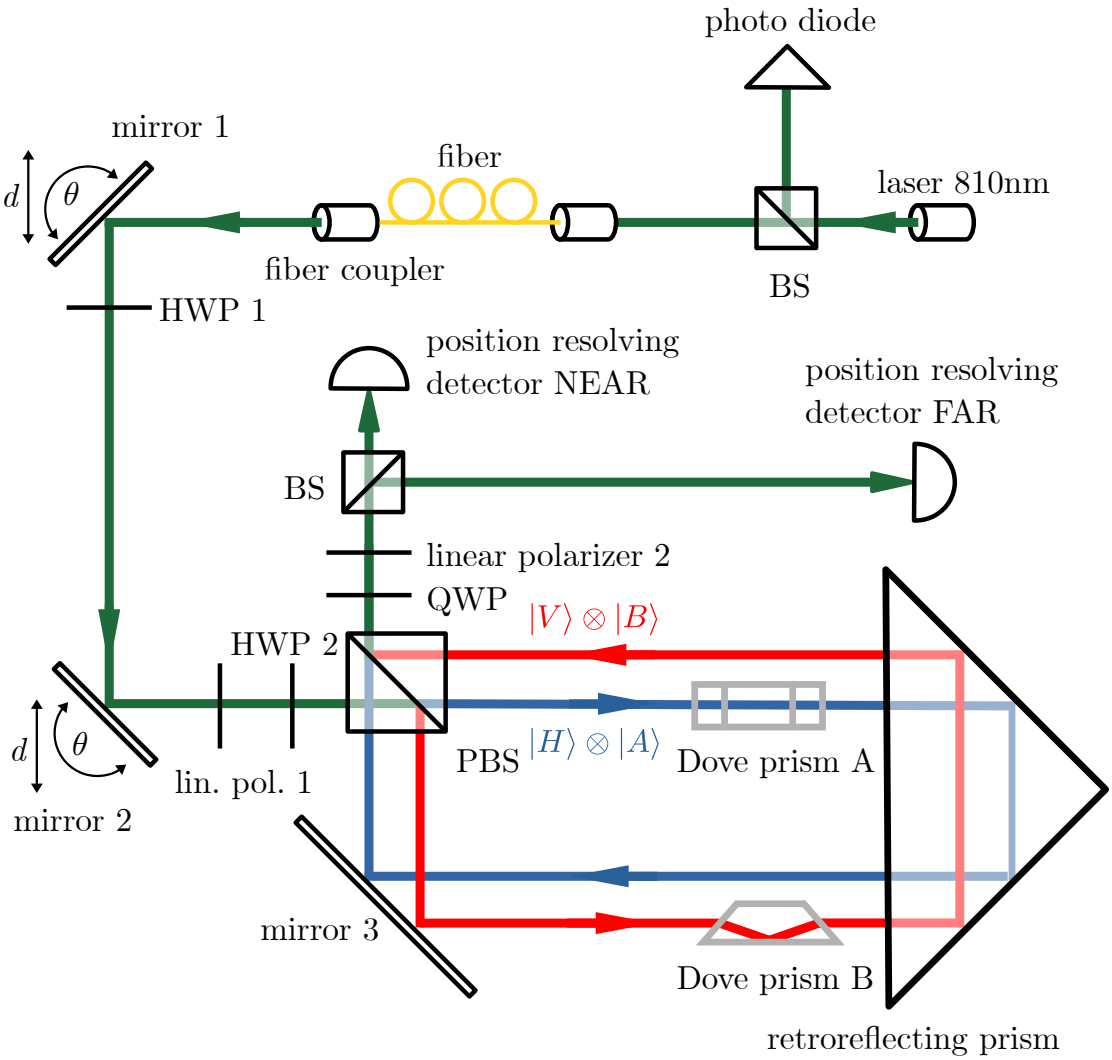

Figure 4.1.: The originally planned experimental setup with all components.

A polarizer (linear polarizer 1) behind the second mirror polarizes the beam. We chose vertical polarization. Behind it, a variable half-wave plate (HWP 1) is placed. Together with a polarizing beam splitter (PBS) right behind it, it sets the amplitudes of the two resulting beams: In the polarizing beam splitter the horizontal component of light is transmitted (the resulting arm is labeled "A"), while the vertical component is reflected (the resulting arm is labeled "B"). With the half-wave plate the ratio of horizontal polarization versus vertical polarization is adjusted, and therefore the amplitudes of the resulting polarized beams in the interferometer are set. The state of the interferometer is described by

$$|\psi\rangle = \cos\alpha\,|H\rangle \otimes |A\rangle + \sin\alpha\,|V\rangle \otimes |B\rangle\ , \qquad \text{(3.13 revisited)}$$

with the polarization degree of freedom and the path degree of freedom. Note that using a polarizing beam splitter has the effect that the interferometer effectively has only one output port. When the beams enter the polarizing beam splitter again, the horizontal beam enters from below (in the bird's eye perspective in Fig. 4.1) and is transmitted, while the vertical beam enters from the right and is reflected by 90°, hence leaving the interferometer at the same output than the horizontal beam. The outer port remains dark (except for imperfections).

We use a a retroreflecting prism instead of two mirrors to facilitate setting up and aligning the interferometer. Two reflecting surfaces are attached with a 90° angle, such that a beam will be reflected back parallel to the incident direction. A third mirror (mirror 3) is then set up so that it separates the beams inside the interferometer. A large separation is obtained using a 2 inch mirror. Slight tilts of the mirror can introduce misalignment to the interferometer.

After the polarizing beam splitter the two beams overlap again, forming the state of Eq. 3.13. They do not have any phase difference, and they do not interfere, as they have opposite polarization. Tracing out the polarization degree of freedom demonstrates this: The result is a mixed state $\cos^2\alpha\,|A\rangle\langle A| + \sin^2|B\rangle\langle B|$. Projecting on an output and calculating the intensity at the output, as in Eq. 3.4 results in $I = 1$. The intensity is not dependent on a phase between the two beams; therefore the beams do not interfere.

To see an interference, it is necessary to project on a polarization. This is done by placing a quarter-wave plate (QWP) and a linear polarizer (linear polarizer 2) behind the polarizing beam splitter. If the optical axis of the quarter-wave plate is set with an angle of 45° to the horizontal polarization, all states of linear polarized light, except for plus and minus polarization, are converted to elliptically polarized light, as explained in Section 4.1. The quarter-wave plate consequently introduces an arbitrary phase difference between the horizontal and vertical light, which leaves the interferometer.

The linear polarizer behind the quarter-wave plate projects the elliptical light on a certain polarization, as seen in Section 4.1. Rotating the polarizer projects on different states. This means that with the rotation of the polarizer, the phase between the two arms can be controlled, and rotating the polarizer changes the resulting interference.

With this combination of quarter-wave plate and linear polarizer, we are consequently able to interfere the two beams, to change the phase between the two arms, and thus change the resulting interference. In other words, we can postsselect on a state $|\phi\rangle = \frac{1}{2}(|H\rangle + e^{i\varphi}|V\rangle) \otimes (|A\rangle + |B\rangle)$ where the phase φ can be chosen arbitrarily.

The projection performed by the quarter-wave plate and polarizer is therefore expressed as

$$|\phi\rangle\langle\phi| = \frac{1}{4}\Big[(|H\rangle + e^{i\varphi}|V\rangle)(\langle H| + e^{-i\varphi}\langle V|)\Big]. \tag{4.6}$$

Now calculating the intensity with Eq. 3.4 yields

$$I = \mathrm{Tr}[|\phi\rangle\langle\phi|\,|\psi\rangle\langle\psi|] = \frac{1}{4}[1 + 2\cos\alpha\sin\alpha\cos\varphi]\,, \tag{4.7}$$

clearly showing a phase dependency. The arms interfere as a result of the projection.

In Fig. 4.2 the postselection state $|\phi\rangle = |H\rangle + e^{i\varphi}|V\rangle$ is represented on the Bloch sphere. It is a vector in the x-y plane of the coordinate system. The state $|\phi'\rangle = \cos\left(\frac{\varphi'}{2}\right)|H\rangle + \sin\left(\frac{\varphi'}{2}\right)|V\rangle$ is the state we detect behind the polarizer. φ' is the rotation angle of the polarizer towards the horizontal axis. The quarter-wave plate maps $|\phi'\rangle$ on the postselection state $|\phi\rangle$, where $\varphi = \frac{\pi}{2} - \varphi'$, using the convention of Section 4.1. This way, the rotation of the polarizer sets the phase of the postselection state.

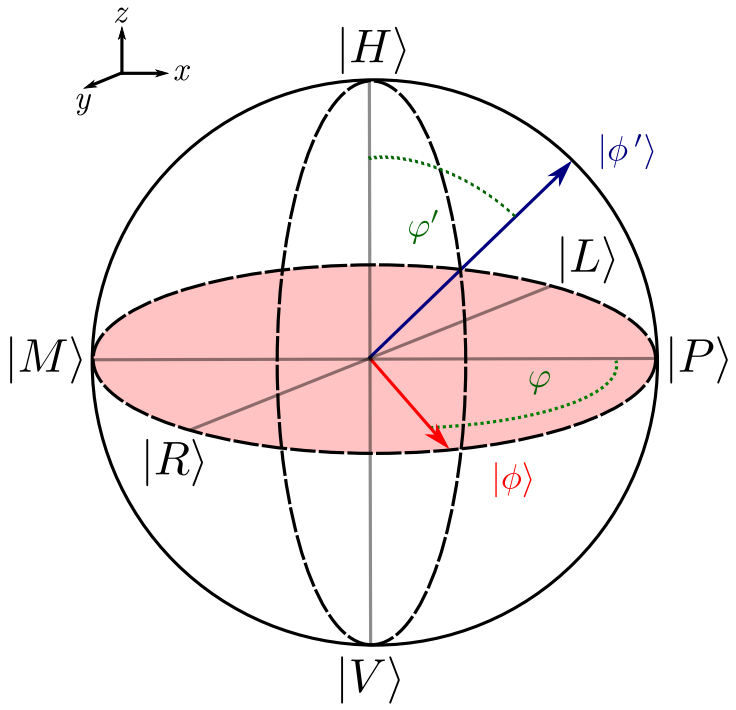

Figure 4.2.: The postselection represented in the Bloch sphere. $|\phi\rangle = |H\rangle + e^{i\varphi}|V\rangle$ is the postselection state in the x-y plane. The state $|\phi'\rangle = \cos\left(\frac{\varphi'}{2}\right)|H\rangle + \sin\left(\frac{\varphi'}{2}\right)|V\rangle$ is the state detected behind the polarizer. The quarter-wave plate maps $|\phi'\rangle$ on $|\phi\rangle$ which the following relation: $\varphi = \frac{\pi}{2} - \varphi'$.

We want to observe the interference both in the near and in the far field. Therefore, the light is split after the polarizer with a regular, non-polarizing beam splitter. One beam is then detected at a position sensor close by, the near detector,

while the other beam travels across the table to a retroreflecting prism (not pictured in Fig. 4.1) and back again before it arrives at another position sensor, the far detector.

When the rest of the setup is finalized, the two Dove prisms are placed in the arms of the interferometer. The Dove prism in arm A (Dove prism A) is placed such that it mirrors the deflection in y-direction. The prism in arm B (Dove prism B) is rotated by 90° around its axis, hence lying on its side, so that it reflects the deflection in y-direction.

4.2.3. Technical specifications and motorization of setup

In our experiment it is essential to rotate the linear polarizer to different angles while continuously measuring the position of the beam. We call this a "phase scan", as the phase φ of the postselection state is changed. The term "full phase scan" therefore means that the phase of the postselection state is changed over a whole period of φ. This phase scan could, in principal, be done by rotating the polarizer by hand and taking a picture with a CCD camera for each angle, as it was done in [57]. Then, the center of masses can be computed from the pictures and plotted versus the angles. However, rotating a polarizer by hand precisely and processing many pictures is tedious and time-consuming.

Therefore, the experiment was motorized and can now be controlled with a computer program written in C++ by Jan Dziewior, a software called "experimental control". Both the half-wave plate that sets the beam amplitudes, as well as the linear polarizer have been mounted into motorized rotary stages and connected to the software. A third motor was placed in such a way that it can block one of the interferometer arms, the other arm, or no arm at all. Blocking one arm makes it possible the compare the weak value amplification method with the far field method described in Section 3.3.

The position sensors and the reference diode are connected to a voltmeter. From the voltages obtained from the position sensor, the position of the beam is calculated with the software. The operating mode of these sensors will be explained in more detail in Section 4.5. The voltages recorded at the reference diode are used to eliminate the laser signal from fluctuations.

The experiment control software is able to rotate the polarizer while simultaneously reading out the position of the beam. It then stores the data in a file, which lists the angle of the polarizer, the x position, the y position and the total intensity in a table. This file can then be evaluated with an external program. We wrote MATLAB scripts for this purpose.

4.3. Fit algorithm for deflection measurement

The goal of the finalized setup is to measure small beam displacements d and deflections θ that occur outside of the beam, by making use of two Dove prisms. Without them, an outside deflection cannot be detected. However, we can still measure deflections inside the interferometer which allowed us to develop a fitting procedure that facilitates the evaluation of any displacement measurement data in our experiment, analogue to the alignment method presented in [8].

The goal is to determine the deflection by fitting the theoretical model to the data obtained in a full phase scan of the phase φ. The deflection can also be determined by measuring the center of masses for both single beams in the interferometer, when the other arm is blocked. From the difference of the center of masses at the near and far detector the angle can be calculated. This corresponds to the far field method of Section 3.3 and allows a comparison with the results obtained from the fit.

The measurement consists of three steps: First, one arm of the interferomenter is blocked and the position and intesity of the remaining single arm is measured at the near and far detector. Then, the other arm is blocked and the measurement repeated. Finally, both beams are unblocked, revealing the interference at the detector. The half-wave plate in the postselection setup is rotated over a full period of the phase φ and for each φ the position of the center of mass of the interference is recorded, together with the beam intensity at the center of mass. For each detector one set of data is obtained from the measurement, containing the x and y position of the beam and the beam intensity.

The angular deflection can be determined from the single beams. The center of masses of the beams have a distance l_{near} and l_{far} at each detector. The angle θ between the two beam is derived as

$$\theta = \arctan\left(\frac{|l_{\text{far}} - l_{\text{near}}|}{L}\right) \tag{4.8}$$

where L is the distance between the two detectors. Since this method only depends on the center of masses of the single beams, which can be measured precisely at high intensity, the angles obtained from the calculations are rather trustworthy. Hence, these results are used to verify the correctness of the results obtained from the fit.

To determine the deflection from the interference the equation for the pointer deflection derived in Chapter 3 is fitted to the data set. Depending on the position of the deflection it makes sense to use different models. The outside deflection can be modeled with both equations from Chapter 3, Eq. 3.40 with the projection operator on arm j, $(\hat{P}_j)_w$, here written in 2 dimensions only

$$\delta R = d + z\theta - (2d + 2z\theta)\,\mathrm{Re}[(\hat{P}_j)_w] + (2z_R\theta_x - 2\frac{z}{z_R}d)\,\mathrm{Im}[(\hat{P}_j)_w] \quad \text{(3.40 revisited)}$$

or Eq. 3.47 which uses the weak value $(\sigma_z)_w$,

$$\delta R = d\,\mathrm{Re}[(\sigma_z)_w] - z_R\theta\,\mathrm{Im}[(\sigma_z)_w] + z\theta\,\mathrm{Re}[(\sigma_z)_w] + \frac{z}{z_R} d\,\mathrm{Im}[(\sigma_z)_w]\,. \quad \text{(3.47 revisited)}$$

Due to the geometry of the Sagnac-like setup, where the two beams hit the same components, it makes sense to model the inside deflection with Eq. 3.47 as well. Deflections affecting only one arm are modeled similar to the technical noise modulations in Eq. 3.68, resulting in a pointer shift similar to Eq. 3.47, but with the weak value of a projector on the arm, $(P_A)_w$ or $(P_B)_w$, rather than $(\sigma_z)_w$. One could also use Eq. 3.47 again, but taking a factor $1/2$ into account, since only one arm of the interferometer is deflected, not both.

Since the deflection in x and y position can be modeled to be independent of each other, the 2 dimensional models can be fitted to both the data for x and y direction. For the model Eq. 3.40 one should take into account that for x and y deflection either the projector on arm A or arm B is used.

The fit function is dependent on several parameters. Most are known or can be calculated from the measurement, only three are determined by the fit. The properties of the beam are known: The waist is $w_0 = 800\,\mu\mathrm{m}$ and the wave length $\lambda = 810\,\mathrm{nm}$. This corresponds to a Rayleigh length of $z_R = 2.4\,\mathrm{m}$ and a beam divergence of $\theta_{\mathrm{div}} = 300\,\mu\mathrm{rad}$.

From the ratio of the intensities in the single arms the parameter α can be determined. As the intensity (given as a voltage) for arm A is $V_A = \cos^2\alpha$ and the intensity in arm B is $V_B = \sin^2\alpha$,

$$\alpha = \arctan\left(\sqrt{\frac{V_B}{V_A}}\right). \tag{4.9}$$

From the intensities of the interference the visibility, Eq. 3.5, of the system can also be deduced for both near and far detector:

$$\mathcal{V} = \frac{\max(V_{\mathrm{sum}}) - \min(V_{\mathrm{sum}})}{\max(V_{\mathrm{sum}}) + \min(V_{\mathrm{sum}})}\,. \tag{4.10}$$

Ideally, the visibility for both detectors is the same. Using $\mathcal{V} = 2\gamma\cos\alpha\sin\alpha$, Eq. 3.9, the overlap of the two beams, γ is calculated:

$$\gamma = \mathcal{V}\frac{1}{2}\frac{1}{\cos\alpha\sin\alpha} = \mathcal{V}\frac{1+\tan^2\alpha}{2\tan\alpha}\,. \tag{4.11}$$

The intensity distribution with respect to the phase φ follows a sinusoidal curve. The phase scan does not necessarily start at $\varphi = 0$, depending on the position of the polarizer. Hence, fitting a sinus curve to the intensity determines the phase offset.

Now, only three parameters remain: the deflection parameters d and θ and the distance from the waist to the detector z. There are two options to perform the

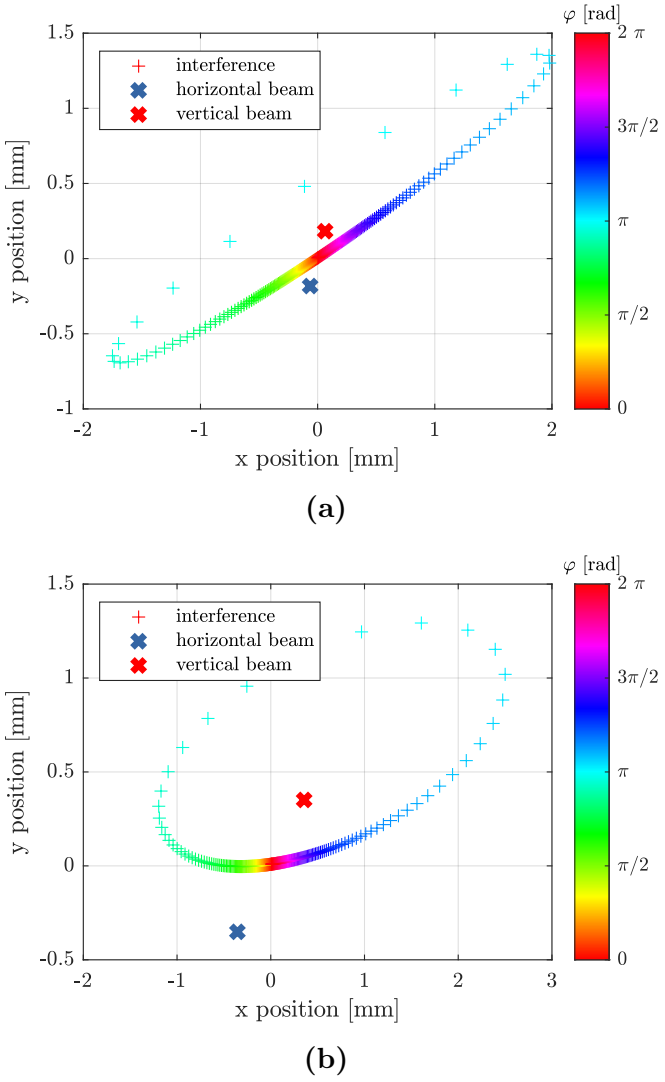

Figure 4.3.: The simulated center of mass of the interference for a deflection of $d_x = 50\,\mu\text{m}$, $d_y = 320\,\mu\text{m}$, $\theta_x = 26\,\mu\text{rad}$ and $\theta_y = 15\,\mu\text{rad}$. (a) shows the ellipse at a detector with distance 0.3 m to the waist and (b) for a detector with 2.573 m from the waist. The colors illustrate the phase between the interfering beams.

fit: The first method fits the model to the data of the near and of the far detector independently, which gives d, θ and z for each detector. Ideally, the obtained deflections are the same for each detector. The two obtained positions from the waist to the detector z_{near} and z_{far} locate the waist at the same position in a good fit.

The second method uses the known distance L between the near and far detector and fits therefore only one z position. The position of the near detector is expressed as z_{near}, while the position of the far detector is $z_{\text{far}} = z_{\text{near}} + L$. In the fit, function $\delta R(z, \varphi, ...)$ is fitted to the data from the near detector, while simultaneously a function $\delta R(z + L, \varphi, ...)$ is fitted to the data from the far detector. In the process the distance between the near fit and the far fit is minimized with respect to both

the data points obtained from the near detector and the far detector. This way, only one set of fit parameters d, θ and z is obtained from the fits to the two datasets of the near and far detector.

Both alternative fit procedures should determine the same deflections and waist position. However having two methods offers the possibility to compare the results and determine if one methods gives more reliable results.

We have generated a data set theoretically for a beam with a deflection $d_x = 50\,\mu\text{m}$, $d_y = 320\,\mu\text{m}$, $\theta_x = 26\,\mu\text{rad}$ and $\theta_y = 15\,\mu\text{rad}$. The distance for the waist to the detector was chosen as $z_{\text{near}} = 0.3\,\text{m}$ and $z_{\text{far}} = 2.573\,\text{m}$. α is chosen to be 43.5°. The generated ellipse is shown in Fig. 4.3 for both detectors. The red and blue x-es indicate the center of mass for a singe beam when the other arm of the interferometer is blocked. The colorful crosses indicate the interference pattern where the phase between the two beams is encoded in the color of the cross. A weak value amplification effect is visible, as in regions of destructive interference, that is where the phase φ is close to π, the distance between the center of mass of the ellipse and the single beams is greater than the distance between the two single beams.

Fig. 4.4 shows the calculated x (blue dots) and y positions (red dots) of the interference dependent on the phase φ. An amplification of the deflection is visible around $\varphi = \pi$. The solid lines are the fits of the model to the data, using the fit algorithm which minimizes the two fit functions $\delta R(z, \varphi, ..)$ and $\delta R(z + L, \varphi, ...)$ with respect to both data sets.

The fit calculates a deflection of

	Near, Far
d_x [mm]	0.04994
d_y [mm]	0.32063
θ_x [mrad]	0.26164
θ_y [mrad]	0.15094

(4.12)

Notice that this fit method yields one set of fit parameters for both data sets. The detector positions with respect to the waist is found as $z_{\text{near}} = 0.30146\,\text{m}$ and $z_{\text{far}} = 2.54846$ with the x position data. The y position data yields $z_{\text{near}} = 0.30925\,\text{m}$ and $z_{\text{far}} = 2.55625\,\text{m}$. The difference between the results amounts to $0.0078\,\text{m}$ for both detector positions, less than one centimeter. Alpha was found to be $\alpha = 43.5°$.

These results agree with the chosen deflections, the chosen detector positions and the chosen α.

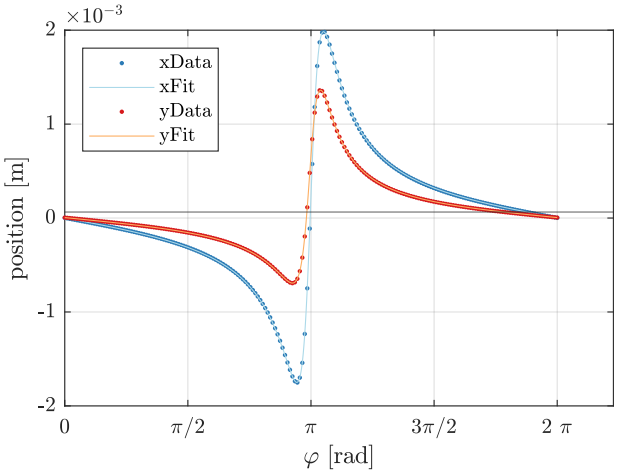

(a)

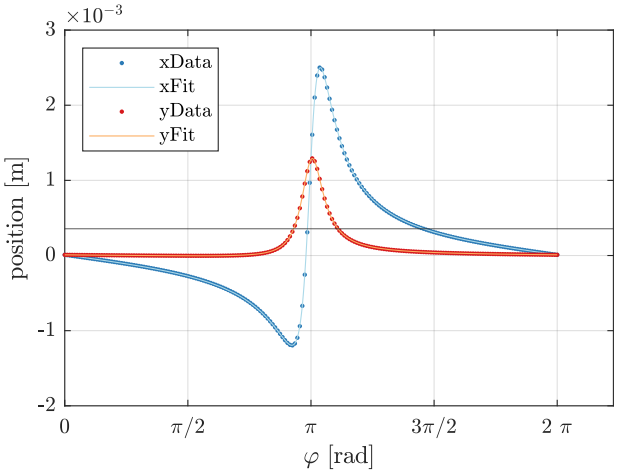

(b)

Figure 4.4.: The simulated positions of the center of mass of a interference for a deflection of $d_x = 50\,\mu\text{m}$, $d_y = 320\,\mu\text{m}$, $\theta_x = 26\,\mu\text{rad}$ and $\theta_y = 15\,\mu\text{rad}$, dependent on the phase φ. (a) shows the ellipse at a detector with distance 0.3 m to the waist and (b) for a detector with 2.573 m from the waist. The colors illustrate the phase between the interfering beams. The dots indicate the data points, while the solid lines are the model fitted to the data.

4.4. Avoiding fringes introduced by polarizing beam splitters

As it was stated in Zerweck's Bachelor thesis [57] several polarizing beam splitters (PBS) have been analyzed. All showed some irregularities and unexpected misbehavior. Some showed the best contrast when they had an angle towards the beam larger than 45°. The beam splitter we then wanted to use introduced some fringes into the vertically polarized beam.

We therefore set up another beam splitter. This one is also a cubic beam splitter. Those beam splitters consists of two glass prisms attached to each other. Unfortunately it turned out that is also introduces fringes in the reflected beam.

A possible explanation for the fringe pattern is that the surfaces where the two prisms are glued together might be imperfect. The reflection on the surface possibly introduces the fringe pattern into the beam.

Since we use a polarizing beam splitter the interferomter has effectively only one output port. Behind it, the horizontal beam was transmitted twice through the polarizing beam splitter, while the vertical beam was reflected twice. We put a half-wave plate with angle 22.5° inside the interferometer, which allowed to detect light also at the dark port. Behind it, both beam have been transmitted and reflected twice.

At the dark port no fringe pattern was visible. We conclude that the second reflection of the vertical beam caused the issue, which is avoided when using the other output port.

We therefore placed a half-wave plate inside the interferometer which rotates the beam polarizations $|H\rangle \rightarrow |V\rangle$ and $|V\rangle \rightarrow |H\rangle$. This way, no fringe pattern is introduced any more. In order to guarantee large beam separation and not block one of the arms with the wave plate mount we use a relatively large wave plate and cut the mount on one side.

4.5. Intensity dependence of the voltmeter

In our experiment we want to be sensitive in regions of low intensity, because with destructive interference the weak value amplification is the highest. We also want to have a good visibility, possibly close to 1, since the quality of the amplification is dependent on the visibility, as seen in Eq. 3.9. Therefore, we need to trust the position sensor in a large intensity range. The maximal intensity we can achieve in the experiment is 4 V, which means a voltage corresponding to a minimum intensity of 0.04 V (1% of the total voltage) would result in a visibility of 98%, which would yield a satisfying amplification. Above 0.04 V the position detection hence shouldn't introduce errors or inaccuracies, else the measurement results cannot be used. For this reason having a reliable position detection even in low intensity is essential for the experiment to work.

Unfortunately, we noticed that when reducing the intensity of the beam the detected position of the beam changed, even when all other components are not changed. For intensities lower than 0.1 V the center of mass seems to start moving, up to 2 mm to its initial position, as seen in Fig. 4.5.

The position of the beam is measured using a position resolving detector from Thorlabs [58], which is a 2D tetra lateral effect sensor. A schematics of such a sensor is shown in Fig. 4.6. The detection area of the sensor is a small chip with a resistive layer, consisting of a cathode and an anode on each side (labeled A, B, C, D in the figure). Incident light creates a photocurrent, which is detected by the electrodes. The position of the light beam is then calculated from the signal at

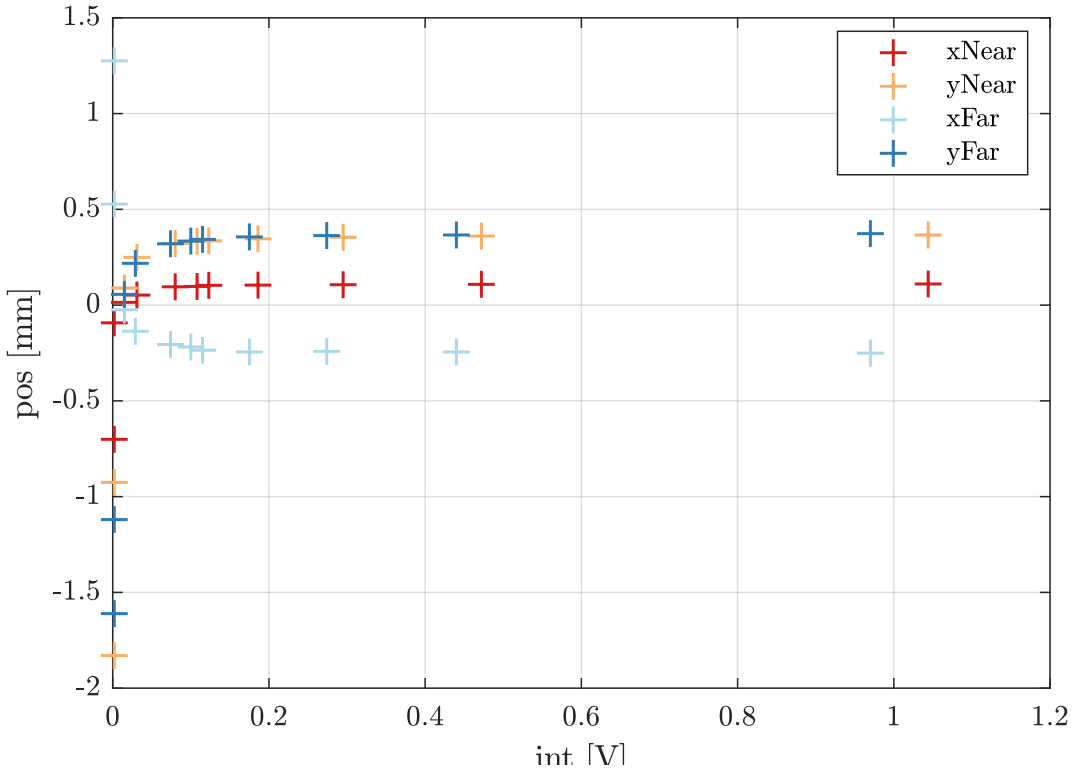

Figure 4.5.: For intensities lower than 0.1 V the detected position of the beam seems to move up to 2 mm.

each electrode, as the length to the electrode is proportional to the resistance of the layer [59]. The position $(x, y) = (0, 0)$ is defined as the middle of the detector.

The voltages created from the photocurrent in x direction, y direction and the total voltage, which is the sum of the x and y voltage, can be calculated from the signal detected at the electrodes. They are given as [59]:

$$V_x = (V_A + V_D) - (V_B + V_C) \tag{4.13}$$
$$V_y = (V_A + V_B) - (V_C + V_D) \tag{4.14}$$
$$V_{\text{sum}} = V_A + V_B + V_C + V_D\,. \tag{4.15}$$

The position of the center of mass of the beam is then calculated with the voltages for x respectively y direction, the sum voltage and the resistance lengths L_x, L_y of the sensor [59]:

$$x = \frac{L_x V_x}{2V_{\text{sum}}} \qquad y = \frac{L_y V_y}{2V_{\text{sum}}}\,. \tag{4.16}$$

These formulas directly reveal a possible source for errors. If the voltages are erroneous both nominator and denominator propagate an error. With the variance formula for error propagation the error for the position x is calculated to be

$$\Delta x = \frac{L_x V_x}{2V_{\text{sum}}} \sqrt{\frac{\Delta V_x^2}{V_x^2} + \frac{\Delta V_{\text{sum}}^2}{V_{\text{sum}}^2}} \tag{4.17}$$

where ΔV_x is the error of V_x and ΔV_{sum} is the error of V_{sum}. The measured position x' is the sum of the actual position x and the error Δx, which is a function of the actual voltages and their uncertainties:

$$x' = x + \Delta x = x \left(1 + \sqrt{\frac{\Delta V_x^2}{V_x^2} + \frac{\Delta V_{\text{sum}}^2}{V_{\text{sum}}^2}}\right). \tag{4.18}$$

Clearly, for low intensities the errors have a stronger effect on the measured position. Therefore, the position measurement for low intensities is more flawed than for high intensities.

Since, unfortunately, only the possibly inaccurate voltages are known and not the correct voltages, the actual position x cannot be determined from the data sets we obtained. However, from practical experience it is known that the position for high intensities is measured correctly. Under this assumption the following analysis was made.

The Thorlabs sensors have resistance lengths of $L_x = L_y = 10\,\text{mm}$ [58]. The voltages V_x, V_y, V_{sum} are read out by a voltmeter and from them the positions of the beam are calculated with Eq. 4.16 by the experiment control software. The voltmeter can also be accessed directly. We first read off the positions calculated with the software and then accessed the voltmeter directly to investigate the quality of the voltmeter.

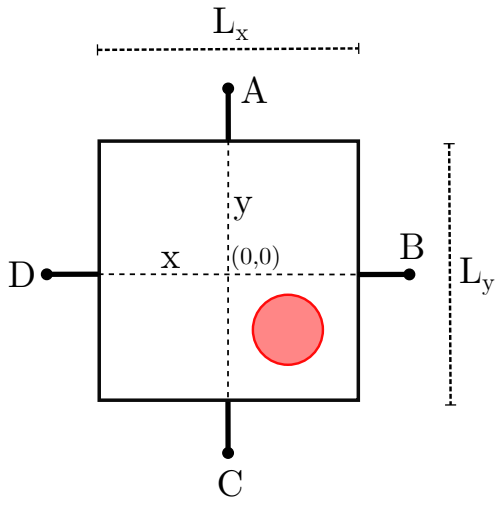

Figure 4.6.: Schematics of a 2D tetra lateral effect sensor to detect the position of a light beam. A, B, C, D are the electrodes that detect the photocurrent created by incident light.

In our lab we have three different voltmeters, which we all tested. Two of them are common ground voltmeters, the third one is a differential voltmeter. Common ground voltmeters are grounded and the voltage is measured as the difference of the potential of the ground and another point. Differential voltmeters are not

grounded, hence the voltage is measured as the difference between to points which can float around. One speaks of a floating voltage [60].

The voltmeter we used initially, which showed position errors of up to 2 mm, was a common ground voltmeter. We then tested another voltmeter of the same kind. This one showed position errors of up to 3000 mm, starting at 0.6 V.

We then tested another voltmeter, this time a differential voltmeter thoroughly and compared the findings to the ones of the initially used voltmeter. To test the voltmeters we compared data obtained from several measurement devices with each other. One measurement device was a power meter, which is able to measure the power of an optical signal in watts. The other measurement device was a multimeter, which is, like the voltmeter, able to read off the voltages detected at the position sensors.

With this method we were able to inspect several aspects at the same time. In a good voltmeter we assume that with decreasing total voltage the voltages in the channels for x and y position also decrease linearly. To see if the voltmeter behaves linearly the voltage of the reference diode was plotted against the intensity measured with the power meter. The reference diode is able to detect voltages up to 9 V. While the reference diode behaved linearly up to 8 V for the differential voltmeter, as shown in Fig. 4.7a, it was only linear until 4 V for one of the common ground voltmeters which we tested, showed in Fig. 4.7b. This is a good indicator that the last voltmeter might not behave correctly.

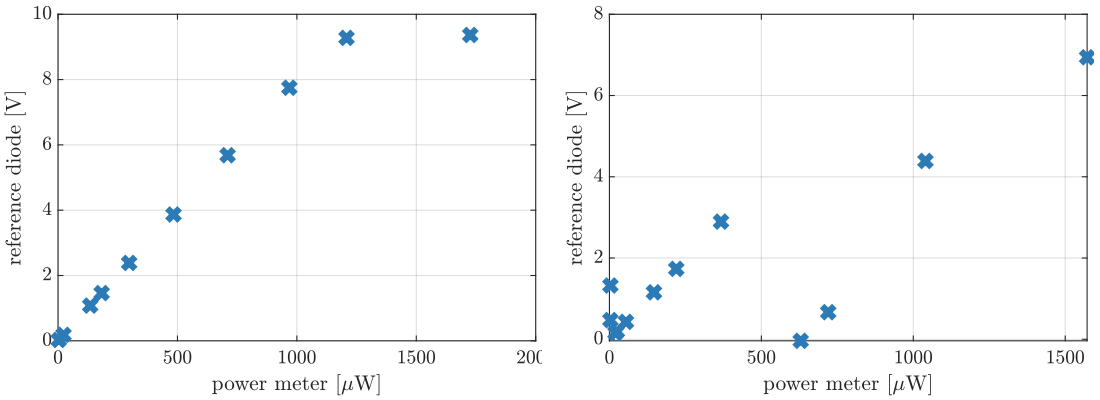

(a) **(b)**

Figure 4.7.: (a) The reference voltage depending of the power of the beam measured with a power meter for the differential voltmeter and (b) for a common ground voltmeter. The common ground voltmeter shows a linear behavior only until 4 V.

As a second step the voltages of the several channels were plotted against the total voltage, the reference diode voltage or the intensity measured with the power meter. This way we were able to tell if the individual channels of the voltmeter

showed non-linearities. For the two common ground voltmeters this was indeed the case, while the differential voltmeter showed only linear behavior. In Fig. 4.8 the voltages from the various channels are depicted depending on the reference voltage. Clearly, one common ground voltmeter behaves non-linear, as shown in Fig. 4.8b, while the other two voltmeters seem to behave in a linear way.

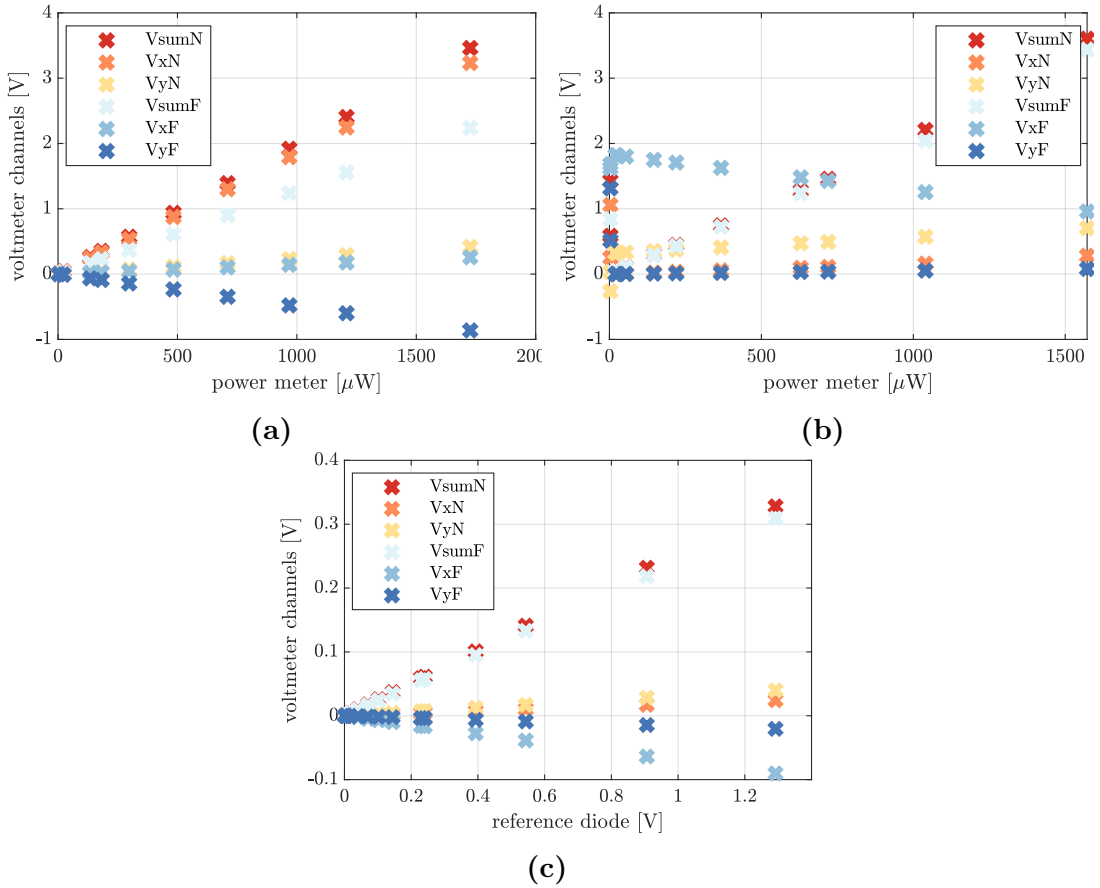

Figure 4.8.: (a) The voltmeter channels depending on the beam intensity measured with a power meter for the differential voltmeter, (b) The voltmeter channels depending on the beam intensity for one common ground voltmeter and (c) the voltmeter channels depending on the reference diode voltage for the other common ground voltmeter. The first common ground voltmeter shows non-linearities.

We didn't continue the testing of the common ground voltmeter with showed position offsets of up to 3000 mm, because this clearly does not behave accurately given the detector size of 1 cm^2. We continued the measurement with the other two voltmeters that didn't show this huge position offsets. We measured the voltages at the position sensors with a multimeter. It has three channels, hence we were able read out the x, y and sum voltage of the near detector. We attached the multimeter to the voltmeter channels of the near detector to measure these

voltages simultaneously. From Eq. 4.17 it becomes clear that for small voltages even small errors influence the signal drastically. Therefore, the substraction of the background is very important. In Fig. 4.9 the effect of the background subtraction is shown. If the background is not subtracted the positions obtained from the voltmeter start to drift already at 0.2 V. The readout with subtracted background and the readout from the multimeter stay stable until very low voltages.

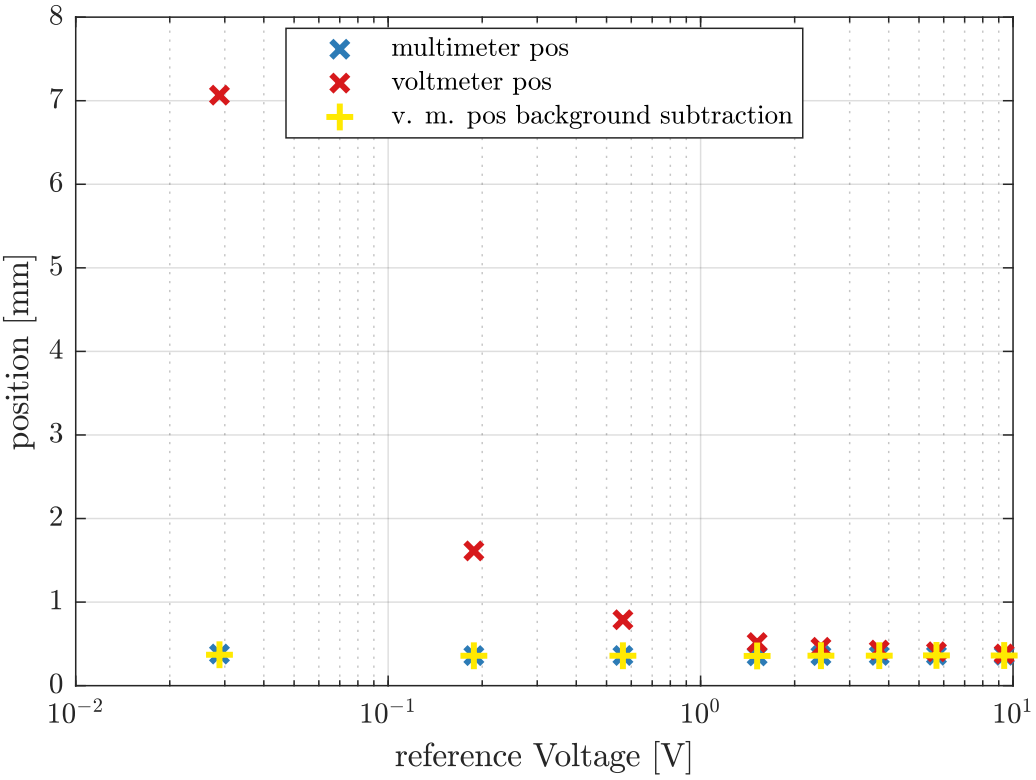

Figure 4.9.: The positions for the x-near channel calculated with the multimeter and the voltmeter. The blue markers indicate voltmeter data without the background being subtracted, the yellow ones with background subtraction.

Finally, having ruled out one voltmeter and having compared the quality of the two remaining voltmeters we analyzed the starting point of the position drift in more in detail. This was done by measuring the position for certain intensities with both voltmeters. The result is shown in Fig. 4.10. The positions obtained with the common ground voltmeter (vM08) are marked with crosses, while the positions obtained from the differential voltmeter (vM04) are marked with x-es. It is clearly visible that at intensities of 0.02 V the positions obtained with the common ground voltmeter have drifted up to 0.2 mm, while the positions for the differential voltmeter have drifted less than 0.05 mm. Hence, the positions calculated with the differential voltmeter seem to be reliable for a lower voltage.

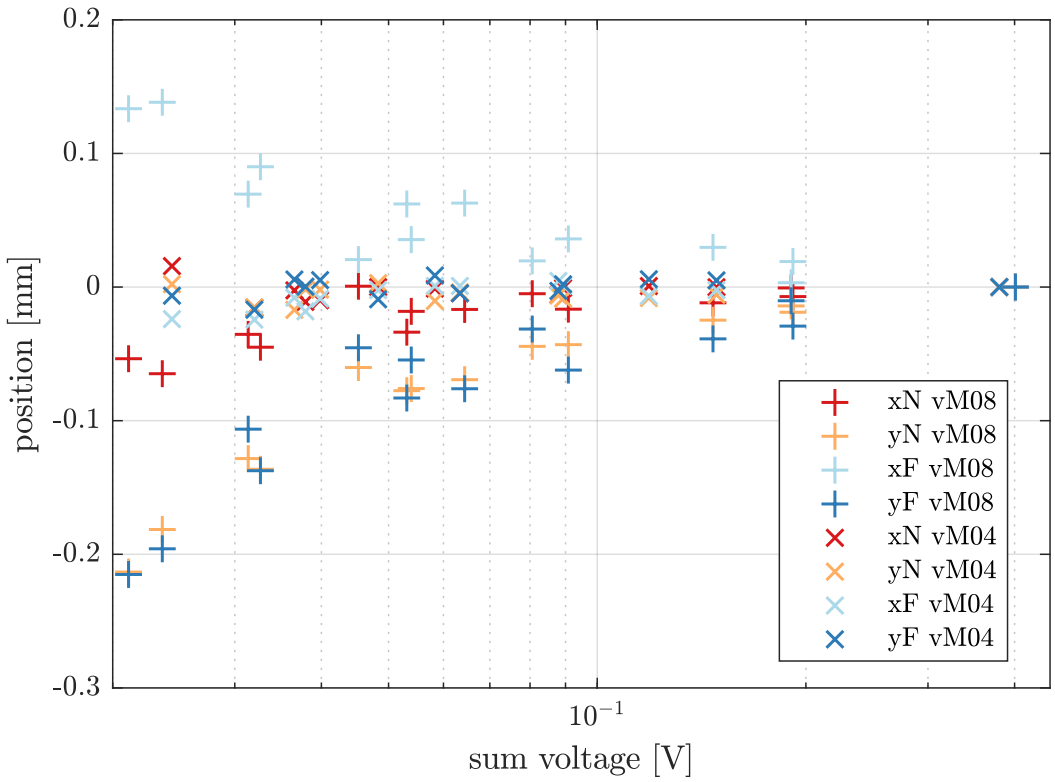

Figure 4.10.: The positions obtained with the common ground voltmeter vM08 (crosses) and with the differential voltmeter vM04 (x-es). It is visible that at intensities of 0.02 V the positions obtained with the common ground voltmeter have drifted up to 0.2 mm, while the positions for the differential voltmeter have drifted less than 0.05 mm.

As a result of the analysis we now make use of the differential voltmeter for the experiment.

4.6. Calibration of the postselection unit

In order to achieve a reliable weak value amplification, the postselection is crucial. On the one hand it is important that the postselection state is well defined. On the other the spatial mode, acting as the pointer, should not be altered by the postselction. Unfortunately the postselection utilizing waveplates, which we initially chose, showed both of these problems.

The postselection unit initially consisted of a quarter-wave plate and a linear polarizer. With both components it is possible to project on the desired postselection state, as explained in Section 4.2. If one arm of the interferometer is blocked, i.e. only one beam with either horizontal or vertical polarization propa-

gates in the interferometer, the light is transformed to circular polarized light by the quarter-wave plate, while the amplitude $\cos\alpha$ or $\sin\alpha$ remains the same.

This has two consequences. Firstly, since we only have one beam at the output, there is no interference. Rotating the polarizer will therefore not change the center of mass of the intensity distribution. Secondly, the amplitude of the intensity distribution should remain constant, as the linear polarizer just reduces the intensity of circular light by one half, like explained in Section 4.1.

These expectations did not match with the actual behavior of the postselection unit. We observed that the center of mass of the intensity distribution changed for different angles of the polarizer when one arm of the interferometer was blocked, resulting in an circular structure on the screen, as seen in Fig. 4.11a, Fig. 4.11b. Moreover, we observed that the intensity oscillated periodically, see Fig. 4.11c, Fig. 4.11d. We performed several measurements in a short period of time, which all yielded these findings, pictured as different curves in Fig. 4.11.

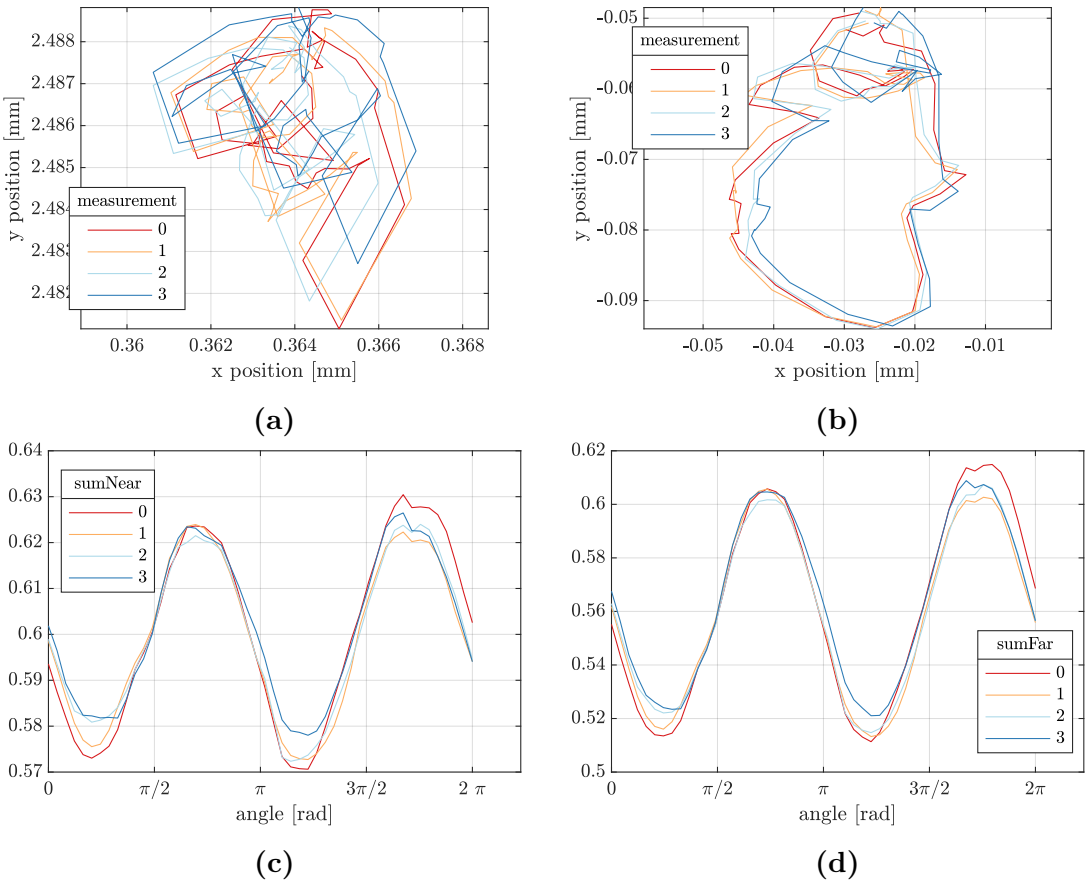

Figure 4.11.: For different angles of the polarizer the position of the center of mass changes (a) in the near and (b) in the far field. An intensity modulation is also visible (c) in the near field and (d) in the far field.

4.6.1. Position changes from rotation of optical components

One possible explanation for the movement of the beam when rotating the polarizer or the halt-wave plate is that these optical components are not plain but slightly wedge-shaped. If the facettes of an optical component are parallel, the beam passes through without getting an angle towards its initial propagation direction. If the facettes are not parallel, according to Snell's law [10] an angle is introduced to the beam. When rotating the component the angle of the beam towards the surface changes, therefore the propagation direction of the beam changes, which can be seen as a position change of the beam on the screen.

The manufacturer of the wave plates specifies a beam defection of up to one angular second. Given the distance from the wave plate to the far detector of about 2.5 m this corresponds to a beam deflection of 12 µm, which is around one third of the deflection we measured.

With Snells' law and geometrical considerations it is possible to find an expression for the angle θ of the beam after passing through the wave plate dependent on the angle α of the surface of the wedge for a straight incident beam:

$$\theta = n(1 - \frac{1}{n})\alpha\,. \tag{4.19}$$

Here, n is the refraction index of the component. This allows to calculate the diameter x of the structure on the screen, which is given by $x = z\theta$ where z is the distance to the screen.

Taking rough approximations for the parameters from our findings, namely $x = 100\,\mu\text{m}$ for the diameter, $z = 2.5\,\text{m}$ and $n = 1.5$ we arrive at an angle for the wedge of $\alpha = 0.005°$. This means that even small deformations of the wave plate could cause a relatively large beam movement.

Another possible explanation is that the optical components are mounted such that they change their angle to the beam for different positions. When rotating them, this results in different positions offsets to the initial beam propagation, which can be detected on the screen as an circular structure. It is also quite possible that the reason is a combination of both, a component with irregular facettes which changes its angle towards the beam with different positions.

To find out weather one component minimizes the circular structure visible at the screen we testes several available components. All four linear polarizers we examined showed the same behavior. The polarizer with the best behavior created structures with a approximate diameters of 5.7 µm for x- and 6.8 µm in y-direction. In the far field the structure had diameters of approximately 31.3 µm and 45.0 µm.

For the polarizer with the worst behavior we got structures with near field diameters of $(8.7\,\mu\text{m}, 9.1\,\mu\text{m})$ and far field diameters of $(110.2\,\mu\text{m}, 109.8\,\mu\text{m})$.

We observed that the diameters of all structures in the far field are roughly 10 times the diameters in the near field, which corresponds well to the distance between the near and far detector of around 218 cm.

Our analysis also included half-wave plates. In order to use a half-wave plate in the postselection unit we exchanged the rotatable linear polarizer with a rotatable half-wave plate and an fixed linear polarizer. This setup is able to perform the same postselection as quarter-wave plate and linear polarizer. The quarter-wave plate introduces a relative phase between the vertical and horizontal beam, resulting in elliptical light. The HPW then changes the ratio of horizontal and vertical polarization in the light, effectively changing the phase between the the beams for different orientations. The linear polarizer then projects onto a certain polarization, performing the postselection. By rotating the half-wave plate we are therefore able to perform a full phase scan.

We tested this setup for five half-wave plates in total. Four of them introduced position modulations into the beam. The wave plate with the best behavior created circular structures with diameters (5.4 µm, 5.0 µm) near and (39.1 µm, 37.7 µm) far. We measured the wave plates several times, opening and closing the blinds of the optical table in between. We wanted to see if this would change the positions drastically, which was not the case.

The wave plate with the worst behavior created structures with diameters (75.3 µm, 725.5 µm) near and (331.1 µm, 1169.1 µm) far. The other two wave plates created structures slightly bigger than the structure of the best component.

The fifth wave plate showed unexpected behavior. In some position it created a big structure with a diameter of around 100 µm in y direction. In another position, found by chance, it did not create an circular structure at all (except for noise). The intensity fluctuation however remained.

From this fact we assume that it is possible to find an optimal position for the wave plate which minimizes the position change. If the waveplate is mounted such that its angle to the beam changes, leading to a change of the introduced position offset the optimal position is in the middle of the wave plate. It is also possible that the facettes of the optical components are parallel at a certain position, which could be found by systematic investigation.

We therefore mounted the half-wave plate on a rotation and translation stage. This allows to measure the deflection caused by the wave plate systematically for different positions and angles to the beam. The wave plate was moved to five different positions in equidistant steps of 0.5 mm. For each position the wave plate was then rotated up to ±5°. For each position and angle we then scanned the phase and evaluated the resulting structure.

With these results it was possible to determine the best position of the wave plate, which would create the smallest structure. If the beam hits the wave plate in the center and has (almost) no angle towards it, no circular structure is cre-

ated. The position of the beam still fluctuates around, but randomly and not systematically. We can therefore conclude that this is noise, most likely due to for example laser fluctuations or air movement. If the beam however hits close to the edge of the wave plate and has a larger angle to it, a circular structure is created.

Fig. 4.12 shows some result of the measurement series in the near and far field. At positions 4, 5, 6 the beam has a small angle to the wave plate and hits in the middle. The beam fluctuations are caused by noise. At positions 9 and, more drastically, 10 circular structures with diameters of up to 100 µm in the near field are visible. When the data was taken for those positions, the beam had a larger angle to the half-wave plate and, for position 10, almost hit the edge of the wave plate.

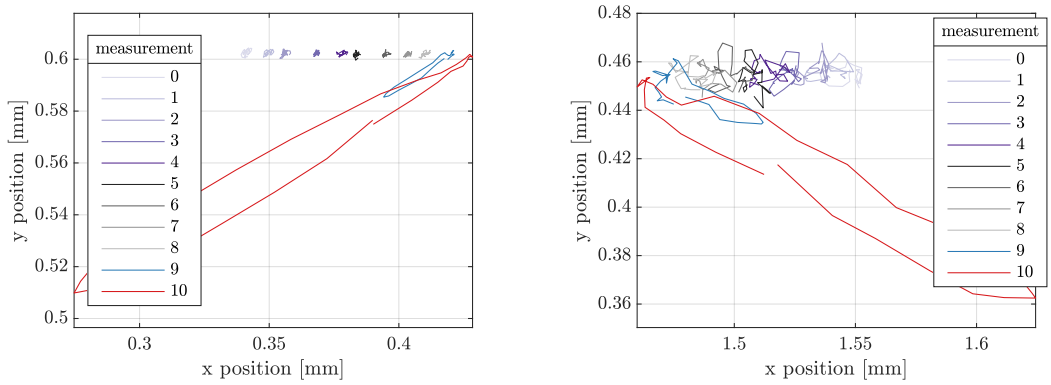

(a) **(b)**

Figure 4.12.: Position fluctuations caused by the half-wave plate for different angles of the half wave plate to the beam, (a) in the near field and (b) in the far field.

Concluding, hitting the wave plate close to the middle did eliminate the position changes when rotating the wave plate, possibly because it is mounted such that the angle to the beam changes. Also, the facettes of the wave plate might be more parallel in the middle, thus only creating a circular structure if the laser beam does not hit its middle.

Unfortunately placing the half-wave plate in a good positions did not eliminate the intensity modulations. This suggest that these fluctuations are caused by the quarter-wave plate.

4.6.2. Polarization analysis and postselection state

A possible explanation for the intensity modulation for different phases is that the quarter-wave plate does not work perfectly. A quarter-wave plate with angle 45° has the plus and minus polarization as eigenaxis, which means that it does not alter plus and minus polarized light passing trough the wave plate. Therefore,

in order to set the quarter-wave plate to 45° it was put in between an plus and a minus polarizer, and fixed so that the intensity behind the minus polarizer is minimal. This way one can assure that the quarter-wave plate rotates light indeed between the plus and minus polarization. However, the rotation on other states might not work equally well, so that the quarter-wave plate transforms horizontal and vertical light to elliptical light rather than circular light. The overlap of the polarizer state and the state of light after traversing the quarter-wave plate is therefore not one half, independently of the angle of the polarizer as it is for circular light, but it now depends on the angle of the polarizer. The postselection is therefore not performed on an arbitrary state in the x-y plane of the Bloch sphere, $|\phi\rangle = |H\rangle + e^{i\varphi}|V\rangle$ anymore. Rather, a postselection on a state

$$|\phi'\rangle = \sqrt{f(\varphi)}\,|H\rangle + e^{i\varphi}\sqrt{1-f(\varphi)}\,|V\rangle\ , \tag{4.20}$$

is performed, which lies in a plane tilted to the x-y plane. $f(\varphi)$ is a function depending on the phase. This postselection on a different state leads to intensity fluctuations when a beam with only horizontal or vertical component passes the postselection unit.

Another possible explanation is that the polarization inside the interferometer changes. If a considerate amount of vertical light travels in the horizontal polarized arm of the interferometer rotating the polarizer or half-wave plate would also result in an intensity fluctuation.

We therefore checked whether the polarization is rotated inside the interferometer. This was accomplished by determining at which angles a variable polarizer projects to horizontal and vertical polarization in a beam in front of the interferometer and in the two polarized beams inside the interferometer. We then compared the findings. The angles were the same up to 1°, which is possibly due to the inaccuracy of the measurement method. We also observed that the intensity modulation remained when a horizontal polarizer was placed right in front of the quarter-wave plate.

This result shows that the polarization stays stable and well-defined in a pure state while passing the interferometer. We can therefore exclude polarization drifts as a reason for the modulations in the intensity while changing the phase.

Therefore it is indeed very likely that the intensity modulations are caused by the quarter-wave plate not performing the correct postselection. As a consequence we can neither use the unit with the quarter-wave plate and linear polarizer, nor the quarter-wave plate - half-wave plate - linear polarizer unit for the postselection, as it does not perform the postselection on the right state.

In order to change the phase between the beams we hence have to use another method. Several methods are possible. It is, for instance, possible to change the phase between the beams with two yttrium-vanadate (YVO) crystals. One of these birefringent crystals separates the beams while the other, placed parallel to the first one, combines the two resulting beams again. Due two the different paths

the two beams travel a relative phase is introduced, changing with different angle of the YVOs to the beam. A major disadvantage of this method is that aligning the two YVOs so that they are parallel is rather tedious. Both YVOs could be mounted on the same rotation stage, so that they would not move relative to each other once the alignment is done.

Another idea would be to change the phase with a liquid crystal phase retarder. A liquid crystal phase retarder is made out of liquid crystal molecules. The alignment of the molecules changes with an applied voltage, changing the effective retardance of the system [61]. The liquid crystal is placed between two linear polarizers of perpendicular polarization. From the input and output intensities the retardance for different applied voltages is determined [62]. With this knowledge the desired phase can be set by applying a certain voltages. We are currently setting up such a device and will hopefully soon be able to postselect the correct polarization without changing the position of the beam.

4.7. Deflection measurement relative to Dove prism

During the process of setting up the experiment we used the fit algorithm to evaluate many measurements of the deflections inside the interferometer. We also used the method when aligning the Dove prisms, taking preliminary data of deflections relative to the Dove prisms.

By introducing the Dove prisms to the aligned interferometer, they introduce a deflection inside the interferometer. When changing to the reference frame of the Dove prism, however the Dove prisms mirror the deflections a beam carries. We can therefore say that we have measured the deflection of the beams relative to the Dove prisms.

A Dove prism has an axis, around which a displacement is mirrored, as explained in Chapter 3. However, only deflections in one direction are affected by the prism. Therefore, two prisms are introduced into the interferometer, to be able to measure both deflections in x and y direction.

The two Dove prism are inserted to the setup as shown in Fig. 4.1. The Dove prism in arm A is placed so that it reflects the beam deflection in y-direction (y-Dove prism). The prism in arm B reflects the deflection in x-direction (x-Dove prism). The y-Dove prism is placed on a translation stage which moves in the y-direction of the setup. This way, the axis of the prism can be placed on the height of the beam, and by rotating the prism along the x-axis it can be aligned. However, the mount also allows to rotate the prism around the y-axis, which introduces a offset in x-direction to the beam. The offset can be compensated by the Dove prism in arm B. It is mounted on a translation stage moving in x-direction. This way the axis of the prism can be placed on the height of the beam, while also compensating for the offset introduced by the other prism. Rotation

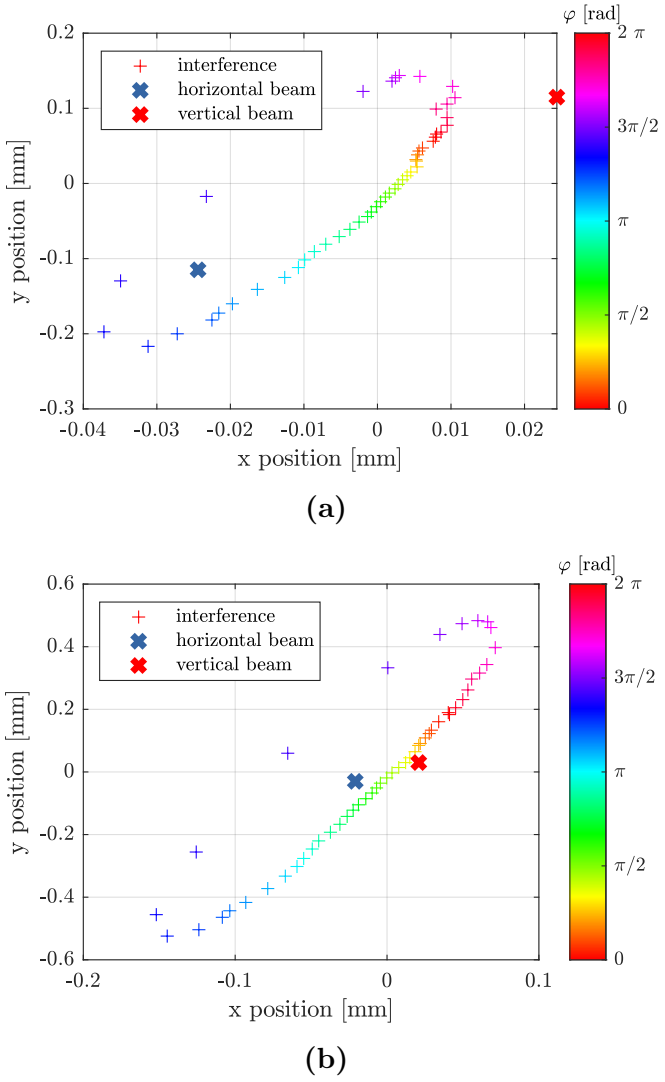

Figure 4.13.: The position of the center of mass of the interference pattern is depicted for different phases φ. (a) shows the data obtained from the detector in the near field, (b) the data from the detector in the far field.

around the y-axis allows to align the prism. The mount of the prism cannot be rotated around the x-axis, hence no additional offset in y-direction is introduced.

The Dove prisms are then aligned by translating and rotating them relative to each other. Due to the different degrees of freedom the alignment is not straight forward, but feasible with iterative steps.

In Fig. 4.13 the result of a phase scan for beam deflections relative to the Dove prisms is shown. It depicts the center of mass of the intensity distribution on the position detector in the far field. The red and blue x-es correspond to the positions of the single arm. The colorful crosses correspond to the center of mass of the interference. The color indicated the phase φ between the interfering beams.

Clearly, the the center of mass lies for several phases φ between the position of the single arms. This is the region of constructive interference, when φ is close to 0 or 2π. In this region the amplification is not very large, as predicted by the weak value formalism. The distance of the center of mass to the single beam positions is much larger for other φ. Take for instance the dark blue markers in Fig. 4.13b. There, the interference is destructive, the phase is around $\varphi = \pi$. The distance to the blue marker is almost three times the distance between the blue and red marker. This indicates an amplification of factor 3.

In Fig. 4.14 the projection of the positions shown in Fig. 4.13 on the phase φ is depicted, together with the obtained fits from the fit algorithm which fits the model independently to the data sets from the near and far detector. The blue markers correspond to the x positions and the green markers to the y positions. The solid lines are the fits to the theoretical model.

Evidently, the fits are not very close to the data points. This is also visible regarding the fit parameters. The fit determines the deflections for the near field and far field detector to be

	Near	Far
d_x [mm]	0.02356	0.00888
d_y [mm]	0.03851	-0.12989
θ_x [mrad]	0.00463	0.02419
θ_y [mrad]	0.03906	0.05236 .

(4.21)

Apparently, the results for near and far field differ significantly from each other. Calculations from the single beams reveal relative angles between the beams

$$\theta_x = 0.00310\,\text{mrad}\,, \tag{4.22}$$

$$\theta_y = 0.07556\,\text{mrad}\,. \tag{4.23}$$

We see that the differences between the angles for x position is one order higher than the angle calculated from the single beams. This shows that the fit results are imprecise or error-prone. For the y-direction the difference and the angle calculated from the single beams are of the same order. In a good measurement the results for the near and far field data should be close to each other, ideally the same.

Apparently, the fit does not not work as desired. A reason seems likely: As described in Section 4.6 due to faulty behavior of the quarter-wave plate the postselection is not performed on the desired state $|\phi\rangle$, but on another state. Since the model postselections on the desired state, model and empirical data do not match, resulting in a discrepancy, as observed for the preliminary data. However, we have showed that displacements relative to the Dove prism can indeed be weak value amplified, as seen in Fig. 4.13.

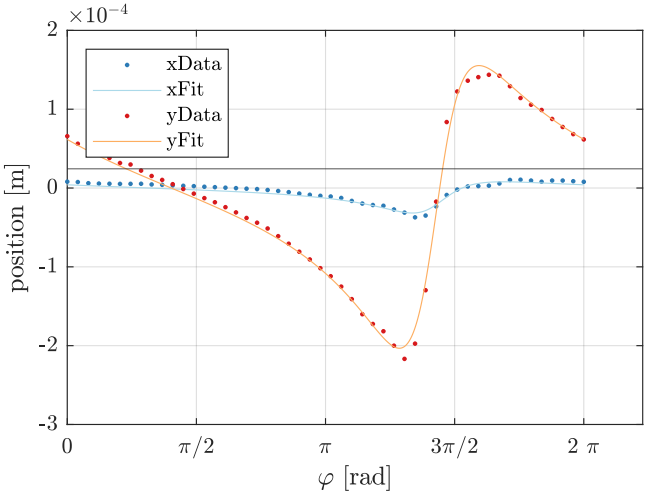

(a)

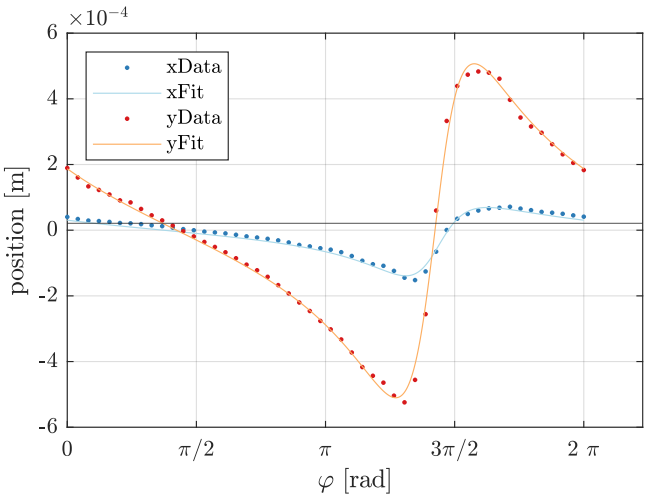

(b)

Figure 4.14.: The projection of the x and y positions of the center of mass of the interference pattern on different phases φ. The markers are the data points taken in the measurement. The solid lines are the fits to the theoretical model. (a) shows the data obtained from the detector in the near field, (b) the data from the detector in the far field.

We are currently calibrating a liquid crystal retarder to overcome the obstacles caused by the quarter-wave plate. Once this is done we hope that we can perform a correct postselection, which results in data matching to the theoretical model. Then, fitting the model should determine the beam deflection correctly and precisely.

Concluding, some more steps await their realization When the liquid crystal retarder is set up we will align the Dove prisms again. While doing so we can measure data for the beam displacement relative to the Dove prisms and therefore examine if the fit algorithm provides the correct results. If this is confirmed and the Dove prisms aligned, we will perform the actual measurement: The mirrors in front of the interferometer will be displaced and tilted slightly. The measurement

method should determine the deflections. Ideally, the fitted results match with the deflections we introduced with the mirrors.

A step further is also planned: One of the outside mirrors shall be connected to a piezoelectric crystal, which oscillates in accordance with an applied signal. This signal could for example be a audio signal, like a song. The oscillation of the mirror introduces different deflections to the interferometer. Setting the phase of the postselection state $|\phi\rangle$ so that the weak value amplification is high, we hope to amplify the audio signal. If this is confirmed, the measurement setup presented here would essentially work as a "spying device".

5. Conclusion

In the thesis, an experiment that is able to measure small beam deflections was introduced. It builds on the method of weak value amplification to enhance the precision of the measurement. In contrast to other weak value amplification experiments, the interaction region is not inside the interferometer but outside, making it possible to detect deflections and displacements of the beam which happen outside of the measuring device.

The technique is implemented using a Sagnac-like interferometer with spatially separated arms. In one of the arms of the interferometer a Dove prism is placed, which mirrors a beam deflection along its axis. This way, the beams are deflected relative to each other. The deflection manifests as a change of the resulting interference of the overlapping beams, which, when properly evaluated, provides information about the deflection and displacement.

We modeled the experiment in two dimensions and compared the expected performance with respect to noise with two alternative measurement methods that do not employ the concept of weak value amplification. The first method measures the beam in the far field, while the second method uses a lens to amplify beam deflections. We demonstrated numerically that the signal-to-noise ratio of the weak value amplification method is at best as good as the one of the alternative methods. However, we showed that the weak value amplification method can suppress technical noise appearing behind the interferometer, which is not possible with the alternative methods. Here, weak value amplification has the potential to outperform the alternative methods.

We described the experimental realization in detail, including obstacles we encountered while setting up the experiment. For several, we explained how we were able to overcome them. For others, we proposed solutions. Several optical components showed unwanted behavior: The polarizing beam splitter in the interferometer introduced fringe pattern into the polarized beam, which was reflected twice. A half-wave plate was placed in the interferometer, which changes the polarization of the beam. This way, both beams are reflected and transmitted once, eliminating the fringe pattern. A half-wave plate deflected a beam differently for different positions. This resulted in a position change on the detector for one interferometer beam when the other beam was blocked. We hypothesize that this stems from the wave plate having a wedge-shaped form or being mounted such that its angle to the beam changes for different positions. To overcome the issue,

we systematically investigated the deflection for different positions and found a position where the beam passed the wave plate undeflected.

In the setup a voltmeter is used to measure the beam positions. The voltmeters measured an apparent position deviation in regions of low intensities. We compared three voltmeters that were at our disposal to find the one which measures the smallest position drift.

A serious problem came up with the quarter-wave plate of the postselection setup. Rotating the polarizer behind the wave plate changes the phase of the interferometer, performing the postselection. For a horizontally polarized beam, when the other beam in the interferometer was blocked, periodic intensity fluctuations were observed for different phases, which should not be the case for the desired postselection. Possibly, the quarter-wave plate changes horizontally and vertically polarized light to elliptical light and not to circular light, as a perfect quarter-wave plate would do. Postselection for different phases then results in different intensities. As a solution we proposed utilizing a liquid crystal retarder to introduce the phase difference between vertical and horizontal light. It is currently calibrated in the laboratory.

We also presented a fit algorithm to extract the deflections from empirical data. We observed that for our preliminary laboratory data the results for the near and far field differed. We attribute this error to the faulty behavior of the quarter-wave plate, which is not captured by our model. Hence model and empirical data do not match.

We expect that we will be able to perform a correct postselection as soon as the liquid crystal retarder is implemented. We will then align the Dove prisms again. Once this is done, we will determine small beam deflections to verify the expected performance of the experiment.

A further step is also planned: One of the outside mirrors shall be connected to a piezoelectric crystal, which oscillates in accordance with an applied signal. This signal could, for example, be an audio signal, like a song. The oscillation of the mirror introduces different deflections to the interferometer. Setting the phase so that the weak value amplification is high, we hope to amplify the audio signal. If confirmed, the measurement setup presented here would essentially work as a "spying device".

A. Abbreviations

AAV	Aharonov, Albert & Vaidman
BS	beam splitter
LC	liquid crystal
MZI	Mach-Zehnder interferometer
HWP	half-wave plate
PBS	polarizing beam splitter
QWP	quarter-wave plate
SNR	signal-to-noise ratio
TSVF	Two-state vector formalism
WV	weak value
WVA	weak value amplification
YVO	yttrium-vanadate

List of Figures

Bibliography

[1] John von Neumann, *Mathematical Foundations of Quantum Mechanics*, Princeton University, 1955, ISBN: 0-691-08003-8 .

[2] Yakir Aharonov, David Z. Albert, and Lev Vaidman, "How the Result of a Measurement of a Component of the Spin of a Spin-1/2 Particle Can Turn Out to be 100", *Physical Review Letters*, vol. 60, no. 14, p. 1351, 1988.

[3] N. W. M. Ritchie, J. G. Story, and Randall G. Hulet, "Realization of a measurement of a "weak value"", *Phys. Rev. Lett.*, vol. 66, no. 9, p. 1107, 1991.

[4] Onur Hosten and Paul Kwiat, "Observation of the Spin Hall Effect of Light via Weak Measurements", *Science*, vol. 319, no. 5864, pp. 787–790, 2008.

[5] P. Ben Dixon, David J. Starling, Andrew N. Jordan, and John C. Howell, "Ultrasensitive Beam Deflection Measurement via Interferometric Weak Value Amplification", *Physical Review Letters*, vol. 102, no. 17, p. 173 601, 2009.

[6] David J Starling, P Ben Dixon, Andrew N Jordan, and John C Howell, "Precision frequency measurements with interferometric weak values", *Physical Review A*, vol. 82, no. 6, p. 063 822, 2010.

[7] Omar S. Magaña-Loaiza, Mohammad Mirhosseini, Brandon Rodenburg, and Robert W. Boyd, "Amplification of angular rotations using weak measurements", *Physical Review Letters*, vol. 112, no. 20, p. 200 401, 2014.

[8] Jan Dziewior *et al.*, "Universality of local weak interactions and its application for interferometric alignment", *Proceedings of the National Academy of Sciences of the United States of America*, vol. 116, no. 8, pp. 2881–2890, 2018.

[9] Courtney Krafczyk, Andrew N Jordan, Michael E Goggin, and Paul G Kwiat, "Enhanced weak-value amplification via photon recycling", *Physical review letters*, vol. 126, no. 22, p. 220 801, 2021.

[10] Wolfgang Zinth and Ursula Zinth, *Optik*, de Gruyter, 2018, ISBN: 978-3-11-049501-0 .

[11] Eugene Hecht, *Optik*, de Gruyter, 2018, ISBN: 978-3-11-052664-6 .

[12] Mark Fox, *Quantum Optics: An Introduction*, Oxford University Press, 2006, ISBN: 978-0-19-856673-1 .

[13] Pericles S. Theocaris and Emmanuel E. Gdoutos, *Matrix Theoryof Photoelasticity*, Jay M. Enoch, Ed., Springer-Verlag Berlin Heidelberg GmbH, 1979, ISBN: 978-3-662-15807-4 .

[14] Javier Alda, "Laser and Gaussian Beam Propagation and Transformation", *Encyclopedia of Optical Engineering*, pp. 999–1013, 2003.

[15] David J. Griffiths, *Quantenmechanik. Lehr- und Übungsbuch*, Pearson, 2012, ISBN: 978-3-86894-114-2 .

[16] J. J. Sakurai, *Modern Quantum Mechanics. Revised Edition*, San Fu Tuan, Ed., Addison-Wesley Publishing Company, 1994, ISBN: 0-201-53929-2 .

[17] Ryszard Horodecki, Paweł Horodecki, Michał Horodecki, and Karol Horodecki, "Quantum entanglement", *Rev. Mod. Phys.*, vol. 81, no. 2, p. 865, 2009.

[18] Wayne Myrvold, "Philosophical Issues in Quantum Theory", *The Stanford Encyclopedia of Philosophy*, Edward N. Zalta and Uri Nodelman, Eds., Metaphysics Research Lab, Stanford University, 2022, *Online; accessed 17th April 2023*.

[19] Maximilian Schlosshauer, "Decoherence, the measurement problem, and interpretations of quantum mechanics", *Reviews of Modern physics*, vol. 76, no. 4, p. 1267, 2005.

[20] Abraham G. Kofman, Sahel Ashhab, and Franco Nori, "Nonperturbative theory of weak pre- and post-selected measurements", *Physics Reports*, vol. 520, no. 2, pp. 43–133, 2012 ISSN: 0370-1573.

[21] David Bohm, "A Suggested Interpretation of the Quantum Theory in Terms of "Hidden" Variables. I", *Phys. Rev.*, vol. 85, no. 2, p. 166, 1952.

[22] Maria Galli, "Measurement of average Bohmian trajectories of photonsin a double slit interferometer", *Published online*, Master thesis, Facoltà di Scienze e Tecnologie, Università degli Studi di Milano, 2018.

[23] Carlotta Versmold, "Bohmian Trajectories in a Double Slit Experiment", *Published online*, Master thesis, Faculty of Physics, Ludwig-Maximilians-Universität Mün-chen, 2021.

[24] Lev Vaidman, "Many-Worlds Interpretation of Quantum Mechanics", *The Stanford Encyclopedia of Philosophy*, Edward N. Zalta, Ed., Metaphysics Research Lab, Stanford University, 2021, *Online; acessed 17th April 2023*.

[25] Todd A. Brun, "A simple model of quantum trajectories", *American Journal of Physics*, vol. 70, no. 7, pp. 719–737, 2002.

[26] Yakir Aharonov, Peter G Bergmann, and Joel L Lebowitz, "Time symmetry in the quantum process of measurement", *Physical Review*, vol. 134, no. 6B, B1410, 1964.

[27] Jan Dziewior, "The Concept of Weak Values", *Published online*, Master thesis, Faculty of Physics, Ludwig-Maximilians-Universität München, 2016.

[28] Yakir Aharonov and Lev Vaidman, "Properties of a quantum system during the time interval between two measurements", *Physical Review A*, vol. 41, no. 1, p. 11, 1990.

[29] Justin Dressel, Mehul Malik, Filippo M. Miatto, Andrew N. Jordan, and Robert W. Boyd, "Colloquium: Understanding quantum weak values: Basics and applications", *Reviews of Modern Physics*, vol. 86, no. 1, p. 307, 2014.

[30] T. Biswas, M. García Díaz, and A. Winter, "Interferometric visibility and coherence", *Proceedings of the Royal Society A: Mathematical, Physical and Engineering Sciences*, vol. 473, no. 2203, p. 20 170 170, 2017.

[31] Lev Vaidman, "Past of a quantum particle", *Physical Review A*, vol. 87, no. 5, p. 052 104, 2013.

[32] Lev Vaidman, "Tracing the past of a quantum particle", *Phys. Rev. A*, vol. 89, no. 2, p. 024 102, 2014.

[33] Lev Vaidman and Izumi Tsutsui, "When photons are lying about where they have been", *Entropy*, vol. 20, no. 7, p. 538, 2018.

[34] Ariel Danan, Demitry Farfurnik, Shimshon Bar-Ad, and Lev Vaidman, "Asking photons where they have been", *Physical review letters*, vol. 111, no. 24, p. 240 402, 2013.

[35] Zheng-Hong Li, M. Al-Amri, and M. Suhail Zubairy, "Comment on "Past of a quantum particle"", *Phys. Rev. A*, vol. 88, no. 4, p. 046 102, 2013.

[36] Hatim Salih, "Commentary: "Asking photons where they have been" - without telling them what to say", *Frontiers in Physics*, vol. 3, p. 47, 2015.

[37] Berthold-Georg Englert, Kelvin Horia, Jibo Dai, Yink Loong Len, and Hui Khoon Ng, "Past of a quantum particle revisited", *Phys. Rev. A*, vol. 96, no. 02, p. 022 126, 2017.

[38] Uri Peleg and Lev Vaidman, "Comment on "Past of a quantum particle revisited"", *Physical Review A*, vol. 99, no. 2, p. 026 103, 2019.

[39] Jerzy Dajka, "Faint trace of a particle in a noisy Vaidman three-path interferometer", *Scientific Reports*, vol. 11, no. 1, p. 1123, 2021.

[40] Rajendra Bhati and Arvind Singh, "Do weak values capture the complete truth about the past of a quantum particle?", *Physics Letters A*, vol. 429, p. 127 955, 2022.

[41] Gregory Reznik *et al.*, "Photons are lying about where they have been, again", *Physics Letters A*, vol. 470, p. 128 782, 2023 ISSN: 0375-9601.

[42] Miguel A. Alonso and Andrew N. Jordan, "Can a Dove prism change the past of a single photon?", *Quantum Studies: Mathematics and Foundations*, vol. 2, no. 3, pp. 255–261, 2015.

[43] Elina Köster, "Analysis of an Interferometric Measurement of Spatial Displacements and Deflections of a Light Beam", Bachelor thesis, Faculty of Physics, Ludwig-Maximilians-Universität München, 2020.

[44] Andrew N. Jordan, Julián Martínez-Rincón, and John C. Howell, "Technical Advantages for Weak-Value Amplification: When Less Is More", *Physical Review X*, vol. 4, no. 1, p. 011 031, 2014.

[45] David J. Starling, P. Ben Dixon, Andrew N. Jordan, and John C. Howell, "Optimizing the signal-to-noise ratio of a beam-deflection measurement with interferometric weak values", *Physical Review A*, vol. 80, no. 4, p. 041 803, 2009.

[46] Lijian Zhang, Animesh Datta, and Ian A. Walmsley, "Precision Metrology Using Weak Measurements", *Physical Review Letters*, vol. 114, no. 21, p. 210 801, 2015.

[47] Christopher Ferrie and Joshua Combes, "Weak value amplification is suboptimal for estimation and detection", *Physical review letters*, vol. 112, no. 4, p. 040 406, 2014.

[48] Gerardo I. Viza, Julián Martínez-Rincón, Gabriel B. Alves, Andrew N. Jordan, and John C. Howell, "Experimentally quantifying the advantages of weak-value-based metrology", *Physical Review A*, vol. 92, no. 3, p. 032 127, 2015.

[49] George C. Knee and Erik M. Gauger, "When amplification with weak values fails to suppress technical noise", *Physical Review X*, vol. 4, no. 1, p. 011 032, 2014.

[50] Juan P Torres and Luis José Salazar-Serrano, "Weak value amplification: a view from quantum estimation theory that highlights what it is and what isn't", *Scientific reports*, vol. 6, no. 1, pp. 1–11, 2016.

[51] Omar S. Magaña-Loaiza, Jérémie Harris, Jeff S. Lundeen, and Robert W. Boyd, "Weak-value measurements can outperform conventional measurements", *Physica Scripta*, vol. 92, no. 2, p. 023 001, 2016.

[52] Stephen M. Barnett, Claude Fabre, and Agnes Maıtre, "Ultimate quantum limits for resolution of beam displacements", *The European Physical Journal D-Atomic, Molecular, Optical and Plasma Physics*, vol. 22, pp. 513–519, 2003.

[53] Marek Dobosz, "Interference sensor for ultra-precision measurement of laser beam angular deflection", *Review of Scientific Instruments*, vol. 89, no. 11, p. 115 003, 2018.

[54] R. Clark Jones, "A New Calculus for the Treatment of Optical Systems I. Description and Discussion of the Calculus", *J. Opt. Soc. Am.*, vol. 31, no. 7, pp. 488–493, Jul. 1941.

[55] E. J. Post, "Sagnac Effect", *Rev. Mod. Phys.*, vol. 39, no. 2, p. 475, 1967.

[56] Max Laue, "Über einen Versuch zur Optik der bewegten Körper", *Münchener Sitzungsberichte*, vol. 12, pp. 405–412, 1911.

[57] Tristan Zerweck, "Measuring Beam Deflections via Weak Amplification in a Sagnac Interferometer", Bachelor thesis, Faculty of Physics, Ludwig-Maximi-lians-Universität München, 2022.

[58] Thorlabs, *Position Sensing Detectors*, `https://www.thorlabs.com/NewGroupPage9.cfm?ObjectGroup_ID=4400`, *Online; accessed 23th March 2023*.

[59] Anssi Mäkynen, "Position-sensitive devices and sensor systems for optical tracking and displacement sensing applications", *Published online*, Ph.D. dissertation, Oulun yliopisto, Teknillinen tiedekunta, Sähkötekniikan osasto, 2000.

[60] Picotech, *Differential and floating voltage measurements*, `https://www.picotech.com/library/oscilloscopes/differential-and-floating-voltage-measurements`, *Online; accessed 15th March 2023*.

[61] I. August, Y. Oiknine, M. AbuLeil, Ibrahim Abdulhalim, and Adrian Stern, "Miniature Compressive Ultra-spectral Imaging System Utilizing a Single Liquid Crystal Phase Retarder", *Sci Rep*, vol. 6, no. 23524, pp. 1–9, 2016.

[62] Juan M. Bueno, "Polarimetry using liquid-crystal variable retarders: theory and calibration", *Journal of Optics A: Pure and Applied Optics*, vol. 2, no. 3, p. 216, May 2000.

Acknowledgments

Viele Leute haben direkt oder indirekt einen Anteil an der Entstehung dieser Arbeit. Ihnen allen möchte ich meinen größten Dank aussprechen. Besonders danken möchte ich den folgenden Personen:

- Professor Harald Weinfurter für die Möglichkeit in seiner Arbeitsgruppe meine Masterarbeit zu verfassen. Ich bin sehr froh und dankbar, ein solch spannendes Thema als Masterarbeit gehabt zu haben.
- Carlotta Versmold für die wunderbare Betreuung. Vielen Dank für die vielen stets enorm hilfreichen und geduldigen Erklärungen, für die Unterstützung und Motivation, aber auch für die produktiven und lustigen Stunden im Labor.
- Jan Dziewior für die immerzu aufschlussreichen Erklärungen und die freundliche Unterstützung.
- Florian Huber, Dr. Jasmin Meinecke, Vinay Tumuluru, Dr. Sholeh Razavian, Akaash Srikanth sowie allen weiteren Mitgliedern der xqp-Gruppe. Danke für die warme Aufnahme in die Gruppe und für das entspannte Arbeitsumfeld. Danke für die vielen lustigen und lehrreichen Stunden und interessanten Gespräche über Physik und andere Themen.
- Tristan Zerweck für den produktiven Start am Experiment.
- Professor Lev Vaidman for fruitful and humorous discussions on various topics related to this thesis.
- Emma Brink für die motivierenden Stunden gemeinsam beim Masterarbeit schreiben in der Bib. Julia Kostin für den interessierten Besuch im Labor und die nette Zeit zusammen in Garching. Sophie Atzpodien für das große Interesse an und den vielen interessierten Fragen zu Weak Values.
- Jonas Zimmermann für die große Unterstützung und die sinnvollen Tipps, sowie dafür, stets ein offenes Ohr für mich gehabt zu haben.
- Allen weiteren Freund:innen und netten Leuten, die mich im Studium begleitet haben und die letzten fünfeinhalb Jahre zu einer unvergesslichen Zeit gemacht haben.

– Meine Eltern Gerta Köster und Tilman Dürbeck, die mich bei meinen Tätigkeiten bedingungslos unterstützen. Die meine Neugierde auf die Welt schon immer förderten und somit einen Einfluss darauf hatten, dass ich nun meine Arbeit in diesem Feld abgebe. Ich möchte auch meiner Schwester Felizia sowie meiner Oma für die Unterstützung und Motivation danken.

Eigenständigkeitserklärung

Hiermit erkläre ich, Elina Köster, die vorliegende Arbeit selbständig verfasst zu haben und keine anderen als die in der Arbeit angegebenen Quellen und Hilfsmittel benutzt zu haben.

München, 02.05.2023 Elina Köster